Numerical Analysis of Local and Global Hydroelastic Response of Wetdeck Slamming Events on Multihull Vessels
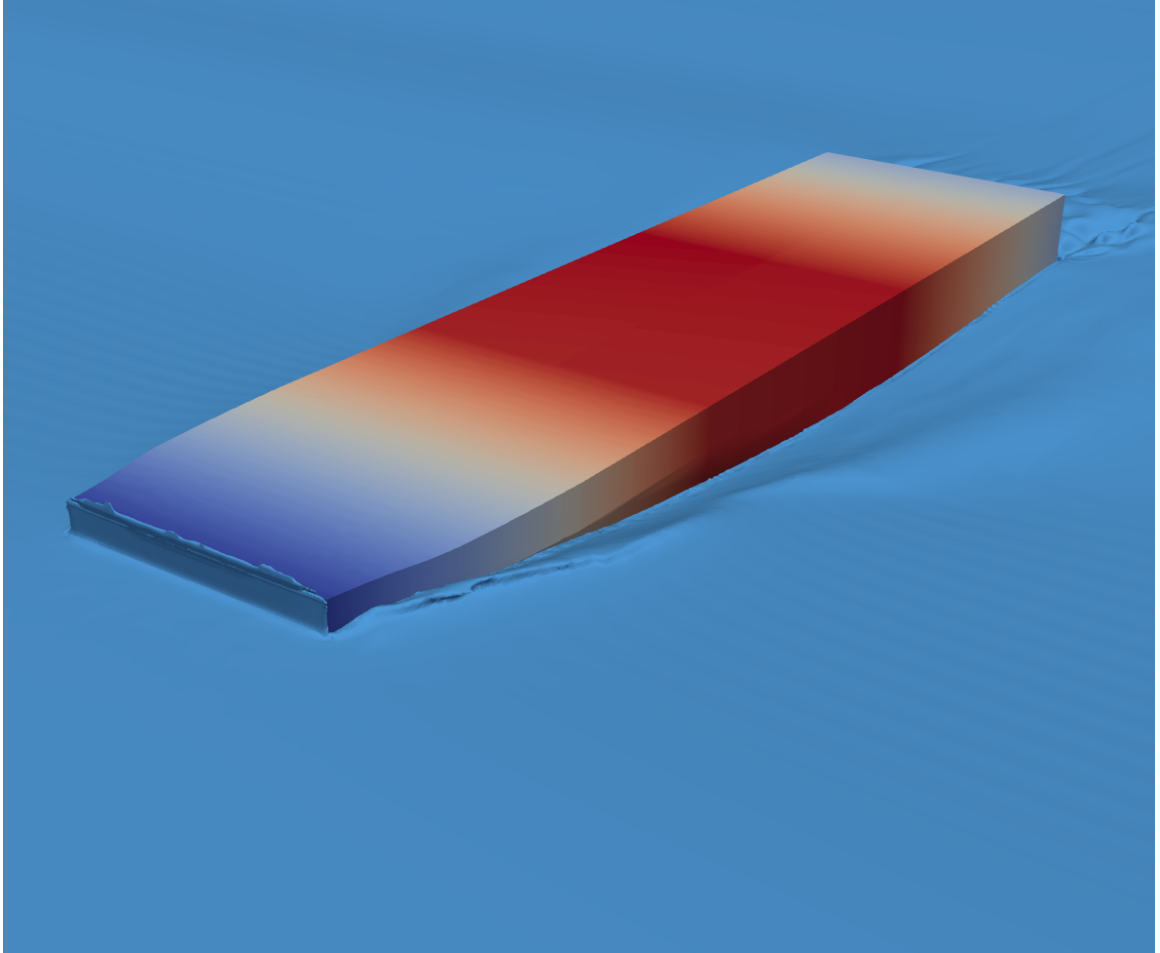
by

Matthew T. Graham

A dissertation submitted in partial fulfillment
of the requirements for the degree of
Doctor of Philosophy
(Naval Architecture and Marine Engineering and Scientific Computing)
in The University of Michigan
2018

Doctoral Committee:

   Associate Professor Kevin J. Maki, Chair
   Associate Professor Matthew D. Collette
   Associate Professor Eric Johnsen
   Professor Yin Lu (Julie) Young

Matthew T. Graham
grahmatt@umich.edu
ORCID id: 0000-0002-1324-5002

ACKNOWLEDGEMENTS

TABLE OF CONTENTS

LIST OF FIGURES

LIST OF TABLES

LIST OF ABBREVIATIONS

ALE Arbitrary Lagrange-Eulerian

BEM Boundary Element Method

CFD Computational Fluid Dynamics

FEA Finite Element Analysis

FEM Finite Element Model

FSI Fluid-Structure Interactions

HBVP Hydrodynamic Boundary Value Problem

HSLA High-Strength Low-Alloy

JHSS Joint High Speed Sealift

MRU Motion Reference Unit

RAO Response Amplitude Operators

RQS Rigid-Quasi Static

SES Surface Effect Ship

SPH Smoothed Particle Hydrodynamics

VoF Volume of Fluid

ABSTRACT

Catamarans operating in a large sea state encounter slamming events on the wet-deck that may lead to structural failure. Wetdeck slamming is a non-linear process which involves complex free-surface topology, high-velocity water jets, and breaking waves interacting with the bow and deck-hull geometry. The slamming process generates large pressures and loads that are time dependent and concentrated in space. The structure responds in a coupled manner to the complex fluid loading. Common approaches to design for the limiting slamming loads include analytical models or segmented model tests. Analytical slamming models assume a linear free-surface, prescribed velocities, and simplified geometries. These simplified assumptions make it difficult to apply to realistic cases. Experimental model tests capture slamming loads by using segmented models attached to a backspline. It is difficult to scale results to full-scale and to recreate model scale conditions that lead to the limiting load cases.

A high-fidelity fluid-structure interaction solver is used to study a simplified impact problem and slamming on a catamaran. The canonical problem is a flat plate impacting a curved water surface. A detailed analysis is conducted on the simple flat plate showing the influence of boundary conditions, structural non-linearities, and the relative impact velocities. A new adaptive inertial under-relaxation scheme is developed for solving the artificial added mass instabilities due to the segregated coupling of the CFD and FEA models. Catamaran slamming simulations compare the influence of global loads on the local wetdeck structure. The full field data provided by the numerical solver is used visualization of flat wetdeck slamming loads. Careful

evaluation of existing impact models are presented and recommendations for reduced order modeling of maximum stress during wetdeck slamming are provided.

CHAPTER I

Introduction

Oceangoing vessels in heavy seas experience slamming events due to large relative vertical motions of the vessel and sea surface. Slamming events can cause a whipping response in the structure in addition to the springing response caused by the encounter wave frequency being close to, or a multiple of, the the hull natural frequency. Slamming events most often occur near the bow region in head seas and sometimes occur at the stern. Recent economic design trends in shipping have led to larger vessels. These larger vessels are subject to hydroealstic effects from springing and whipping and have experienced structural failure such as the case of the MOL COMFORT (2015) and MSC Napoli (2008). In the case of the MOL COMFORT, Figure 1.1, the vessel completely broke in half before sinking. Even though these vessels met the current classification societies rules, it is clear that dynamic effects from springing and whipping can not be ignored when designing the structure of a ship. The research area of dynamic springing and whipping loads on container ships has grown in recent years for the purpose of providing recommendations for classification society rules and building safer ships.

For catamarans, slamming events lead to large structural loads on the wetdeck area located between the two hulls. These slamming loads are experienced in large and small vessels. Slamming events can produce the maximum structural loads that a

Figure 1.1: MOL COMFORT after structural failure and before sinking

vessel will see during its service life. If the maximum loads are not properly designed for, plastic deformation or failure to the structure can occur as seen in Figure 1.2, for the INCAT 96 m wave piercing catamaran. External plate buckling is seen on the forward side hull after the catamaran experienced an extreme slam event Lavroff et al. (2013). Slamming on the wetdeck is a complex process and difficult to model due to the wave breaking, hull interactions, air entrapment, and ship motions that effect the response of the structure. In addition to the local slamming loads, the global whipping and springing response may contribute to the structural failure.

One advantage of catamarans is their ability to offer a large flat deck area. The outer portion of the lower deck structure that connects the two hulls is called the wetdeck. Figures 1.3 and 1.4 shows two common wetdeck designs circled in red. In some cases the wetdeck may be flat as seen in Figure 1.3, which makes the wetdeck vulnerable to large slamming loads in large sea states. Figure 1.4 shows a popular design for catamarans involving the use of wave-piercing bows to reduce the added resistance due to a sea state. Although the wave-piercing bows provide a reduction

Figure 1.2: External plate buckling after an extreme slam event Lavroff et al. (2013)

in resistance, the reduced buoyancy in the front of the bows makes the vessel more susceptible to wetdeck slamming. For this reason, a wedge-shaped wetdeck was designed to reduce the impulse force on the wetdeck structure. This wedge shape adds weight and air resistance to the catamaran, which is a compromise in the design for the reduction of slamming motions.

Slamming forces on a wetdeck may cause large structural loads and whipping, which can contribute to global structural fatigue. Accurately predicting the slamming forces on a wetdeck structure is important for design evaluation. There are many challenges to the designer to accurately model wetdeck and global structure loading. Structural models typically use a Finite Element Model (FEM) that can be as simple as a single beam or incorporate the full details of the ship structure using a large number of structural elements stiffeners, frames, and plates. Corrosion and fatigue of the structure can also lead to failures in the harsh marine environment. Fluid models

Figure 1.3: X-craft naval catamaran showing the design of a flat wetdeck circled in red

Figure 1.4: The naval HSV-2 Swift catamaran with wave piercing bows and a wedge shaped wetdeck to mitigate slamming loads

can incorporate analytical models or higher fidelity tools such as Computational Fluid Dynamics (CFD). Fluid models need to account for the random ocean environment which includes wind, waves, currents, and potential for green water on deck that all contribute to a vessels motions and structural response. Higher fidelity tools are computationally expensive and do not capture all of the complex interactions that lead to the structural response of the vessel. In addition, analytical and numerical tools have not been fully validated and experimental results are difficult to scale and measure accurately. Using the higher fidelity tools on extreme slam events can provide insights to reduced order models. The higher fidelity tools model more of the physics involved in the Fluid-Structure Interactions (FSI) and allow for corrections or insights to be gained when using a reduced order model.

Current analytical methods are limited in modeling the nonlinear interactions that occur during a wetdeck slamming event. It is difficult to define the appropriate boundary conditions, the relative velocity of impact, the effective deadrise angle, and the three-dimensional ship geometry in terms of two-dimensional contours. The objective of this research is to provide a new in-depth analysis of wetdeck slamming loads to assist analytical modeling methods. This research uses a tightly coupled CFD and Finite Element Analysis (FEA) numerical FSI solver to study the complex interactions between the fluid and the structure during a wetdeck slam event. The FSI solver captures the three-dimensional free-surface that is typically omitted in analytical slam models. The full field data is available for the fluid and the structure allowing for a complete spatial representation of a wetdeck slam event.

Chapter II provides an overview of slamming analysis techniques and a detailed description of the FSI solver. Chapter III provides a detailed slamming analysis of a canonical problem. The canonical problem is a simple two-dimensional flat plate impacting a free-surface and is used as a validation case for reduced order slamming models. The simplified flat plate problem allows for a detailed review of the FSI

solver stability, accuracy, and convergence. Chapter IV presents a new adaptive inertial under-relaxation scheme used to stabilize the segregated FSI solver. In this chapter the new algorithm is applied to the flat-plate drop canonical problem, and a detailed analysis shows how the fluid added mass varies and influences the stability of the algorithm. Chapter V analyzes the flow and structural response of a catamaran operating with forward speed in wave a condition that leads to wetdeck slamming. The FSI solver provides novel details of the progression of a flat wetdeck slam event and the influence between the global and local structure response. Comparisons of the wetdeck slamming loads to the two-dimensional simple plate problem are provided, and recommendations are provided for reduced order modeling of wetdeck slamming loads. Finally, Chapter VI summarizes the research work, lists the contributions, and suggests recommendations for future research.

CHAPTER II

Background

The three main analysis techniques used for fluid-structure interactions during slamming events are analytical solutions, experimental model tests, and numerical analysis. Each technique has its advantages and disadvantages depending on the type of slamming problem being modeled. This research focuses on expanding a new numerical technique that couples a CFD Volume of Fluid (VoF) approach for the fluid domain to an FEA model of the structure that uses a modal decomposition. This new numerical technique is a high-fidelity FSI solver that can be used to model wetdeck slamming on catamarans with realistic geometries. This high-fidelity tool models the complex three-dimensional geometry and the non-linear interactions of the free-surface with the geometry.

2.1 Analytical Models

The modern analytical methods for predicting slamming forces were first developed by Von Karman (1929) for the maximum pressure forces on seaplane floats during landing. A two-dimensional wedge was used to model the bottom of the seaplane float. Wagner (1932) extended upon this method by accounting for the pile-up of displaced water using momentum theory and a potential flow approach. Both methods attempt to solve for the pressure on an impacting body by accounting for

the added mass effects. The methods are two-dimensional and the velocity of the impact is prescribed. Bishop and Price (1979) developed a method to study the hydroelasticity of ship structures by modeling a ship as a beam and solving for the modal decomposition of the structure. Hydrodynamic forces are applied to the structure using strip theory. Bishop et al. (1986) extended upon the hydroelastic analysis to incorporate catamaran structures for the analysis of sectional forces and bending moments.

The analytical slamming models were first used to model wetdeck slamming loads by Zhao and Faltinsen (1992). Kvalsvold and Faltinsen (1995) derived a numerical solution for hydroelastic response of wetdeck slamming that uses analytical functions for modeling the hydrodynamic loads on a flat plate impacting the top of a wave. Two-dimensional Timoshenko beam elements where used for a modal decomposition of the structure. A Hydrodynamic Boundary Value Problem (HBVP) was solved using Wagner's Theory (Wagner, 1932), which includes the pile-up of water to estimate the wetted length of the plate. The coordinate system of the HBVP is shown in Figure 2.1. Three stages of entry were identified when modeling the hydroelastic response, the compressible phase, the structural inertia phase, and the added mass restoring phase. Compressible effects due to air entrapment did not have a significant effect on the maximum stress up to and including the structural inertia phase. However, a simplified one-dimensional acoustic approximation is used to model the compressible phase.

Faltinsen et al. (1997) developed an asymptotic solution procedure based of the results from Kvalsvold and Faltinsen (1995) to solve the flat plate impact problem. The compressible phase is neglected and only the structural inertia and added mass restoring phases are considered. The plate is assumed fully wetted and the velocity is constant. This simplifies the solution procedure since the phase with time dependence of the wetted length of the plate is not calculated. Both Økland (2002) and Ge (2002)
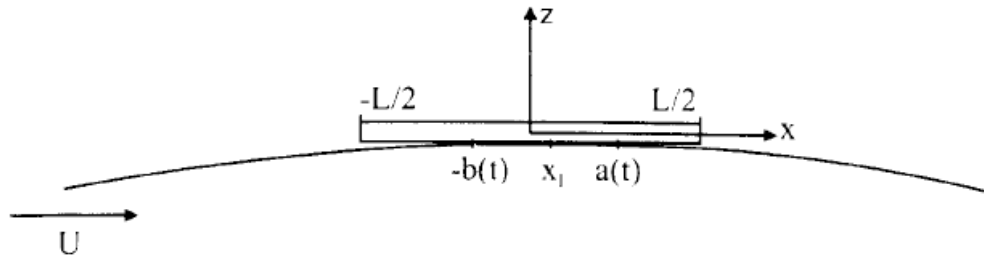
Figure 2.1: Coordinate system for the HBVP for a flat plate impacting the top of a wave (Kvalsvold and Faltinsen, 1995).

studied the global loads on catamarans with flat wetdecks in a sea state. Slamming forces are modeled using the two-dimensional analytical theories. Ge et al. (2005) used a similar method to Kvalsvold and Faltinsen (1995), but used the Von Karman (1929) assumption to model wetdeck slamming. Ge et al. (2005) found that further improvements need to be made to properly capture the three-dimensional interactions when modeling wetdeck slamming on catamarans analytically.

Wedge impacts have been widely studied since Von Karman (1929) first used them. More recently, hydroelastic analysis of wedge impacts have been developed to model the fluid-structure interactions. Korobkin et al. (2006) used a generalized Wagner approach similar to Kvalsvold and Faltinsen (1995), but coupled to a FEM to study the impact of an elastic wedge. The FEM consisted of Euler beam elements and a modal decomposition was calculated using FEA techniques. Using a FEM allows for more realistic structures to be modeled and the generalized Wagner approach will give good results for blunt body impacts. The generalized Wagner approach is only valid while the chines are dry. Once the wedge or blunt body is fully wetted the Wagner model is no longer valid since it accounts for the force of the changing wetted length. Piro and Maki (2011) studied the entry and exit of a two-dimensional wedge by coupling CFD and FEA model. Results showed that in some cases the exit phase of an elastic wedge can generate larger structural forces than the entry phase. This suggests that further development of analytical models may be needed to model the

9

maximum slamming loads on a structure that experiences entry and exit phases.

The analytical models described in this section work well during the entry stage of impacting blunt bodies. The velocity of the impacting body must be known ahead of time. If the velocity of impact is not constant, then the analytical models become difficult to solve and numerical techniques must be employed. The widely used Wagner model is only valid up to the body becoming fully wetted. Analytical models are not valid for the exit stage of a slamming body as they can not properly model the time dependence wetted length of the body. Numerical solvers, such as the one used in this research, are able to provide insights into further development of analytical models for entry and exit stages.

2.2 Experimental Models

There are two different ways to model hydroelastic slamming effects experimentally. The first involves a fully elastic model. This can be measuring slamming forces on a full scale prototype or a smaller section of a full scale model such as flat plate drop tests. The second is a segmented model test. This is where a scaled model of a vessel is cut into segments and attached to a backspline that is scaled to the appropriate structural elastic properties of the full scale vessel. An example of a segmented model is shown in Figure 2.2 with three cuts along each hull corresponding to $L/4$, $L/2$, and $3L/4$ where L is the length of the model. The cuts are the white vertical strips in Figure 2.2, which are sealed to prevent water from penetrating the model while still allowing the model to deflect under load.

Full scale prototype models are not practical for large vessels. Full scale vessel testing has many complications including relying on the environment to produce slamming conditions. Faltinsen (2001) conducted full scale testing with a high speed catamaran. Strain measurements were taken in several areas along the hull and wetdeck. However, measurements for vertical velocities, free surface elevation, and
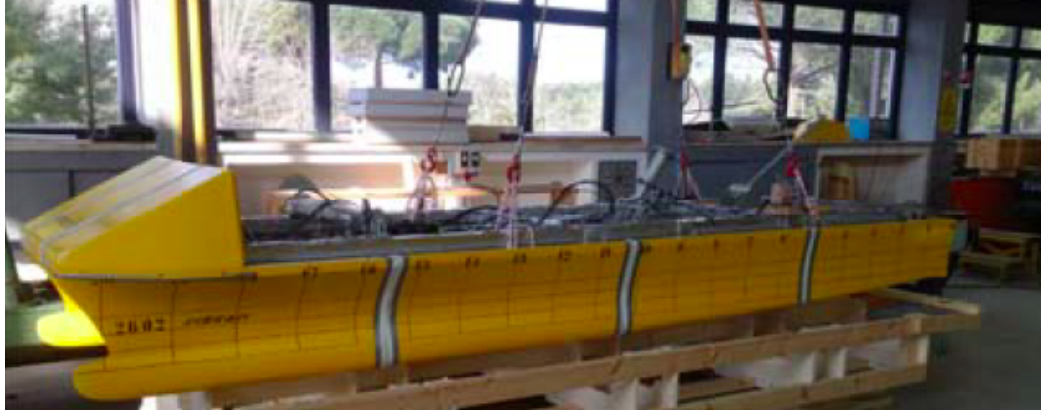
Figure 2.2: Example of a segmented X-Craft scaled model from Dessi et al. (2016).

pressures were not taken, which hampered comparisons to analytical results. Jacobi et al. (2014) took full scale measurements of the strains on the structure of the 98 m long HSV-2 catamaran to investigate slamming loads. Reducing the operating speed or changing heading from head seas greatly reduced the number of slams and maximum loading on the structure due to slam events.

Greenhow and Lin (1983) first studied rigid wedge and cylinders impacting the free-surface and made comparisons to two-dimensional free-surface theories. The exit phase of a fully submerged cylinder was also studied, but the two-dimensional theories were insufficient at describing the complex vortex shedding and free-surface interactions during the exit phase. Whelan (2004) conducted experimental drop tests on two-dimensional bow sections for wedge shaped wetdecks. Recommendations for wedge section shapes to reduce maximum accelerations are provided and compared with added mass theories. Swidan et al. (2017) conducted vertical drop tests on the INCAT model bow section with different geometries. Visual inspection of the impacting flow and forcing on the bow section are analyzed.

Fully elastic scaled models are extremely difficult to test and not all scaling parameters can be met simultaneously. Flat plate drop tests are a useful way to model local structural impacts. Faltinsen et al. (1997) conducted flat plate impacts on top of wave crests. The flat plate drops were only conducted for relatively large radius of

wave curvature, and difficulties in dropping the wedge on the top of the wave crest were documented.

The number of segments used can effect the response of the backspline structure. Økland et al. (2003) found that at least three segments per hull were needed to model the global structure mode shapes for catamarans with four segments yielding better accuracy of typical structure mode shapes. When cavitation, ventilation, or air entrapment occurs during wetdeck slamming, Thomas et al. (2011) found that the segmented catamaran model had conservative predictions for structural loads when compared to the full scale vessel measurements. Lavroff et al. (2013) used a segmented model of the INCAT catamaran with forward speed to capture global hydroelastic response due to slamming. Maximum loads on the structure occurred during slam impacts.

Experimental testing for hydroelastic effects is complex and difficult. Scaling of the velocities and structural properties provides significant challenges for full scale extrapolations. Well documented test setups and data are needed for both the structure and model geometry to compare with analytical and numerical simulations. Although experimental model tests are challenging and may have scaling issues, they also provide valuable data that can be used for validation of analytical and numerical models.

2.3 Numerical Models

There are several numerical techniques that are used to model slamming events. Some of these numerical techniques incorporate the two-dimensional analytical models to estimate forces during slamming. The more complicated analytical models, such as Kvalsvold and Faltinsen (1995), require numerical techniques to solve for the time dependent wetted length. This section will focus on the more advance numerical techniques that try to model the full three-dimensional geometry of a vessel and complex fluid-structure interactions. These include numerical techniques such as

Boundary Element Method (BEM), Smoothed Particle Hydrodynamics (SPH), and CFD.

Zhao and Faltinsen (1992) developed the BEM for the slamming of two dimensional bodies. Although good agreement was found for two dimensional wedge sections, three dimensional effects were not captured. Three-dimensional effects can be very important for wetdeck slamming on catamarans in real sea conditions. Three dimensional Rankine panel methods have been developed to handle ship motions in a seaway. A code capable of handling non-linear Wave-Induced loads and SHip motion (WISH) was developed with capabilities of modeling the a ship structure as a beam (Kim et al., 2011). Kim et al. (2015) used a three dimensional Rankine panel method with a Generalized Wagner Model (GWM) for slamming using two-dimensional sections. Results were compared with a segmented container ship model showing good agreement for whipping response due to slamming.

An Euler-Lagrange coupling method to capture the fluid-structure interaction for a wedge drop impacting water was studied by Aquelet et al. (2006), Stenius et al. (2007), Das and Batra (2011), and Wang and Guedes Soares (2017). The fluid solves the Navier-Stokes equations using an Arbitrary Lagrange-Eulerian (ALE) formulation on a fixed or moving mesh, while the structure is solved using a Lagrange formulation on a deforming mesh. A contact penalty approach is used to couple the fluid and structure solutions. The contact penalty approach causes oscillations in the fluid pressure acting on the wedge. Aquelet et al. (2006) proposed a damping term to remove the non-physical oscillations from the pressure. Stenius et al. (2011) used a multi-material ALE formulation to model air and water for an elastic wedge impact. The importance of fluid structure interactions was found by comparing to Rigid-Quasi Static (RQS) results. De Rosis et al. (2014) modeled a hydroelastic wedge impact using the lattice Boltzmann method coupled to a FEM. The numerical results underpredicted strain at different impact velocities, but followed the trends

of the experimental results. SPH is used by Amicarelli et al. (2015) and Gong et al. (2016) to model rigid wedge impacts and Lind et al. (2015) used SPH to model rigid flat plate impacts. Detailed hydroelastic results using SPH have not been widely used and validated. Most SPH studies have used rigid structures to compare forcing to experiments.

Common techniques in industry to model fluid structure interactions use CFD with a one-way coupling to the FEM structure to perform a RQS analysis. Maki et al. (2011) improved upon the RQS analysis and provide the structure inertia effects by performing a one-way coupling between the fluid and structure for a wedge drop with a 10 degree deadrise angle. Wet natural frequencies were modeled with acoustic elements on the FEM structure. The difference in maximum displacement of the wet and dry natural frequencies showed the importance of capturing the correct wetted length of the wedge during impact. Piro and Maki (2011) studied the FSI of a wedge during entry and exit using CFD VoF approach coupled to a modal decomposition of a FEM structure using beam elements. This two-way coupled technique allows for the time varying added mass and wetted length of the wedge to be modeled. The study also compared an exact boundary condition with a deforming mesh to an approximate boundary condition with no deformations and only structure velocities that are given to the fluid patch. For small deflections, the approximate boundary condition had good comparisons with the exact boundary condition. Camilleri et al. (2015) also looked at wedge drops by coupling two commercial codes, CFD with Star CCM+ and FEM with Abaqus. A large computational expense was needed to converge the fluid and structure solutions using this two-way coupled method. The full structure model was used adding to the computational expense of the method.

Two-way coupling of CFD and FEM has been used to model FSI interactions due to ship slamming in head seas. El Moctar et al. (2011) coupled VoF CFD with Timoshenko beam elements to model bow flare slamming for containerships. This

technique was extended by Seng (2012), Seng et al. (2014), Oberhagemann (2016), and el Moctar et al. (2017) to compare with experimental results for a segmented containership model. Good agreement was observed with experimental results when comparing the vertical bending moment in a sea state with slamming. Piro (2013) used a similar technique to study slamming with green water on the deck of a segmented Joint High Speed Sealift (JHSS) model. A modal decomposition was used for the FEM to reduce the degrees of freedom and an approximate boundary condition to remove the need to morph the fluid mesh. This allowed the FSI solver to run at similar computational expense as the rigid body simulations. Higher frequencies in the structural responses were not fully captured, but the lower frequencies that correspond to the primary bending modes showed good agreement with experiments. Southall et al. (2016) studied vertical bending moments on a segmented containership model by using a linear seakeeping code to predict vessel motions and detect slamming events. Slamming forces are accounted for using two-dimensional CFD runs for sections experiencing a slam with the initial conditions and motions provided from the linear code. This method reduces the computational expense allowing for longer simulations to be conducted for statistical analysis. McVicar et al. (2018) coupled the commercial CFD solver Star-CCM+ with the commercial FEA solver Abaqus to study slamming on a wave piercing catamaran model. One-way and two-way coupling techniques were compared. The two-way coupling was found to be computationally expensive so the one-way coupling technique was recommended that includes an added-mass estimation. Comparisons of the global loads from the segmented model experiments showed decent agreement.

Two-way coupled CFD and FEM provide a way to model realistic three dimensional geometries and capture non-linear hydrodynamic effects; however, there is a significant computational expense and should only be used when three dimensional and non-linear hydrodynamic effects are important. This research uses Piro (2013)

formulation to study global and local slam events on flat wetdeck structures. One-way and two-way coupling techniques will be compared. The two-way coupling method captures the added mass effects and has a similar computationally expense as the one-way method depending on the number of iterations needed to converge the solution.

2.4   FSI Solver

The development of the FSI solver is described in detailed by Piro (2013). This section gives a short overview of the FSI solver and how the coupling between the fluid and the structure is handled.

The FSI solver uses CFD with a VoF surface capturing techniques for the fluid domain, coupled with a FEA modal decomposition for the structure domain. The solver is validated with elastic wedge drops and segmented model tests of the JHSS in head seas. The fluid solution is solved using the OpenFOAM 2.4.x CFD library. OpenFOAM uses an arbitrary-polyhedral discritization that allows for the modeling of realistic and complex geometries. The governing fluid equations are the Navier-Stokes equations,

$$\nabla \cdot \vec{u} = 0 \tag{2.1}$$

$$\frac{\partial \rho \vec{u}}{\partial t} + \nabla \cdot \rho \vec{u} \vec{u} = -\nabla p + \nabla \cdot \left[\mu \left(\nabla \vec{u} + \nabla \vec{u}^T \right) \right] + \rho \vec{g}. \tag{2.2}$$

An arbitrary Lagrangian-Eulerian finite volume discritization is used to allow for a moving and deforming mesh. A two-phase flow is captured using the VoF technique with the equation governing the phase-indicator variable α,

$$\frac{\partial \alpha}{\partial t} + \nabla \cdot (\alpha \vec{u}) + \nabla \cdot (\alpha(1 - \alpha)\vec{u_r}) = 0. \tag{2.3}$$

16

The volume fraction variable, α, tracks the two phases which are 0 for air and 1 for water. This method allows for the tracking of a nonlinear free-surface. Fluid discritization schemes are second order space and first order in time.

The structure is modeled using the FEM. The homogeneous equations of motion for the FEM are written as,

$$[M]\{\ddot{u}\} + [K]\{u\} = 0 \tag{2.4}$$

where $[M]$ is the global mass matrix, $[K]$ is the global stiffness matrix, and $\{u\}$ is the displacement vector for the nodes. Assuming small deflections and sinusoidal vibrations, Equation 2.4 can be written as a determinate problem and the eigenvalues and eigenvectors of the system can be found. These correspond to the natural frequencies and mode shapes of the structure. The modal equations of motion including damping and forcing are,

$$[I]\{\ddot{q}_m\} + [2\zeta\omega_n]\{\dot{q}_m\} + [\omega_n^2]\{q_m\} = \{f_m\} \tag{2.5}$$

where $[I]$ is the identity matrix, $[2\zeta\omega_n]$ is the modal viscous damping matrix, $[\omega_n^2]$ is a diagonal matrix containing the squared natural frequencies of the structure, $\{q_m\}$ is a vector containing the modal amplitudes, and $\{f_m\}$ is the modal force vector. An advantage to using the modal equations of motion is the reduction of the number of degrees of freedom in the system. Small deflections are assumed for this linearization to be valid. The majority of the structure's energy is contained in the lower frequencies, which correspond to the first set of mode shapes, allowing for the high frequencies to be neglected.

The modal equations of motion are solved in time using the state-space representation,

$$\frac{d}{dt}\begin{Bmatrix}\{q_m\}\\ \{\dot{q}_m\}\end{Bmatrix} = \begin{bmatrix} 0 & 1 \\ -[\omega_n^2] & -[2\zeta\omega_n] \end{bmatrix}\begin{Bmatrix}\{q_m\}\\ \{\dot{q}_m\}\end{Bmatrix} + \begin{Bmatrix} 0 \\ \{f_m\}\end{Bmatrix} \qquad (2.6)$$

where the time derivative depends on the time stepping scheme. The state vector is saved for the two previous time steps to allow a second-order time stepping scheme to be used for the structure solution for the FSI solver. For a single degree-of-freedom the state-space representation can be written as,

$$X_{i+1}^{n+1} = [A]X^n + \begin{Bmatrix} 0 \\ \Delta t f_m \end{Bmatrix}_i^{n+1}, X = \begin{Bmatrix} q_m \\ \dot{q}_m \end{Bmatrix} \qquad (2.7)$$

where X is the state vector, the n index refers to the current time, and the i index refers to the current iteration.

The coupling of the two segregated codes using the FSI solver may have instabilities due to the artificial added mass as discussed by Young et al. (2012). The artificial added mass comes from the lag in exchanging data across the fluid-structure interface. An inertial under-relaxation scheme is used to stabilize the FSI solver. The modal equations of motion become,

$$([I] + [\Gamma])\{\ddot{q}_m\} + [2\zeta\omega_n]\{\dot{q}_m\} + [\omega_n^2]\{q_m\} = \{f_m\} + [\Gamma]\{\ddot{q}_{m,est}\} \qquad (2.8)$$

where $[\Gamma]$ is a diagonal matrix containing the inertial under-relaxation factors for each mode. Assuming a small time step size, the estimate of modal acceleration for each mode is a first-order finite difference scheme,

$$\ddot{q}_{m,est} \approx \frac{\dot{q}_m^{n+1} - \dot{q}_m^n}{\Delta t}. \qquad (2.9)$$

A single mode is analyzed for the stability of the FSI solver using the single degree-of-freedom modal equation of motion with inertial under-relaxation,

$$(1 + \Gamma)\ddot{q}_m + 2\zeta\omega_n\dot{q}_m + \omega_n^2 q_m = f_m + \Gamma\ddot{q}_{m,est}. \tag{2.10}$$

Equation 2.7 for a single degree-of-freedom and the iterative algorithm for updating the structure state becomes,

$$X_{i+1}^{n+1} = [A]X^n + \left\{ \begin{array}{c} 0 \\ \Delta t \frac{f_m + \Gamma\ddot{q}_{m,est}}{1+\Gamma} \end{array} \right\}_i^{n+1} \tag{2.11}$$

The modal force can be split into the modal added mass, γ_m and time dependent component $\tilde{f}$,

$$f_m = -\gamma_m\ddot{q}_m + \tilde{f}. \tag{2.12}$$

The final structure iteration algorithm is,

$$X_{i+1}^{n+1} = \begin{bmatrix} 0 & 0 \\ 0 & -\frac{\gamma_m - \Gamma}{1+\Gamma} \end{bmatrix} X_i^{n+1} + [A^*]X^n + \left\{ \begin{array}{c} 0 \\ \Delta t\tilde{f} \end{array} \right\}_i^{n+1}, \tag{2.13}$$

where $[A^*]$ is determined by the time discretization scheme with the addition of the velocity from the current time level for the estimation of acceleration. Knowing that the eigenvalues of the matrix must have a magnitude less than one, the inertial under-relaxation stability criteria is,

$$\Gamma \geq \frac{1}{2}(\gamma_m - 1). \tag{2.14}$$

Details on selecting the inertial under-relaxation and the impact on stability of the FSI solver is discussed in Chapter IV. A adaptive inertial under-relaxation scheme is presented in Chapter IV as well.

The solver tightly couples the fluid and structure solutions to capture the fluid structure interactions. The fluid solution is solved first and the pressure forces are

interpolated to the Gauss points, as shown in Figure 2.3. The fluid pressure interpolation to the structure is handled through a weighted distance function of the four closest fluid cell centers. The structural forces are then interpolated to nodes and transformed to modal forces using the eigenvectors. The modal equations of motion are then solved and transformed back to structural velocities and displacements at the nodes. The structural velocities and displacements are given to the fluid solution at the face centers using the structure shape functions. The fluid solution is solved again with the new structure displacements and velocities. This iterative process is repeated until the fluid and structural solution has converged for the current time step.
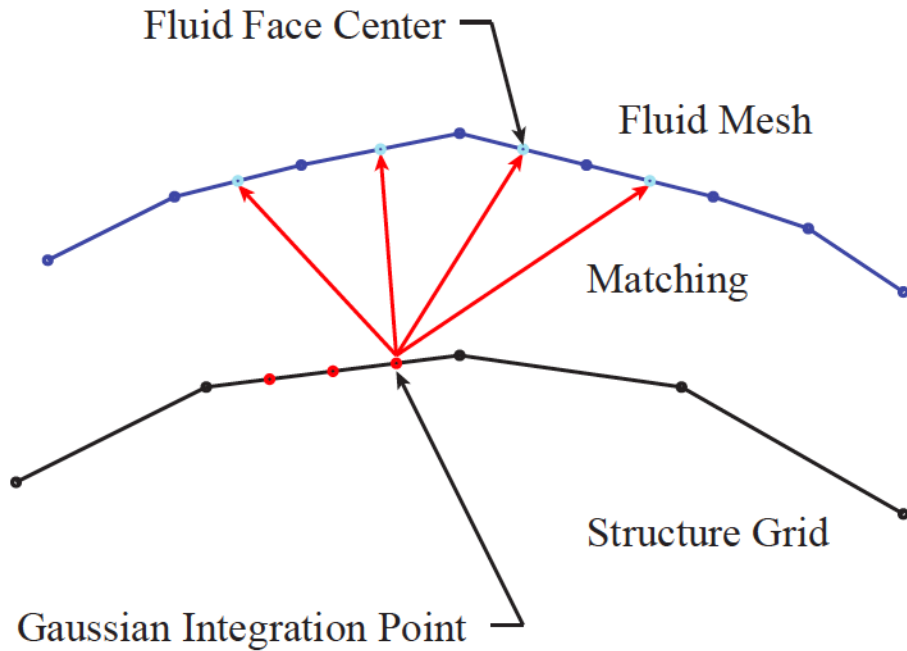
Figure 2.3: Fluid-to-structure mapping Piro (2013)

For coupling the fluid to the structure, two boundary conditions are possible. The exact boundary condition uses the structure displacements to deform the fluid mesh and apply the correct velocities to the fluid boundary. The approximate boundary condition uses the structure velocities on the body boundary to impart the correct

velocities on the fluid patch without deforming the mesh. The approximate boundary condition is consistent with the assumption of small deflections, and can be used to reduce the computational expense and inaccuracies of deforming the fluid mesh, shown by Piro and Maki (2013). The difference between the two boundary conditions will be further examined in Chapter III.

It is common to assume small deflections when modeling steel hull structures. Using the approximate boundary condition on the fluid patch and the modal decomposition of the structure allows for a large reduction in computational expense. Piro (2013) found that for complex ship slamming simulations, using only the first 100 frequencies, the FSI solver had similar computational times to the rigid body simulations. The modeling of hydroelastic effects for steel hull structures is accomplished with reasonable computational cost using the FSI solver.

CHAPTER III

Hydroelastic Analysis of a Simple Plate

This chapter presents a canonical problem which is used to model wetdeck slamming impacts. The problem is set up so it can be modeled in two-dimensions, allowing analytical slamming models to be evaluated. A numerical model, analytic model, and experimental data are compared with the FSI solver in order to verify and validate the solver and further understand the underlying physics that are important when modeling this type of impact problem.

The simplified problem uses a flat plate free-surface impact as a way to model a wetdeck structural panel experiencing a slamming load. The flat plate is dropped at varying heights onto a wave with varying radius of curvatures, or a calm (flat) free-surface. During the impact, the speed of the flat-plate is assumed to be constant or close to constant since the time duration of the impact is short and the plate is modeling only a small portion of the overall mass of the multi-hull structure. The structure and fluid problem are modeled in two-dimensions to isolate and study the hydroelastic effects. The case setup chosen to compare with experimental results is shown in Figure 3.1.

The flat plate is 0.5 m long and 8 mm thick and made of steel. The impact test condition chosen to simulate is a 0.5 m drop height corresponding to an nominal constant velocity impact of 2.5 m/s. The wave radius of curvature is 10.2 m, which
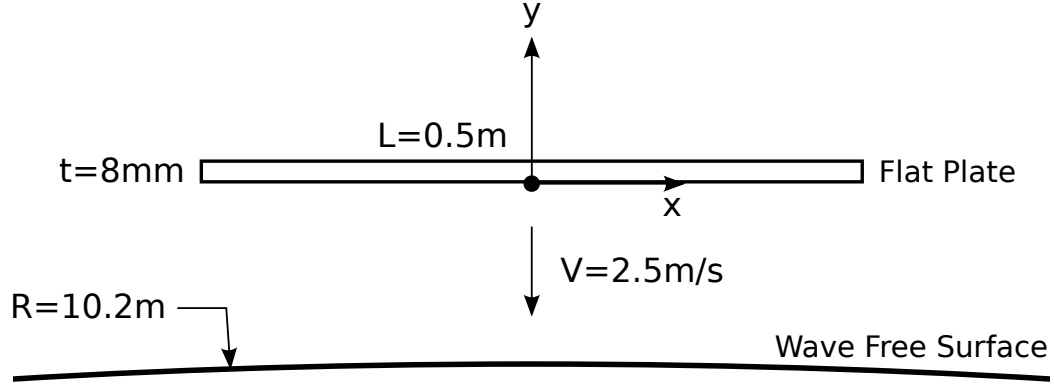
Figure 3.1: Flat plate drop setup

is flat enough that an air pocket is captured between the plate and the wave surface at impact. The air pocket was observed in the experimental tests and the numerical simulations. The wave radius of curvature is given as,

$$R = \frac{1}{ak^2} \tag{3.1}$$

where a is the wave amplitude and k is the wave number. The detailed analysis of the hydroelastic behavior is focused on the deflections and strains at the center of the plate, corresponding to $x = 0$.

3.1 Convergence Study

A rigorous study of the convergence behavior of the FSI solver is conducted in this section. The convergence of the structure from the FEM, fluid from the CFD, and the combined fluid and structure algorithm is analyzed. Convergence is determined using grid refinement and iteration studies. Results are used to make parameter selections for the FSI solver.

3.1.1 Structure

The plate is modeled in Abaqus using two-dimensional beam elements. A symmetry condition is used for the structure and the fluid solution located at the center of the flat plate. The boundary conditions at the ends are a symmetric boundary condition at $x = 0$ m and a pinned boundary condition with a torsional stiffness at $x = 0.25$ m. The torsional stiffness is provided from Faltinsen et al. (1997) as a stiffness per unit width. This stiffness was measured from the experimental setup. Abaqus solves the modal decomposition of the structure. The natural frequencies and mode shapes are provided to the FSI solver. The first six mode shapes from from the FEM are shown in Figure 3.2.
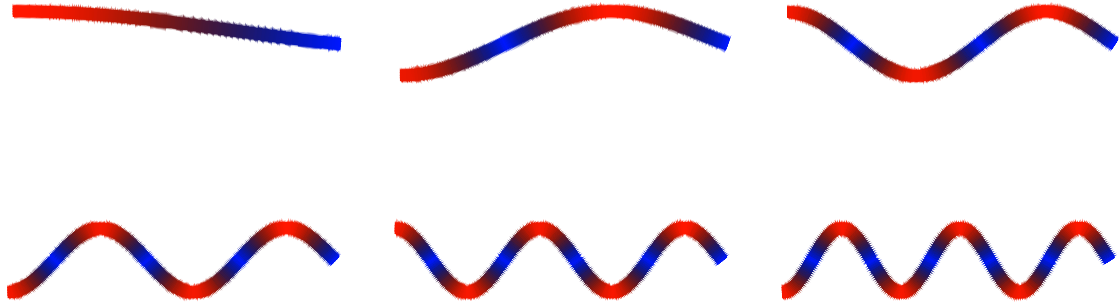
Figure 3.2: First six mode shapes from Abaqus

By varying the number of beam elements, Abaqus results were used to study the sensitivity of the modal frequencies as a function of the number of elements in the FEM. Frequency results for selected modes between 5 and 200 are shown in Figure 3.3 and the frequencies for the first 10 modes are provided in Table 3.1.

The modal analysis of a structure usually contains the majority of the structural energy in the first couple of modes, which correspond to the lowest frequencies. For a small number of beam elements the first 10 modes have already visually converged. The higher frequencies require more resolution before they converge. Resolution is
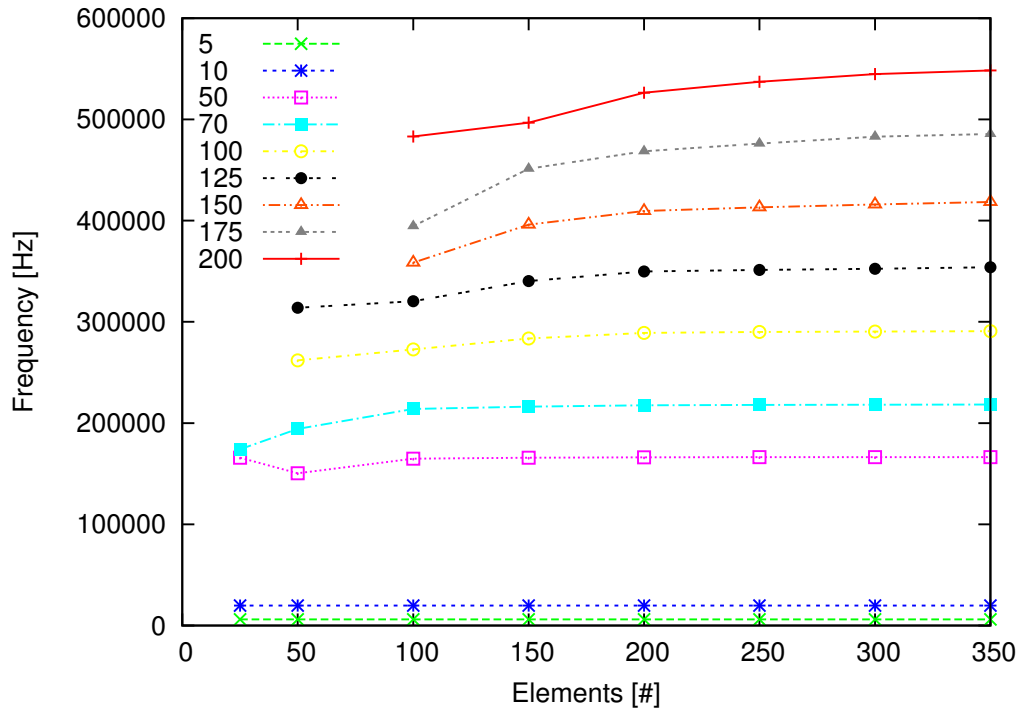
Figure 3.3: Convergence of mode frequencies verse number of beam elements

	Modal Freq. [Hz]					
Elements	50	100	150	200	250	300
Mode 1	119.13	119.13	119.12	119.12	119.12	119.12
Mode 2	741.59	741.54	741.53	741.53	741.52	741.52
Mode 3	1939.40	1939.10	1939.00	1939.00	1939.00	1939.00
Mode 4	3699.40	3698.30	3698.10	3698.10	3698.00	3698.00
Mode 5	5991.80	5989.40	5989.00	5988.80	5988.80	5988.70
Mode 6	8778.50	8774.30	8773.50	8773.20	8773.10	8773.00
Mode 7	10409.00	10410.00	10411.00	10411.00	10411.00	10411.00
Mode 8	12016.00	12010.00	12009.00	12009.00	12009.00	12009.00
Mode 9	15659.00	15653.00	15652.00	15651.00	15651.00	15651.00
Mode 10	19662.00	19658.00	19658.00	19657.00	19657.00	19657.00

Table 3.1: Convergence of Modal Frequency

added by increasing the number of beam elements. For this problem, 300 beam elements were selected to study the effects of higher frequencies and local peak pressures from the fluid. A large number of beam elements allows for the proper structural resolution to capture the high frequencies and local peak pressure forcing effects.

An advantage to using the modal analysis of the structure is reducing the degrees-of-freedom needed to solve the structure. This is done by truncating the total modes available that capture the majority of the structural energy. To determine where the structural energy is contained for this problem, a fluid grid with 0.625 mm resolution and 10 iterations was selected based off the studies in Sections 3.1.2 and 3.1.3 respectively. Simulating a flat plate impact on top of a 10.2 m radius wave curvature using a constant velocity impact at 2.5 m/s, the modal forces were integrated for the first 40 modes to determine the total structural energy during the simulation. Each modes force was then integrated and divided by the total structure energy to determine the percentage of modal energy of each mode during the impact. The modal force is plotted for the first nine modes in Figure 3.4 and the percentage of the total energy and cumulative energy of the structure is given in Table 3.2.

Mode #	Total Energy [%]	Cumalitive Energy [%]
1	99.99445	99.99445
2	0.00506	99.99951
3	0.00038	99.99989
4	0.00007	99.99996
5	0.00002	99.99998
6	0.00001	99.99999

Table 3.2: Structural energy for the first six modes during a two-dimensional flat plate impact

The largest contribution to the total structural energy is contained in the first mode shape as see in Figure 3.4 and Table 3.2. Other modes are excited at the initial impact, but quickly damp out. The first mode shape continues to vibrate at the wetted natural frequency after the initial impact. The contribution to the structural
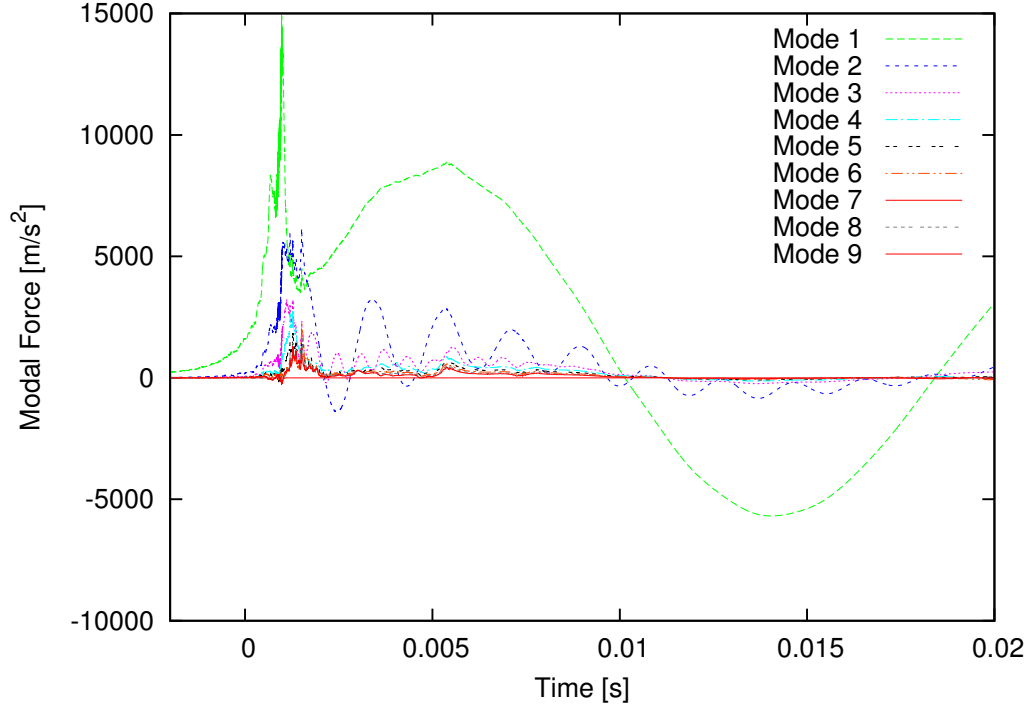
Figure 3.4: Modal forcing during a 2.5 m/s constant velocity impact on a 10.2 m wave curvature radius

energy decreases as the mode frequency increases. It is important to capture the total structural energy without selecting unnecessary higher mode frequencies that have a limiting time step criteria for the one-way coupling algorithm. Adding higher frequencies decreases the maximum time step size for stability of the one-way coupling structure solution leading to more time expensive simulations. The higher frequencies can suffer from accuracy with the two-way coupling algorithm if a small enough time step is not taken. From this simulation, nine modes are selected for the remaining simulations as this is sufficient to capture the majority of the structural energy.

3.1.2 Fluid

The fluid grid also utilizes a symmetry boundary condition at $x = 0$. The CFD grid is a two-dimensional grid with local refinement near the hydroelastic patch. Figure 3.5(a) shows the cell density of the selected CFD grid. Figure 3.5(b) shows

the phase indicator, α, on the grid where a value of one or zero is a cell containing only water or air respectively, and a value in between one and zero is the location of the free surface interface. Cells above the hydroelastic patch are removed to reduce computational cost.

(a) Two-dimensional CFD grid   (b) Alpha field modeling the wave surface
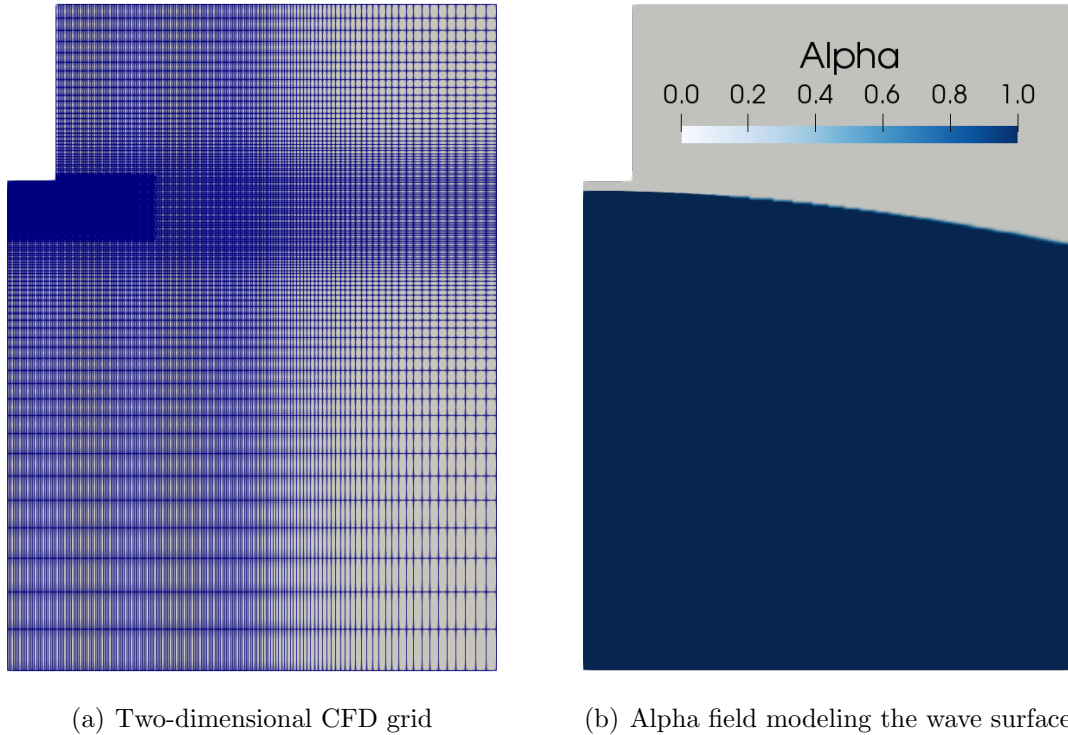
Figure 3.5: Fluid grid setup for flat plate drop simulations

The convergence of the fluid solution is analyzed by conducting a spatial resolution study for the CFD grid. A rigid simulation of the flat plate drop using the same conditions in Section 3.1.1 is set up without the structure coupling. Pressure at 0.1 m from the center of the plate is plotted for varying resolutions along with experimental data in Figure 3.6. Also the total force per unit length acting on the plate is plotted in Figure 3.7.

The peak pressure increases as the resolution increases. The peak pressure time occurs earlier when the resolution is too coarse. The experimental data has a lower pressure peak due to the hydroelastic effects compared to the the rigid simulations,
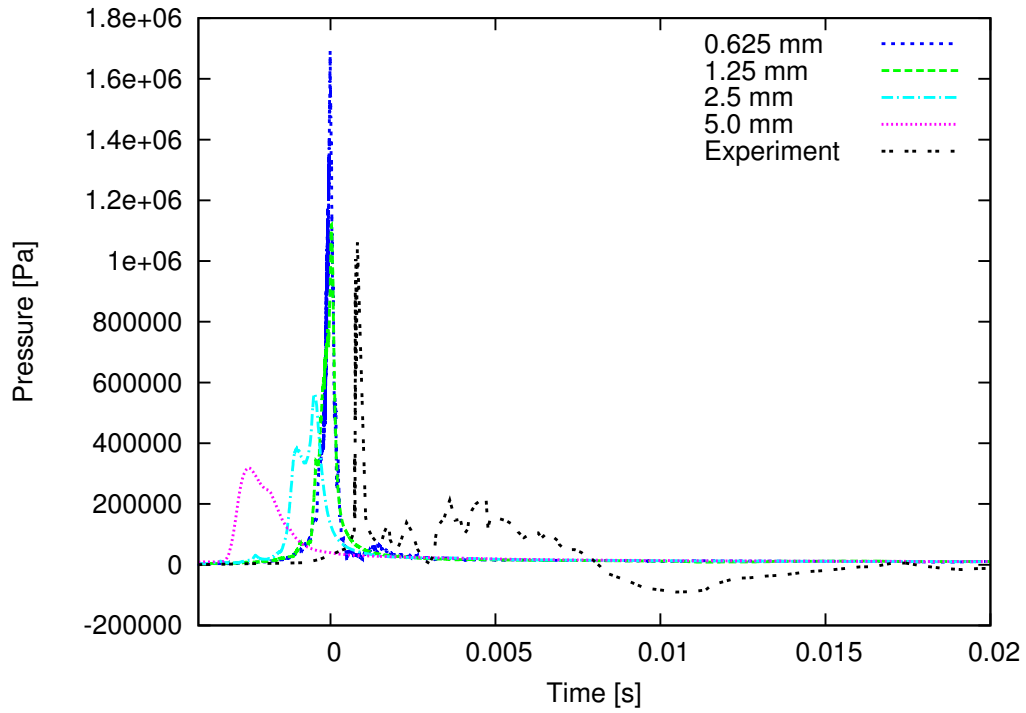
Figure 3.6: Pressure during a rigid flat plate slam at 0.1 m from the plate center
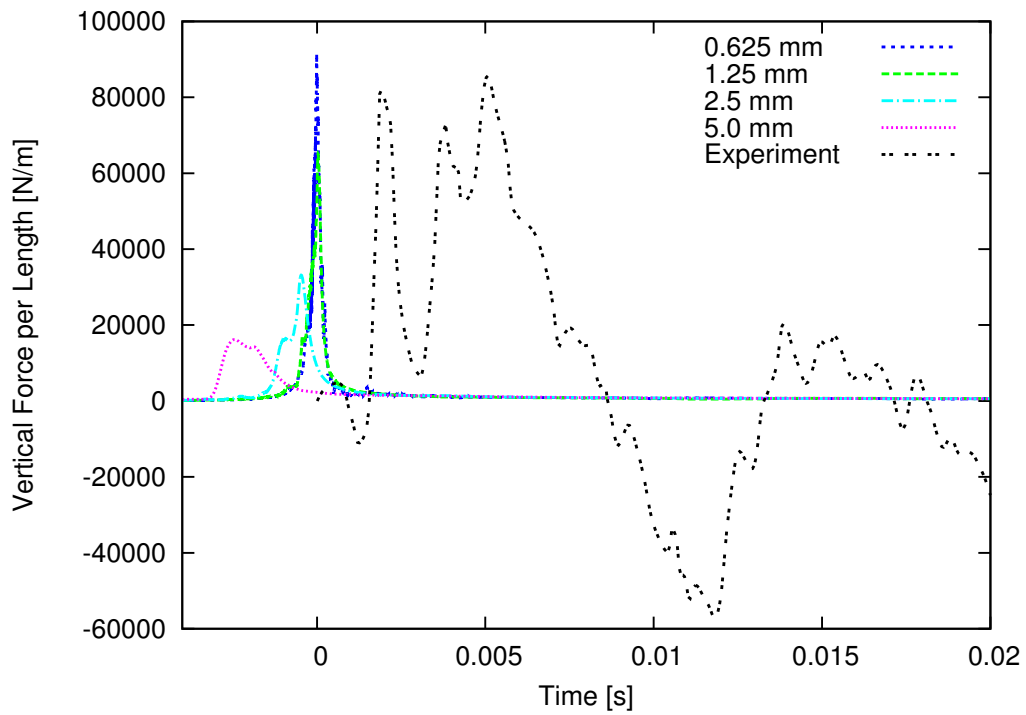
Figure 3.7: Total forcing per unit length of a rigid flat plate slam

which have enough resolution to capture the pressure peak. The pressure peak happens during the impact stage and then approaches a constant value due to the rigid plate and constant velocity boundary conditions. After impact, the experimental pressure values continue to oscillate at the first wet natural frequency since the plate is still oscillating at this frequency. Smaller, higher frequency oscillations are also seen in the experimental pressure data shortly after impact due to higher modes, air entrapment and mixing.

The vertical force per unit length of the flat plate also exhibits similar trends to the pressure on the plate. However, the numerical peak force is closer to the experimental peak force. The finest grid resolution still over predicts the experimental data as expected for a rigid simulation. The oscillations in forcing are not present for the rigid simulations as these are due to the hydroelastic effects for the experimental forcing data.

The fluid grid resolution selection is important for capturing the correct forcing while maximizing the time step stability criteria to reduce computational expense. A finer resolution requires smaller time steps. Peak pressures are not as important to the response of the structure if the peak pressure occurs over a short time. Similarly, the peak forcing on a structure is only critical to the response if the impulse force is large. For the two-dimensional simulations, the 0.625 mm resolution translates to only 242,000 cells and so the finest resolution is used for the two-dimensional simulations to more closely model the fluid dynamics. For three-dimensional simulations, coarser resolutions can be used to reduce computational cost, as long as the forcing is sufficiently resolved.

3.1.3 Fluid-Structure Coupling

The mapping scheme between the fluid and the structure is discussed by Piro and Maki (2013). The scheme assumes that the CFD grid has more resolution than the

FEM as is typical between the two different numerical models. This allows for the fluid and structure grids to be made independent of each other as mesh generation and refinement zones are typically different for each model. Both the fluid and the structure grids are modeled in two-dimensions. However, for transferring pressure to a force and to model the torsional stiffness of the end boundary condition a unit width is given to the CFD and FEM grids. Figure 3.8 shows the mapping of the first modes eigenvector magnitudes at the 301 structure node points to the 400 fluid cell faces for the CFD grid. A visual inspection of the mapping scheme shows the fluid grid matching the structure nodes. The symmetry condition is at the center of the plate at $x = 0$ m and the pinned torsional boundary condition is on the right at $x = 0.25$ m. The structure has 300 beam elements and the fluid has 400 cells along the mutual patch.
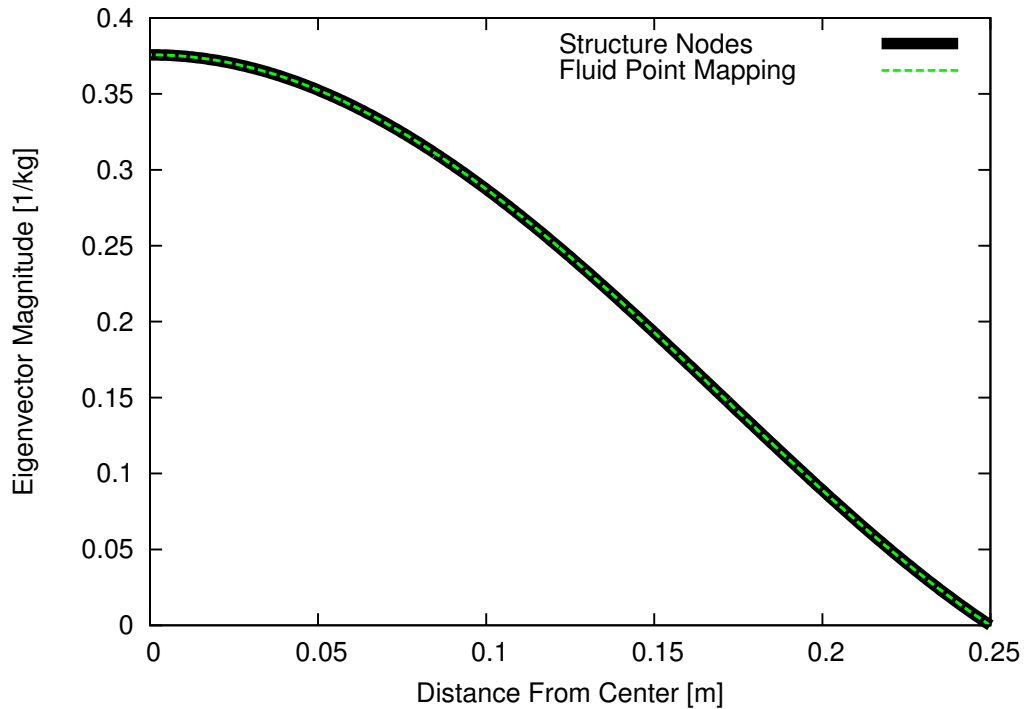
Figure 3.8: Mapping of the eigenvectors magnitudes at the structure node points to the fluid faces

The convergence of the FSI solver is analyzed through the number of modes used

31
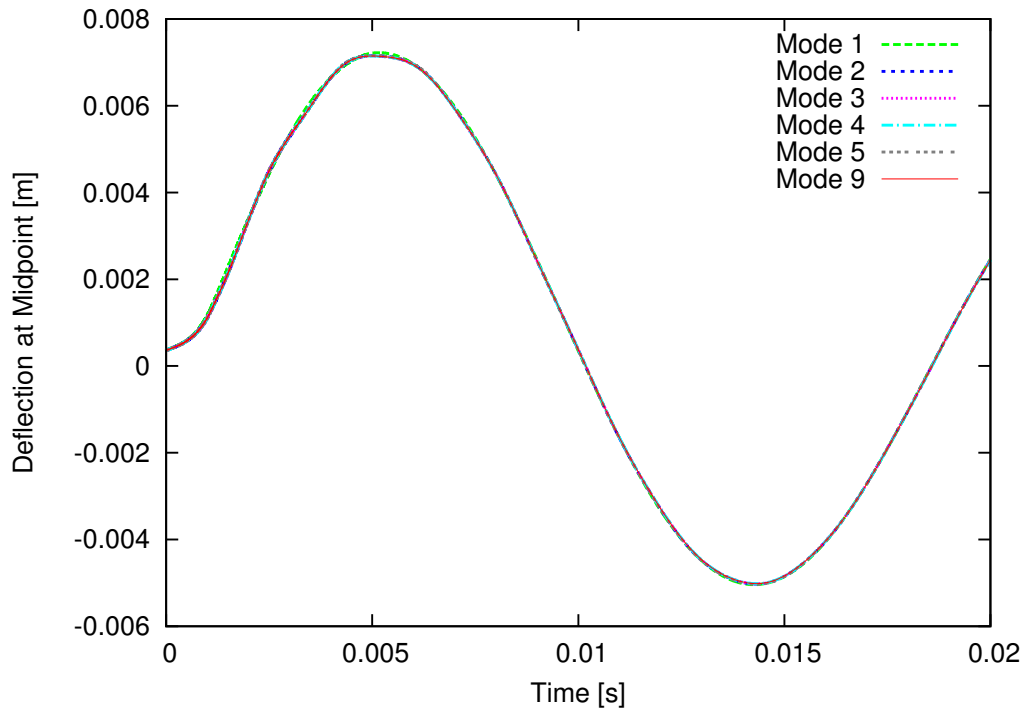
Figure 3.9: Convergence of deflection at the center of the plate for different number of modes
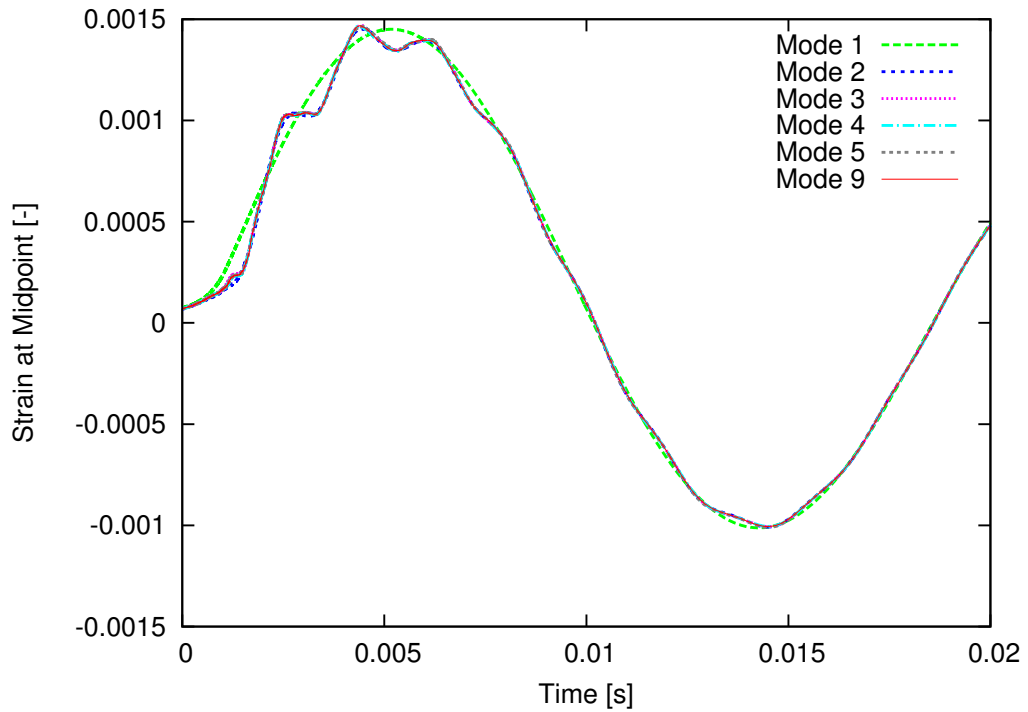
Figure 3.10: Convergence of strain at the center of the plate for different number of modes
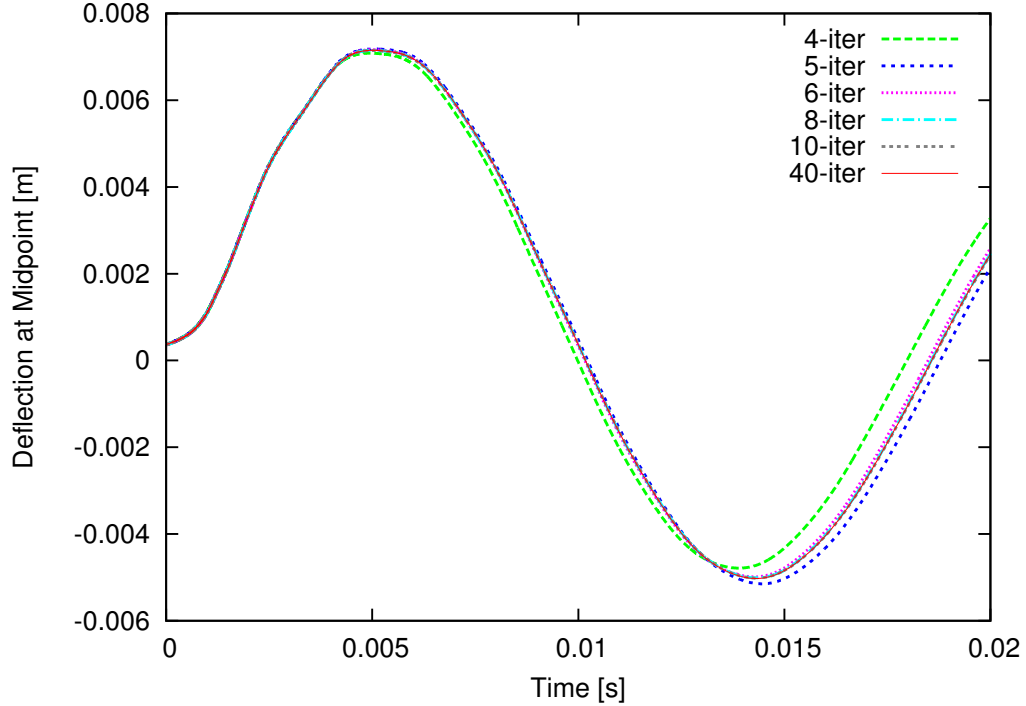
Figure 3.11: Convergence of deflection at the center of the plate for different number of iterations with a fixed inertial under-relaxation factor of 1.7 for all modes

on the structure side and the number of iterations needed for the algorithm to converge. The stability of the FSI solver is discussed in more detail in Chapter IV. The number of iterations needed is largely dependent on the inertial under-relaxation factor used. This problem uses the conditions outlined from the previous two sections with an inertial under-relaxation factor Γ_e of 1.7 or a modal added mass γ of 4.4 for all modes. The first convergence test analyzed uses 10 iterations and varies the number of modes. This test is a secondary test for Section 3.1.1 and confirms the number of modes needed for the structure.

Figures 3.9 and 3.10 confirm what is presented in Section 3.1.1. The majority of structural energy is contained in the first mode shape which is already visually converged for the deflection at the center of the plate. The strain at the center of the plate is visually converged after adding the second mode which contains the second most structure energy. With this in mind, nine modes are selected for the remaining
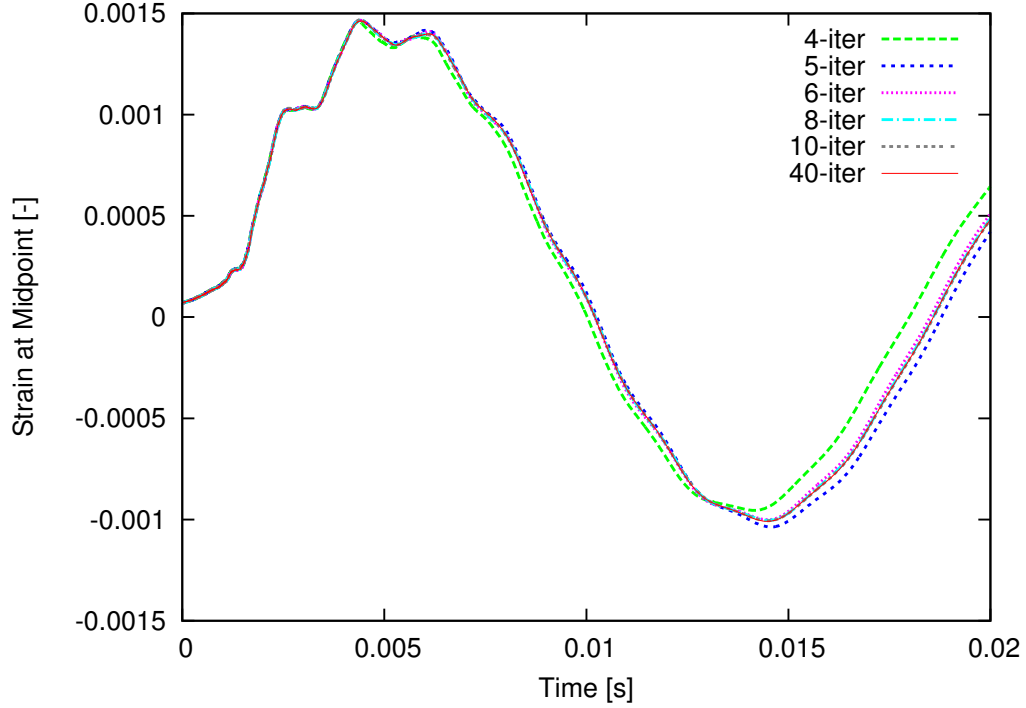
Figure 3.12: Convergence of strain at the center of the plate for different number of iterations with a fixed inertial under-relaxation factor of 1.7 for all modes

analysis. For the convergence of the FSI solver, the number of iterations between the fluid and the structure is evaluated in Figures 3.11 and 3.12.

The convergence of the FSI solver is clearly visible in the frequency of oscillation after impact. A large number of iterations - up to 40 - were plotted to insure that the algorithm was converged. Deflection and strain is shown to converge after six iterations, which corresponds to six fluid solves and five structure solves. For the remaining simulations, 10 iterations are used to ensure convergence and the added expense is still small enough for this two-dimensional problem.

3.2 Experimental Validation

Experimental test data is available for this flat plate drop problem. Results were obtained from Faltinsen et al. (1997) as well as the description of the setup and some

detailed data. The tests were conducted at the MARINTEK wave basin in Norway. A steel and stiffened aluminum section were tested, but detailed results were only given for the steel section. Dummy plate sections were placed on either side of the test plate section to reduce the three dimensional effects for comparisons with two dimensional slamming models. Pressure, acceleration, strain, and displacement measurements of the test section were taken at several locations. The plates were dropped on flat free-surfaces as well as the top of waves with varying radius of curvature. The dry structural natural frequencies and torsional rigidity of the plate connection points were experimentally determined before the flat plate drop. The total weight of the rig setup was 500 kg to model a constant-velocity impact. Data for comparative studies was only provided for a drop height of 0.5 m, which corresponds to a nominal impact velocity of 2.5 m/s, and a wave radius of curvature of 10.2 m for the steel test section.

(a) Top view.   (b) Profile view.
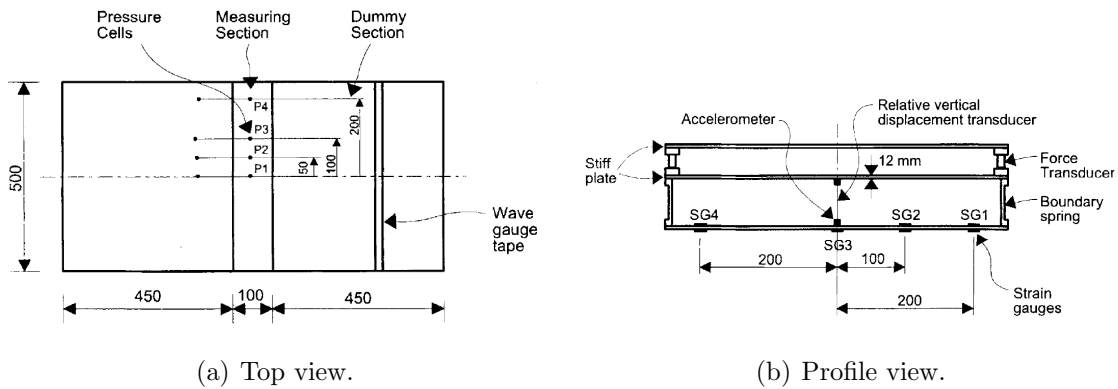
Figure 3.13: Flat plate drop test setup (Faltinsen et al. (1997)).

An overview of the test rig is presented in Figure 3.13. The instrumentation of the test rig is provided with locations for pressure probes, strain gauges, force transducers, and displacement transducer. Data for strain (SG3) and deflection is only provided at the center of the plate test section. Comparisons with the FSI solver for validation will focus on these measurement points.

3.2.1 Boundary Conditions

Three-dimensional effects are assumed negligible for the flat plate drop, so the FSI solver comparisons use a two-dimensional fluid grid with Euler beam elements representing the plate structure as described in the previous sections. Both a constant velocity and free drop condition is simulated to compare the constant velocity assumption to the actual drop speed. A comparison of the drop speed velocities for the simulations and experiment is shown in Figure 3.14.
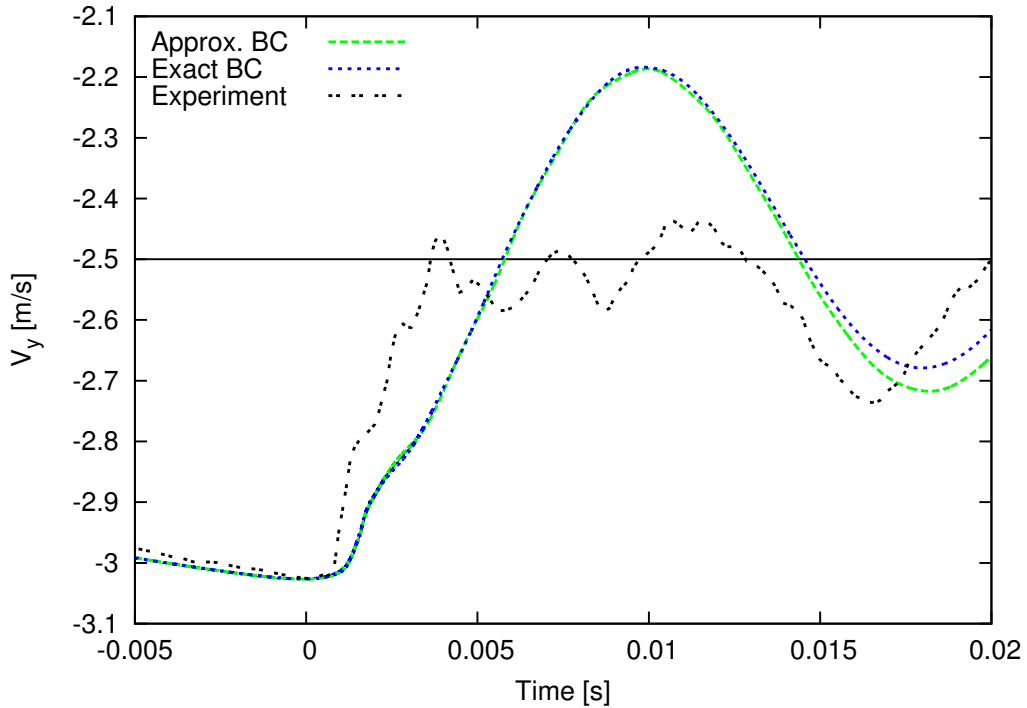
Figure 3.14: Free drop velocity of test rig for simulations and experiment

The free drop simulations solve a single degree-of-freedom rigid body motion equation that starts at rest 0.5 m above the wave crest to model the velocity impact. The motion solver impacts the wave crest at approximately 3.0 m/s and rapidly slows to a velocity of approximately 2.5 m/s during the impacting stage. The simulation velocities for the exact and approximate FSI boundary conditions have the same initial impact speed and then decelerate at the same rate. The difference between the exact and approximate boundary conditions is discussed in Section 2.4. The approximate

boundary condition does not influence the initial impact speed were the maximum deflection and strain occurs. The constant velocity assumption of 2.5 m/s is the solid black line on the graph and is approximately the average of the experimental velocity shortly after impact. The simulations do not show the small oscillations around 2.5 m/s which may be due to a combination of the two-dimensional assumption, compressibilty effects, and differences in the actual impact angle of the plate during the experiments. The FSI solver's exact and approximate boundary conditions are further compared for different impact velocities in Figures 3.15 and 3.16.
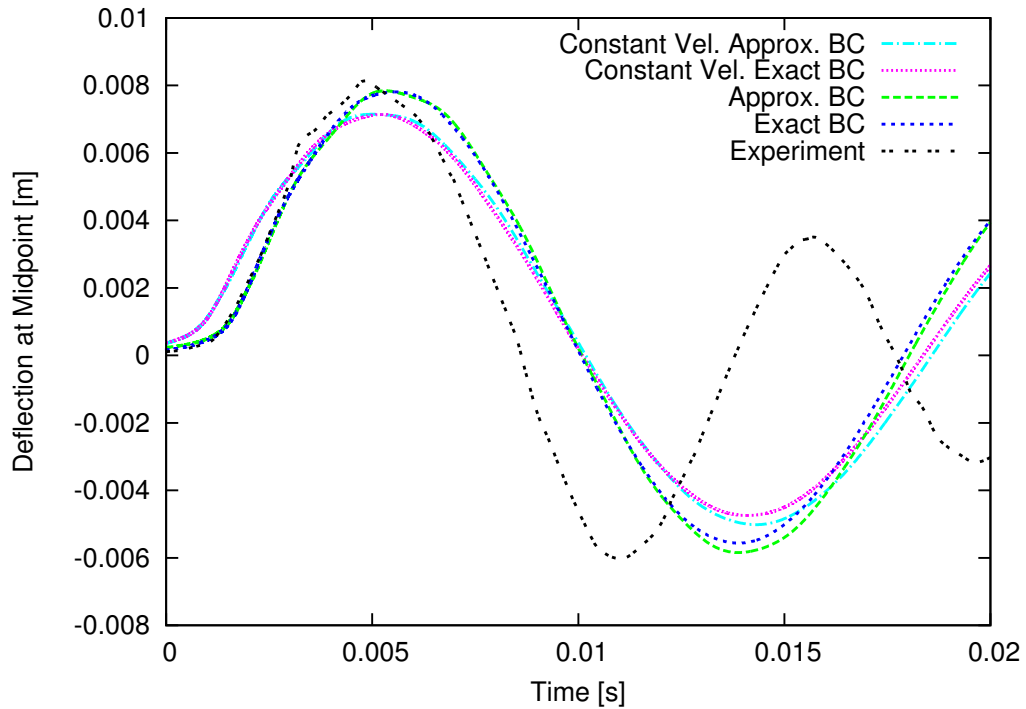
Figure 3.15: Deflection for different FSI solver boundary conditions

The free drop impact case is similar to the constant velocity impact case, but the constant velocity impacts underpredict the maximum deflection. The two FSI solver boundary conditions, exact and approximate, show similar results for each impact speed when looking at the deflections at the center of the plate. The strains are more sensitive to the hydroelastic effects and show differences in the higher frequency oscillations for each test case. However, the variable of most importance is the maximum
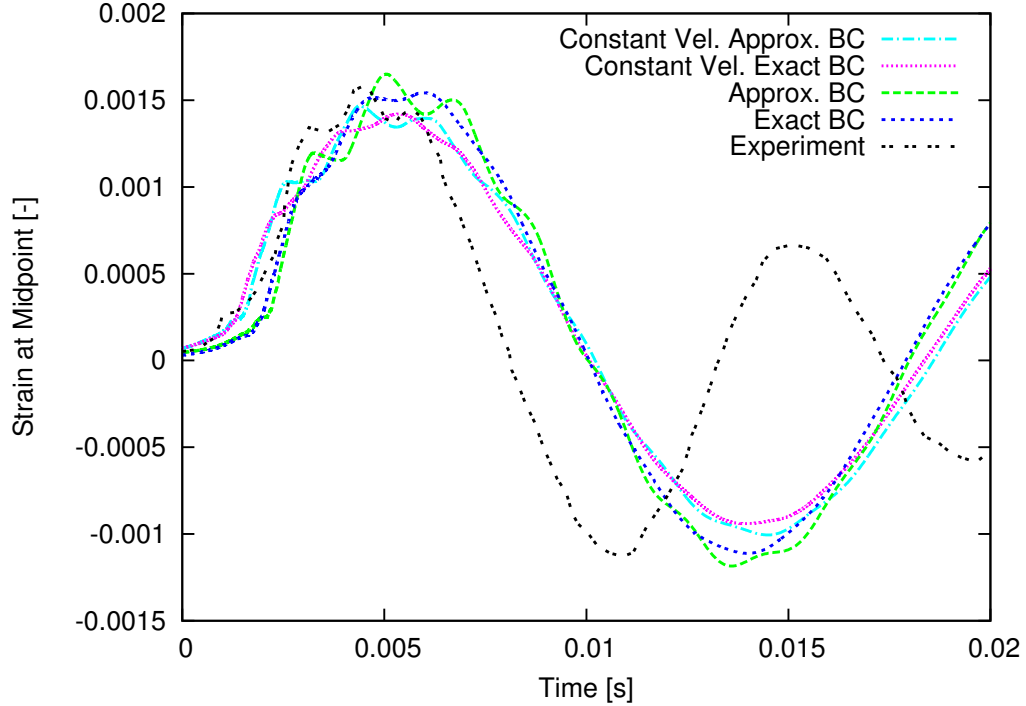
Figure 3.16: Strain for different FSI solver boundary conditions

strain. When comparing the maximum strain between impact speeds, the maximum strains are similar. The free drop condition matches the experimental results better than the constant velocity impact as expected. The constant velocity impact has a slight advantage in improved computational costs, and for similar impact problems may provide a decent assumption for impact models that require a prescribed velocity. It is important to note that a similar impact problem requires a larger rigid body mass when compared to the hydroelastic structural mass for the validity of this assumption to remain true. The close comparisons between the approximate and exact boundary conditions shows that for small deflections the approximate boundary condition can be used. Using the approximate boundary condition avoids the additional computational cost in morphing the mesh, which adds additional iterations in the FSI algorithm.

The main difference between the FSI solver and experimental results are in the primary oscillation frequency after impact. There are several modeling differences

between the simulations and experiments that may contribute to the different oscil-lation frequency. The simulations assume a perfectly symmetric fluid and structure domain. The experimental setup required the test rig to be dropped on a moving wave. The wave crest at impact, during the experiments, did not exactly hit at the center of the plate. This, combined with the horizontal velocity of the wave, means that the fluid loading on the structure was never symmetric in the experiments. The experimental plate test section was welded to the test rig at the plate ends. The tor-sional stiffness at the ends of the plate were experimentally measured and assumed to be symmetric. The measured torsional stiffness is applied as a symmetrical bound-ary condition in the simulation model. This symmetric assumption in the structural boundary conditions in reality is not true as the two welds are different and create an asymmetric boundary condition. The sensitivity of the structure boundary conditions is demonstrated in Figures 3.17 and 3.18.
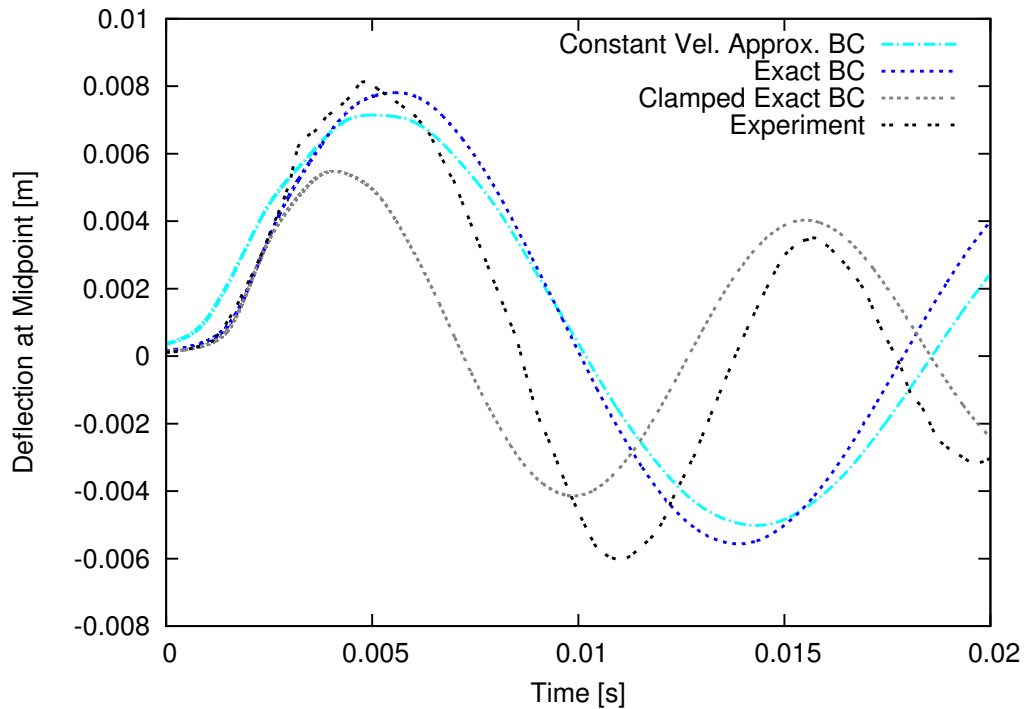
Figure 3.17: Deflections for different structure boundary conditions

The free drop condition with the exact boundary condition is chosen, since this

39
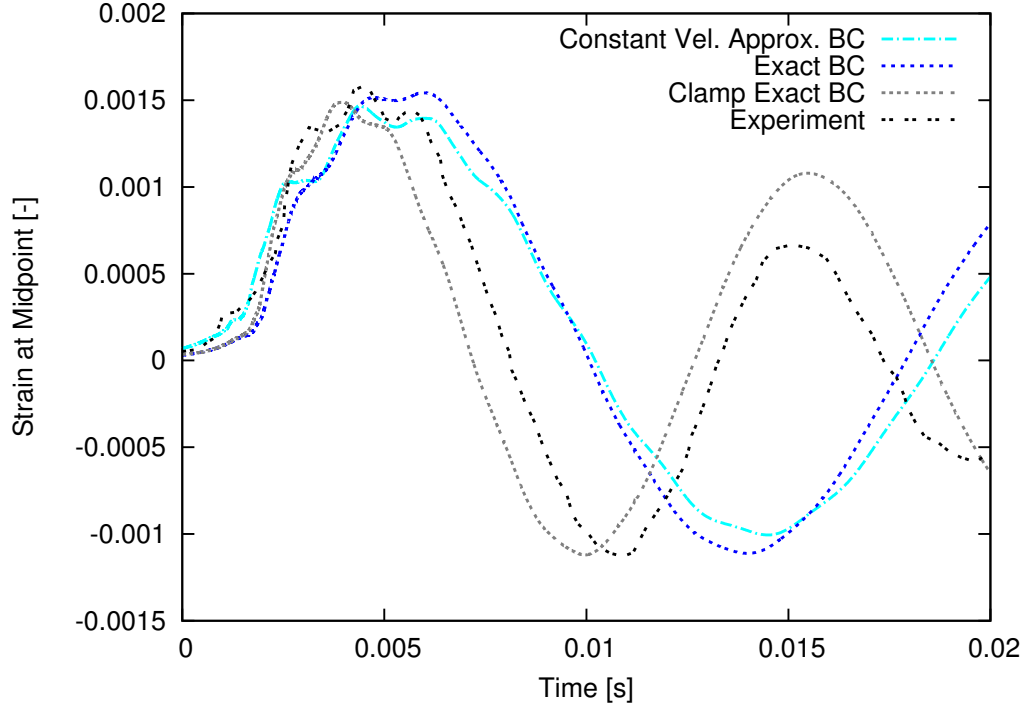
Figure 3.18: Strains for different structure boundary conditions

simulation is closest to the maximum results at the center of the plate. The structure boundary condition at the ends is changed from the experimentally measured torsional stiffness to a clamped condition. The main oscillation frequency matches the experimental results, but the maximum deflection is underpredicted. However, the maximum strain is still closely captured. The main frequency of oscillation and maximum deflection is sensitive to the structure boundary conditions. An asymmetry in the plate welds at the ends of the plate, compressibility effects, and cavitation may contribute to the difference in oscillation frequency and deflection results at the center of the plate. Figure 3.19 shows the fluid grid for the free drop condition with the exact boundary condition close to the maximum deflection at time 0.004831 seconds. The deflection of the plate and the mixing of the air pocket that is captured at impact are visible.

The oscillation period and reduction in amplitude of the second oscillation for the deflection and strain may also be explained from the missing physics in the simu-
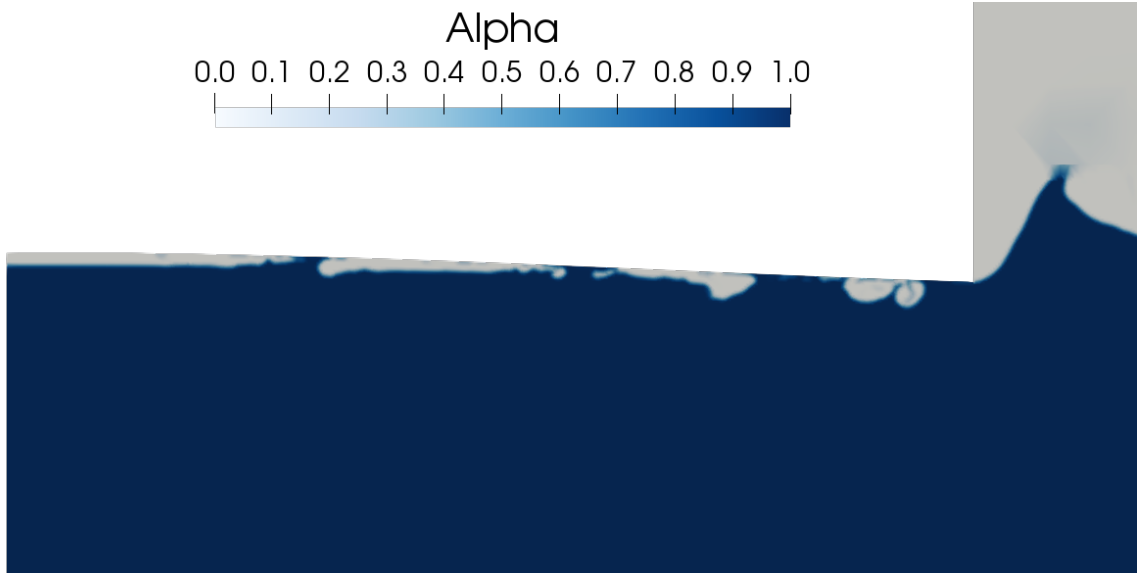
Figure 3.19: Two-dimensional free drop with exact boundary condition close to maximum deflection

lations. The experiments have observed air entrapment at impact with ventilation and cavitation also occurring around 0.01 s. The FSI solver simulates the air entrapment during impact, but the solver does not account for the compressibility of the air captured. Kvalsvold and Faltinsen (1995) state that modeling the compression is not necessary for the maximum structure response. Modeling the compression could influence the response of the structure during the second oscillation frequency. The FSI solver does not model cavitation when the pressure approaches vapor pressure. In the experiments, cavitation was not analyzed so the contribution of the structure response from cavitation is difficult to quantify. Structural damping may also play a role in the reduction of amplitudes in the second oscillation. Structural damping is modeled as a percentage of the structure velocity. A constant structural damping parameter of 2% is used for all simulations and modes.

The torsional stiffness at the plate ends was experimentally measured and converted to a torsion per unit width. The two-dimensional beam model used a unit width to model the full rig setup including the dummy plate components. The ex-

perimentally measured torsional stiffness is applied as a boundary condition at the plate ends in the FEM model. Information on the dummy plates was not provided, but stated that the dummy plates were similar to the test section plate. The measured natural frequencies of the first three modes are compared to the FEM natural frequencies in Table 3.3.

Mode [#]	Exp. [Hz]	FEM [Hz]	Diff. [%]
1	125	119	-4.8
2	375	-	-
3	800	745	-6.9

Table 3.3: Dry structural frequency comparisons with experiments

The unit width beam element model closely matches the experimental results. The second natural frequency is an asymmetric mode which is not captured with the symmetry boundary condition used for the two-dimensional beam element model. Since the fluid loading on the structure is also symmetric, the asymmetric mode is not excited during impact. The dry frequencies are close to the experimentally measured values and differences may be attributed to the experimental error, inaccuracies in modeling the dummy plates, and the assumption of symmetrical boundary conditions when measuring the torsional stiffness at the plate ends.

3.2.2 Structure Sampling

Post-processing stress and strain in FEA may have inaccuracies depending on where the sampling point is positioned on an element. FEA solves for the structure displacements and velocities at the nodes. The formulation of elements use interpolation functions to solve for the structure solution contained in the element between the node points. The interpolation functions used are called shape functions. Shape functions are C_0 continuous between elements. For deflections and rotations the shape functions will have the same value at shared node points for any element. However, the interpolation of stress and strain, which uses the derivatives of the shape functions,

at the nodes may be different for each element. The stress and strain interpolations are most accurate at the Gauss points, and can yield large inaccuracies at the node points. There are many sampling post-processing techniques for stress and strain that can be used to avoid large inaccuracies.

Sampling of stress and strain at the nodes is a common request in the design analysis of a structure. FEA post-processing tools use stress smoothing techniques to interpolate stresses and strains at the node points. The formulation of an element involves the use of Gauss points to integrate over the element. At the Gauss points, the stress and strains are most accurate. Stress smoothing techniques use the stress and strain interpolation at the Gauss points in various ways to interpolate to the node points - for example, taking the stress at the closest Gauss points for each element that attaches to the node and averaging the stresses. In Figure 3.20, the deflection at the center of the plate is shown for different number of beam elements. The deflection at the center element Gauss point does not have a noticeable difference from the node points and is omitted from this plot. Figure 3.21 shows the strains at the center Gauss point of the element closest to the center of the plate for different number of beam elements. Inaccuracies of strain interpolation at the node located at the center of the plate is shown in Figure 3.22.

The center of the flat plate, modeled by beam elements, lies on a node point with a symmetry boundary condition. The Gauss points are at the center of the element that connects to the node modeling the center of the plate. As more beam elements are used, the Gauss points approach the true center of the plate. After 50 beam elements are used, the strain interpolation at the Gauss points is no longer sensitive to the distance from the center of the plate and the deflections are converged.

The strain interpolation at the nodes becomes more inaccurate with increasing elements and does not match the converged strain from interpolations at the Gauss points. Adding beam elements increases the overprediction of strain at the center to
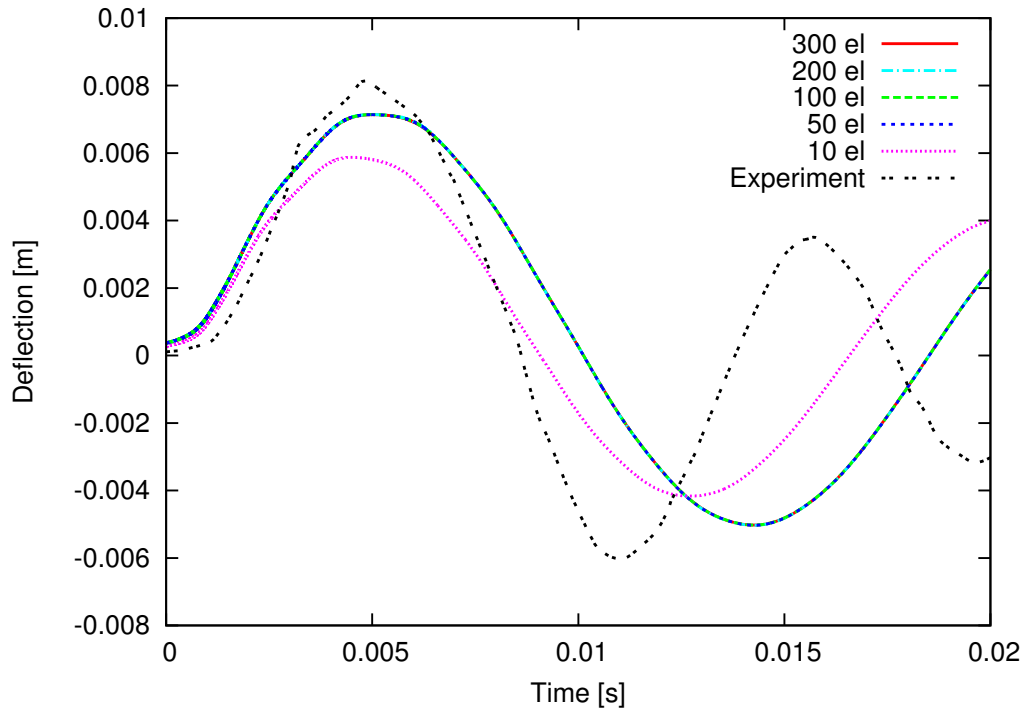
Figure 3.20: Deflection near center point for different number of structure elements
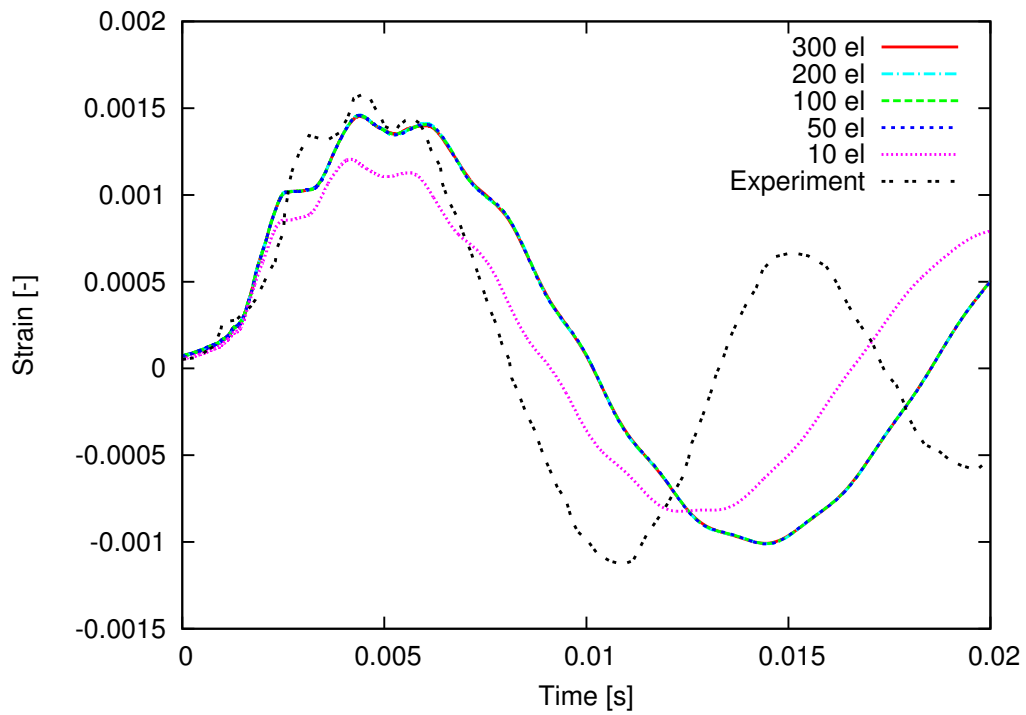
Figure 3.21: Strain sampled at the center Gauss point of the element
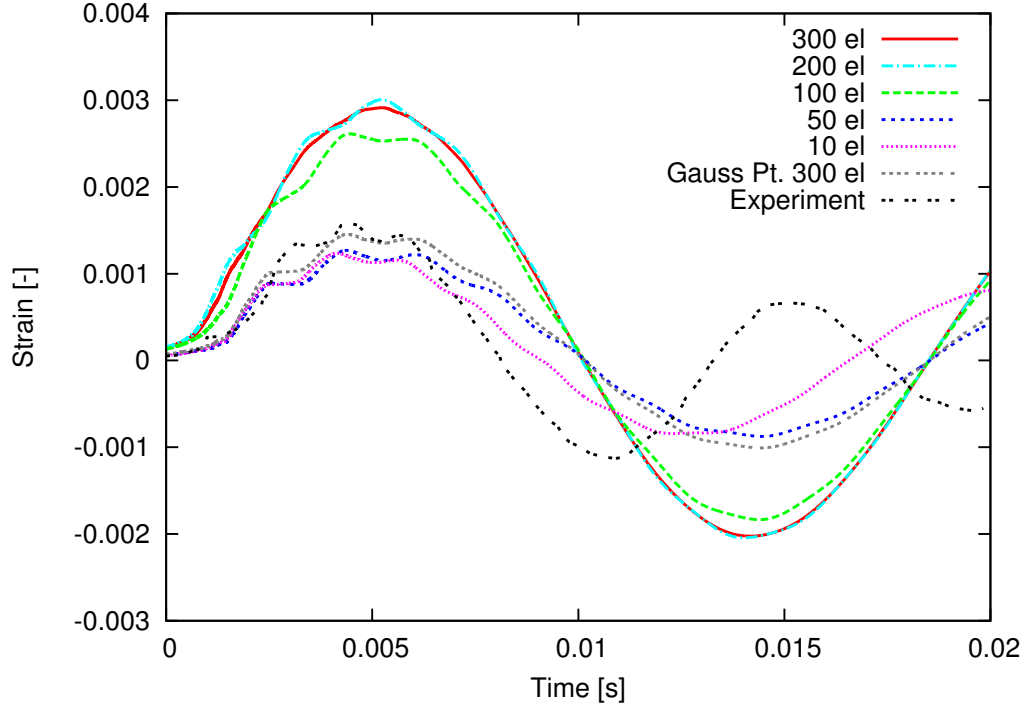
Figure 3.22: Sampling of strain on the node point at the center of the plate

almost twice the measured experimental strain. The strain measured at the Gauss points converges after 50 elements and does not show large inaccuracies with increasing number of elements. This shows the importance of sampling stress and strain at the Gauss points and using a smoothing technique to interpolate to the nodes. The FSI solver does not employ a smoothing technique, so care is taken to sample the structure at a Gauss point.

3.2.3 Structure Non-Linearity

Two types of structural non-linearity that are omitted when using a modal analysis are geometric and material non-linearity. The FSI solver only handles the modal decomposition of the structural model. Thus, a one-way coupling utility is developed to couple the rigid pressure loads from the fluid patch to the FEM in Abaqus to study the sensitivity of the non-linear structural effects.

The three-dimensional geometry of the plate test section is modeled with plate

elements in Abaqus. The full test rig in three-dimensions is modeled for the rigid CFD grid. Rigid pressures from the CFD grid are mapped to the structure model using Abaqus's Python wrapper. The Python utility then solves the structure for the next time step and repeats the mapping for the next pressure time history. The measured torsional stiffness from the experiments is scaled to 0.1 m, the width of the plate test section for the structural model. The dummy plates on the test rig are not modeled in the structural model since the geometric description of the dummy plates is not provided. This increases the primary oscillating frequency after impact when compared to the experiments since the dummy plates were wider than the test section at 0.45 m on either side and contained a larger proportion of mass compared to the test section. However, maximum strain measurements at the center of the plate are still similar to the experimental results when acoustic elements are used. The difference between a one-way and two-way coupling is shown in Figure 3.23.
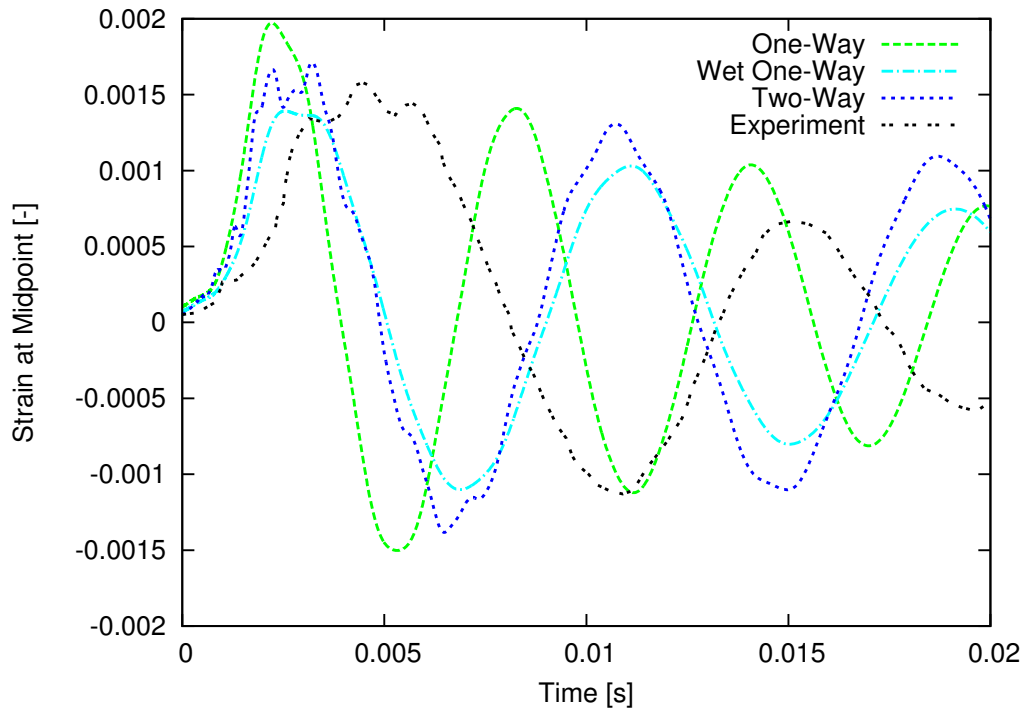
Figure 3.23: Comparison of one-way and two-way three-dimensional flat plate drops

Hydroelastic effects are responsible for the differences between the one-way and

two-way coupling results. The added mass is captured in the two-way coupling, causing the structure to oscillate at a lower frequency. The one-way coupling oscillates at the dry frequency. The rigid slamming pressures are larger during the initial impact and the dry structure captures higher excitation frequencies causing the maximum strains to be larger for the one-way coupling without acoustic elements. Acoustic elements model the structure as fully wetted which reduces the excitation of the structure from higher frequency content in the fluid forcing. However, the rigid forcing does not capture the hydroelastic effects, because the fluid does not experience the change in velocity due to the structure motion, which is captured by the two-way coupling. When studying the structural non-linearity, the hydroelastic effects are neglected to save computational cost and compare just the geometric and material non-linear effects.

A modal decomposition of the structure is used to reduce the number of degrees-of-freedom by linearizing the response of the structure into a finite number of mode shapes. This linearization neglects the non-linear effects that can occur in the geometry when the full FEM model is solved. A comparison between the full FEM model solved using the one-way Abaqus coupling tool and the one-way modal analysis is presented in Figure 3.24.

Between the linear modal results and the non-linear geometry there is an increase in the oscillation frequency. In addition, the non-linear structure responds to local forcing effects, causing small amplitude higher frequency oscillations. These local forcing effects are filtered out in the linear modal results. These effects are not shown in the experimental data and may be caused by the hydroelastic and compressibility effects that are not modeled.

Material non-linearity is more difficult to model and requires experimental tests to be modeled accurately. Non-linearity in materials occur when a structure's elastic behavior on the stress strain curve does not have a constant slope (constant Young's
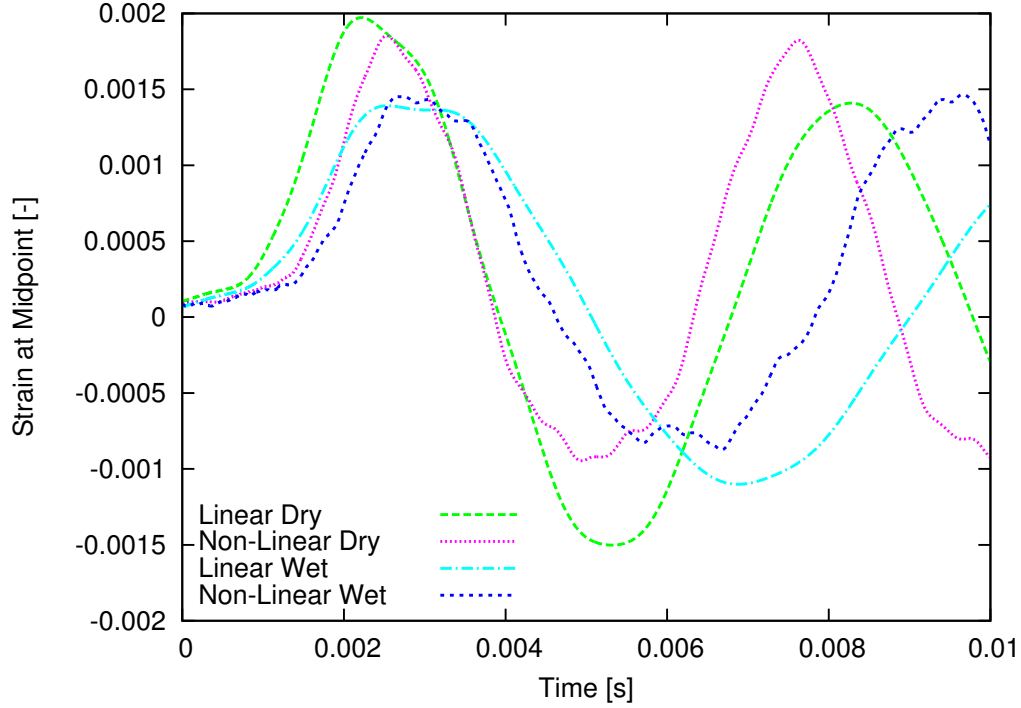
Figure 3.24: Non-linear geometry effects

modulus, E), or when the yield stress of the material is exceeded and plastic deformations occur. The material listed in the experiments was High-Strength Low-Alloy (HSLA) steel. There are several different types of HSLA steel and the exact specifications were not provided. Three types of HSLA steel were chosen with low, medium, and high yield stresses. An elastic-plastic model for non-linear material is setup with the one-way Abaqus coupling utility. Figure 3.25 shows results for the non-linear material simulations. These simulations also contain the non-linear geometry effects.

The elastic simulation models the high strength HSLA steel as the yield stress is never met so the structure material responds in the elastic range only. This is the same result as the non-linear dry simulation in Figure 3.24. The medium and low grade HSLA steels have yield stresses of 360 MPa and 260 MPa respectively. The material is modeled as elastic until the stress in the element exceeds the yield stress then the material is modeled as plastic. The medium grade HSLA steel simulations barely

48
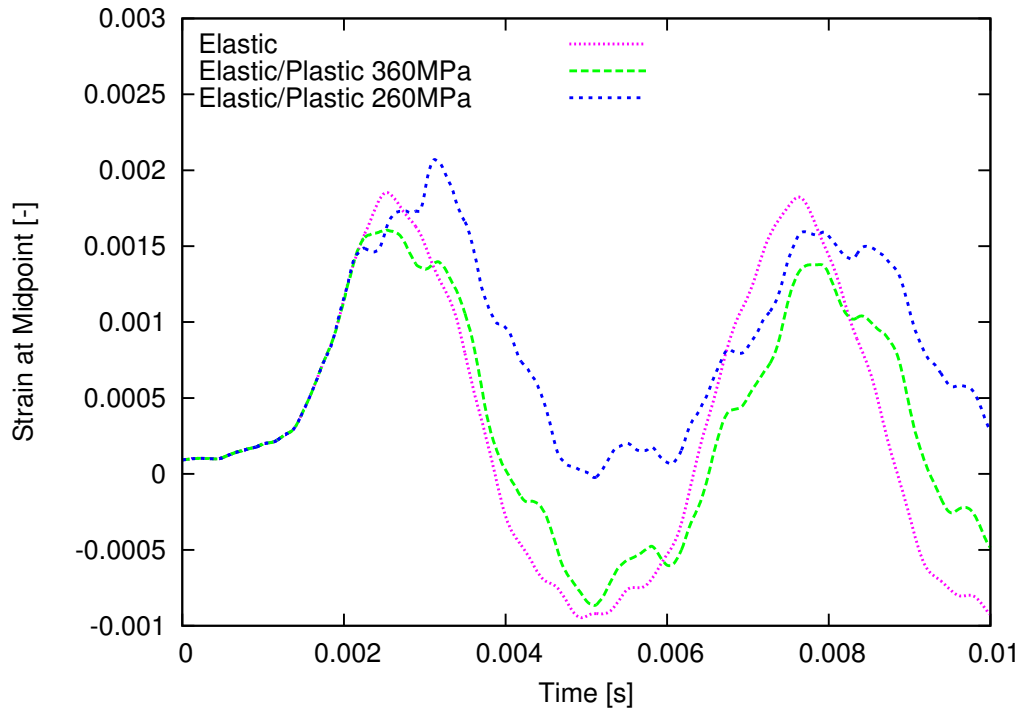
Figure 3.25: Non-linear material effects

exceed the yield stress which causes a small reduction in maximum strain. Higher frequency content is present, but the main oscillation frequency is reduced after the first oscillation. The low grade HSLA steel exceeds the yield stress early in the impact and the large plastic deformations are shown by a shift in the oscillations about zero strain to approximately 0.001 strain. A higher maximum strain is captured and the main oscillation frequency is increased when compared to the high grade HSLA steel.

Non-linear effects can change the maximum strain and frequency-of-oscillation during impact. The non-linear geometry may be more sensitive to compressible effects by responding to local higher frequency forcing components from the incompressible fluid solution. Using a modal solution filters out the local high frequency forcing. Based on this analysis, modeling non-linear effects is not important for this problem, but would be important if the yield stress of the material is exceeded.

3.2.4 Analytical Modeling

Two numerical methods that use analytical functions to model the hydrodynamic loading on a flat plate slam are compared with the experimental and FSI solver results. The first method by Kvalsvold and Faltinsen (1995) models the impact problem using a generalized Wagner theory to account for the time dependent wetted length. The second method by Faltinsen et al. (1997) has several simplifications that are made based off of the results of the first method. The deflections and strains at the center of the plate for the numerical methods, FSI solver, and experimental results are presented in Figures 3.26 and 3.27.
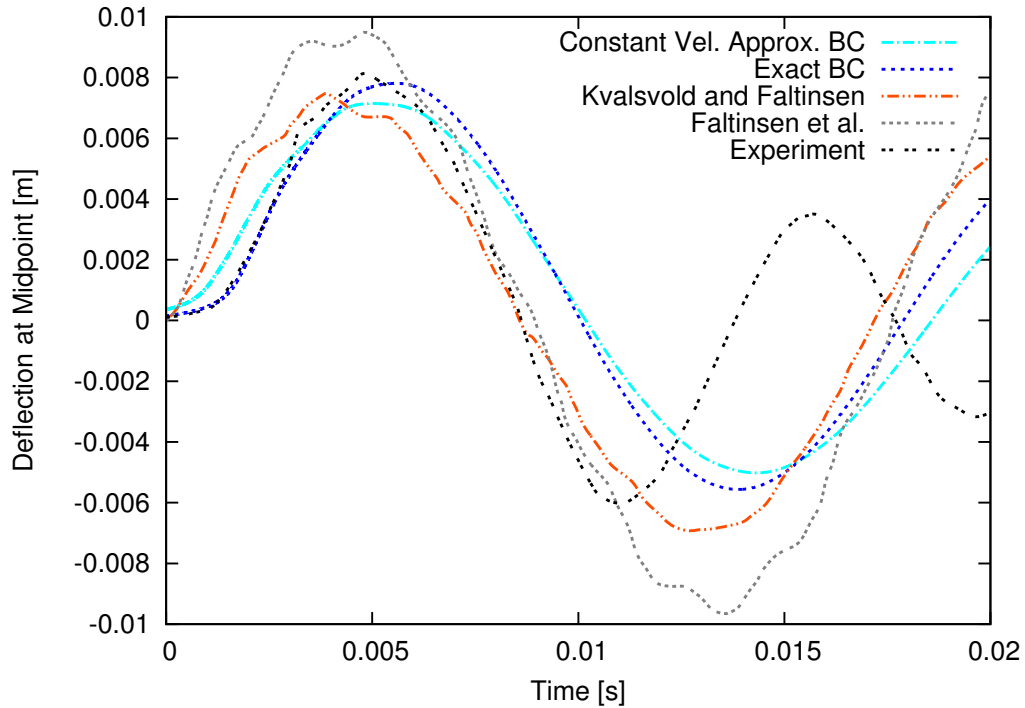
Figure 3.26: Deflection comparisons with analytical models

The two numerical methods and FSI solver oscillate at the same first wetted natural frequency of the structure. However, the excitation of the second symmetric frequency in the two numerical methods does not damp out like the experimental and FSI solver results. This leads to large overpredictions of the maximum strain of 18% and 47% for Kvalsvold and Faltinsen (1995) and Faltinsen et al. (1997), respectively.
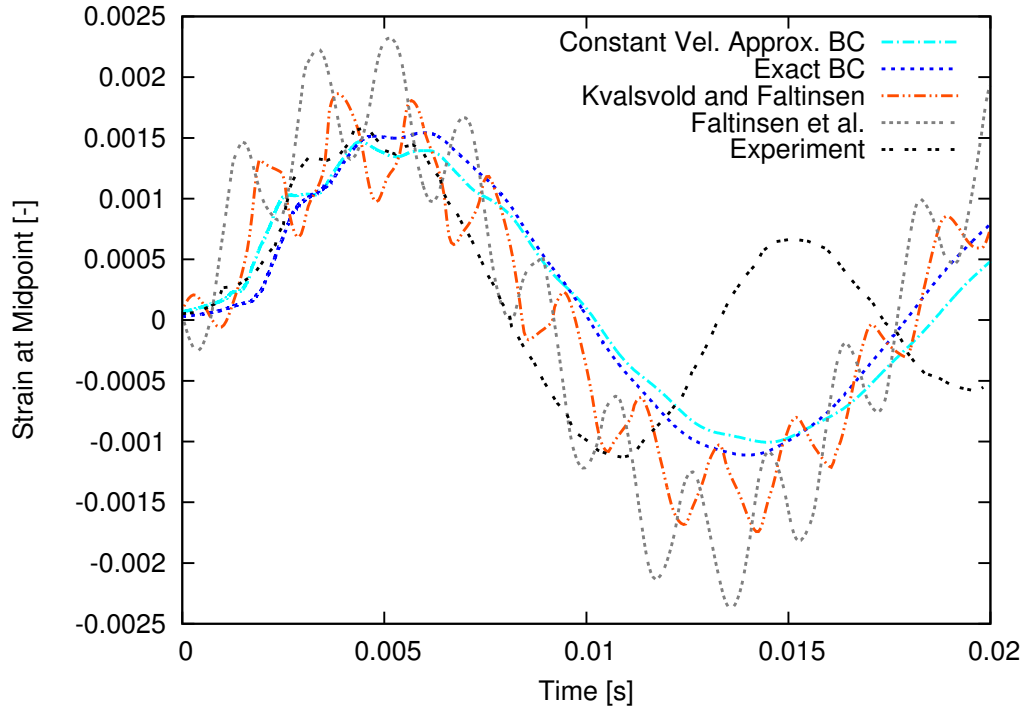
Figure 3.27: Strain comparisons with analytical models

Faltinsen et al. (1997) does not solve for the time dependent wettness of the structure during impact and assumes a fully wetted structure. The Kvalsvold and Faltinsen (1995) method captures more of the physics during the initial impact and compares better with the experimental results when compared with the symplifications made by Faltinsen et al. (1997). The two numerical methods and the FSI solver do not model the cavitation that occurs around 0.01 seconds which is why the frequency of oscillations are different from experiments after the maximum deflection and strain. Maximum deflections from Kvalsvold and Faltinsen (1995) and the FSI solver are close to experimental results, but the simplifications by Faltinsen et al. (1997) lead to an overprediction of maximum deflection by 17%. These simplifications add to the overprediction of the maximum strain, but both numerical models suffer from large oscillations from the secondary symmetric natural frequency that are not present in the experiments.

To relate the two-dimensional slamming models and experimental results to re-

alistic wetdeck slamming events, Faltinsen et al. (1997) proposes a non-dimensional maximum bending coefficient, k, formulated as

$$k = \frac{|\sigma_{max}|}{V_{ave}Z}\sqrt{\frac{I}{\rho ELW}} \tag{3.2}$$

where σ_{max} is the maximum stress, V_{ave} is the average impact velocity, Z is the distance from the neutral axis to the measured maximum stress, I is the cross sectional area moment of inertia, ρ is the impacting fluid density, E is the modulus of elasticity, L is the length of the plate between transverse stiffeners, and W is the width of the plate between longitudinal stiffeners. The non-dimensional maximum stress values are calculated for the four FSI solver simulations and the two numerical methods and plotted with experimental results in Figure 3.28.
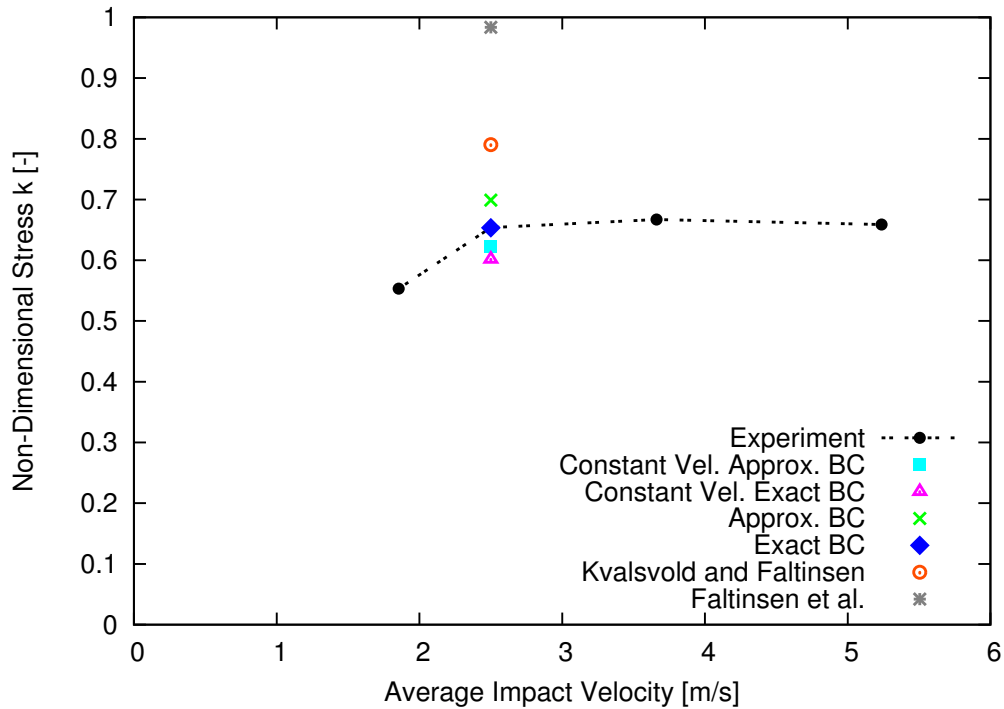
Figure 3.28: Non-dimensional stress at center of the plate

The non-dimensional stress parameter uses an impact velocity instead of a maximum pressure as is common in classification rules. Relating the maximum stress to an impact velocity is more consistent with experimental results, where large variations

in maximum pressures are captured and are sensitive to small differences in surface features during an impact, but do not influence the maximum stress in the structure. However, determining the average impact velocity has sensitivity issues as to the time window that the average velocity is calculated for. The average impact velocity of 2.5 m/s has an initial impact speed of approximately 3.0 m/s before decelerating to the averaged value. Kvalsvold and Faltinsen (1995) use the actual velocity recorded during the experimental results, while the exact and approximate FSI simulations solve for the rigid body motions during impact. The constant velocity FSI simulations and Faltinsen et al. (1997) use the average impact velocity 2.5 m/s as the fixed drop velocity. The constant velocity assumption for the FSI simulations decreases the predicted maximum stress, while the approximate boundary condition increases the maximum stress. The FSI simulation solving for the rigid body motions and using the exact boundary condition captures the maximum stress with a difference of approximately 2.4% from the experimental results. The approximate boundary condition has a difference of 4.4% and the constant velocity simulations have differences of 7.2% and 10.1% for the approximate and exact boundary conditions respectively. This provides further validation that capturing the correct velocity during impact is one of the important factors to model when determining the maximum stress.

Predicting maximum stress during a slam impact is important for the analysis of an adequate structure design, as it may be the maximum condition that a structure experiences during its lifetime. For the flat plate impact case, the FSI solver closely matches experimental data for maximum deflection and maximum strain at the center of the plate when modeling the correct impact velocity. Modeling the impact velocity accurately has the most significant effect on capturing an accurate maximum stress in the structure. Linear potential models can be used to predict the relative impact velocity on the wetdeck and use the non-dimensional stress factor k to determine loading on the wetdeck structure. Future work could involve validating the non-

dimensional stress factor for different impact velocities.

CHAPTER IV

Adaptive Inertial Under-Relaxation Factor

Coupling CFD and FEA with two-phase flows presents a unique challenge when compared to single-phase flow analysis. The primary challenge is in accurately modeling the time-dependent wetness of a body, and this has direct implications on the added mass of the body and response of the structure. In marine flows, the two-phases typically modeled are water and air. Water is approximately 850 times denser than air. This difference leads to large time variations in added mass of a marine structure during a slamming event. For catamaran structures with flat wetdecks, there is a substantially large variation in added mass between normal operations with a dry wetdeck and during an impact with time varying wetness on the wetdeck. The VoF approach allows for the tracking of the time dependent wetness and the total forcing, including the added mass forcing, of a marine structure. Large differences between the added mass and the hydroelastic structural mass, will cause the FSI solver to be unstable when using a tightly-coupled segregated algorithm. This is due to the artificial added effects from delay in information transfer between the segregated algorithms as discussed in Young et al. (2012). For pitching hydrofoils, Young et al. (2012) proposes a hybrid coupling method to estimate the added mass and improve convergence. For the FSI coupling using the full FEM, Veldman et al. (2018) proposes a quasi-simultaneous coupling method that uses the mode shapes to provide

an estimate of the structure displacement to the fluid instead of using inertial under-relaxation. Yvin et al. (2014) estimates added mass of rigid six degree-of-freedom body using unit accelerations provide to the fluid during run time, but states applying this technique to deformable structures is not straight forward. The new method proposed in this chapter uses an inertial under-relaxation technique to stabilize the FSI solver on the structure side. During runtime, an estimate of the modal added mass is calculated for each mode and used to provide an inertial under-relaxation factor for the next time-step. An analysis of the stability criteria for the FSI solver, as it pertains to the added mass effects, is described in this Section 2.4. Further details on the convergence of the solver and estimating the added mass are provided in this section for an adaptive inertial under-relaxation factor.

4.1 FSI Solver Stability

Large added mass effects are experienced during a slamming event and can destabilize the FSI solver. These added mass effects are related to the modal accelerations, $\ddot{q}_m$, of the modal added mass in Equation 2.12. The forcing due to added mass during a slamming event can be quite large and dominate the forcing term. To analyze this effect, consider Equation 2.12 where the modal forcing, f_m, is composed of a component of modal added mass, γ_m, along with a time dependent forcing, $\tilde{f}$. The modal added mass is the ratio of the added mass contribution from the mode to the modal structural mass of that mode. The modal added mass varies for each mode. If the modal added mass is larger than 1, meaning the added mass contribution is more than the modal structural mass, the FSI solver can become unstable. An inertial under-relaxation method is used shown in Equation 2.8 to stabilize the FSI solver. $[\Gamma]$, is a square matrix with non-zero values along the diagonal corresponding to the inertial under-relaxation factor for each mode. A detailed stability analysis for the FSI solver is presented in Section 2.4 and further stability information is presented

in Piro and Maki (2013).

The coupling algorithm's stability is independent of the the time step and relies on choosing an inertial under-relaxation factor that is related to the modal added mass by Equation 2.14. A large value for Γ, may insure stability, but convergence is governed by the magnitude of Γ. Minimizing Γ will speed up convergence and reduce the number of iterations for each time step of the FSI solver. This leaves the choice of stability and convergence to an estimate of the modal added mass. An estimate of the modal added mass, proposed by Mesa and Maki (2017), can be obtained by comparing the dry, ω_d, and wet, ω_w, natural frequencies of each mode,

$$\gamma_m = \frac{\omega_d^2}{\omega_w^2} - 1. \tag{4.1}$$

Many FEA programs have the ability to include acoustic elements to solve for the wet natural frequencies. The wet natural frequencies are smaller due to the added mass effects when compared to the dry natural frequencies. Each mode will have an independent added mass estimation that indicates that mode's participation to the added mass effects. Using acoustic elements in a FEM adds additional elements and degrees-of-freedom to the analysis. This increases computational time for the FEA program to solve for the modal decomposition. The wet frequencies of the dry mode shapes may be difficult to decipher as mode shapes pertaining to the acoustic elements are also generated. For complex geometries, comparing the wet and dry frequencies to estimate the modal added mass becomes time intensive for computations and matching the wet frequencies to the dry frequencies. The order between dry and wet modes may not be the same and this can introduce error matching the dry and wet frequencies. Mismatching the dry and wet modes leads to a miscalculation that can under or over predict the modal added mass. Another method for estimating the modal added mass to determine the inertial under-relaxation factor is described in the next section.

4.2 Runtime Modal Added Mass Estimation

Estimating the modal added mass using Equation 4.1, presents challenges for complex geometries. An estimate for added mass during the simulation runtime would eliminate the need for estimating the added mass before the simulation. A runtime estimation of added mass could reduce the computational expense and potential for a failed simulation due to instability associated with an under estimation of the added mass during pre-processing. With a few assumptions of the forcing, a runtime estimation of the added mass is described in this section.

During a slamming event, the forcing due to added mass for each mode in Equations 2.12 is assumed to be much larger that the forcing from other components,

$$|\gamma_m \ddot{q}_m| >> |\tilde{f}| \rightarrow f_m \approx -\gamma_m \ddot{q}_m. \tag{4.2}$$

Assuming the modal forcing is dominated by the added mass effects, the modal forcing is approximated to be the modal added mass forcing. Under the small time step assumption the estimation for modal acceleration using the first order finite difference scheme, Equation 2.9, the time dependent modal added mass for each mode is determined,

$$\gamma_m = -\frac{f_m}{\ddot{q}_{m,est}}. \tag{4.3}$$

The estimate for the modal mass may be determined for each iteration during a single time step. This estimation allows for an inertial under-relaxation factor to be calculated using Equation 2.14. Analyzing the this estimation and developing a adaptive inertial under-relaxation algorithm is presented in the following section.

4.3 Runtime Adaptive Inertial Under-Relaxation Factor

A runtime adaptive inertial under-relaxation scheme is developed using the runtime estimation of the modal added masses. For each iteration k and each mode, Equation 4.3 becomes,

$$\gamma_m^k = -\frac{f_m^k}{\ddot{q}_{m,est}^k}.$$ (4.4)

The maximum modal added mass over the old time step iterations is combined into Equation 2.14 to determine the inertial under-relaxation factor for the new time step for each mode,

$$\Gamma_m^n = \frac{1}{2}\left(\max\left[\gamma_m^{k,o}\right]S - 1\right)$$ (4.5)

where n is the new time step, o is the old time step, and S is a stability factor greater than one. A stability factor of 1.5 is used for the simulations in this report. The stability factor is necessary in the case where the modal added mass is increasing per time step. This ensures that the inertial under-relaxation factor for the new time step is in the stability range of the FSI solver.

The estimation of the modal added mass in Equation 4.4 is invalid if the modal acceleration for a given mode is zero. The adaptive inertial under-relaxation scheme insures that the modal added mass estimation does not divide by zero. If accelerations are small, large values of the estimated added mass will plague the algorithm so small acceleration estimations need to be eliminated for any mode. To determine what small accelerations are, the modal accelerations for all modes are normalized by the absolute value of their sum,

$$\ddot{q}_{m,norm} = \frac{\ddot{q}_{m,est}^2}{\sum\limits_{m=1}^{\#modes} \ddot{q}_{m,est}^2}.$$ (4.6)

The normalized modal accelerations that are smaller than 0.1, or 10% of the summed squared modal accelerations, use the last time step estimate of added mass for that mode instead of the new calculated value. A similar normalization can also be made for the modal forcing to remove high modal added mass estimations that may linger between time steps. Normalized modal forces that do not meet the minimum criteria can set the modal added mass estimate for that iteration and mode to zero. If a normalized modal force is used, the minimum criteria for the normalized modal force is recommend to be set to 0.01 (1%) or smaller.

To reduce large oscillations in the inertial under-relaxation factor between time steps, a reduction factor R is used to restrict the decrease in the inertial under-relaxation factor between time steps,

$$\Gamma_m^n = \max\left[\Gamma_m^n, R\Gamma_m^o\right], \quad R = [0:1].$$

(4.7)

A reduction factor of 0.9 is used in this study. This means that the inertial under-relaxation factor for the new time step can not be less than 90% of the factor from the old time step. This has the effect of stabilizing the algorithm when difficulties in calculating the estimated modal added mass are encountered leading to large and small estimations between time steps. For a constant iteration value, significant changes in the inertial under-relaxation factor between time steps can lead to instabilities in the adaptive inertial under-relaxation scheme.

When the modal added mass estimations are small enough that Equation 4.5 becomes small or negative. A minimum inertial under-relaxation factor is set before runtime that is greater than or equal to zero.

$$\Gamma_m^n = \max\left[\Gamma_m^n, \Gamma_{m,min}\right], \quad \Gamma_{m,min} \geq 0.$$

(4.8)

This minimum value can vary between modes and insures that the inertial under-

relaxation value is not negative.

This work uses a constant iteration for each time step. In future work, a convergence criteria for the state vector should be added so that the number of iterations can adapt to assure convergence before moving to the next time step. The sensitivity of the stability factor, reduction factor, and other terms in the adaptive inertial under-relaxation scheme could then be further analyzed for convergence. Recommendations for the value of the factors in the adaptive inertial under-relaxation scheme could be provided.

4.4   Modal Added Mass Analysis

The adaptive inertial under-relaxation scheme is used to estimate the added mass at the previous time step and determine a suitable inertial under-relaxation factor for the next time step. The adaptive scheme uses a constant 10 iterations per time step and a 0.5 minimum inertial under-relaxation factor. Nine modes are used, but the first mode contains the majority of the structural energy and requires the largest inertial under-relaxation factor. The analysis will show the first two modes for analyzing the stability of the adaptive algorithm. A constant drop velocity with the approximate FSI boundary condition, from Section 3.2.1, is used and results for the deflection and strain for adaptive and fixed inertial under-relaxation factors are shown in Figures 4.1 and 4.2.

The adaptive algorithm shows good agreement with the 1.7 fixed inertial under-relaxation factor. The adaptive algorithm remains stable with the 0.5 minimum inertial under-relaxation factor, while the fixed 0.5 inertial under-relaxation factor goes unstable during impact. This shows the advantage of the adaptive inertial under-relaxation scheme for cases where the modal added mass estimation is difficult or not possible for all modes. An analysis of the convergence of the adaptive scheme is presented in Figure 4.3.
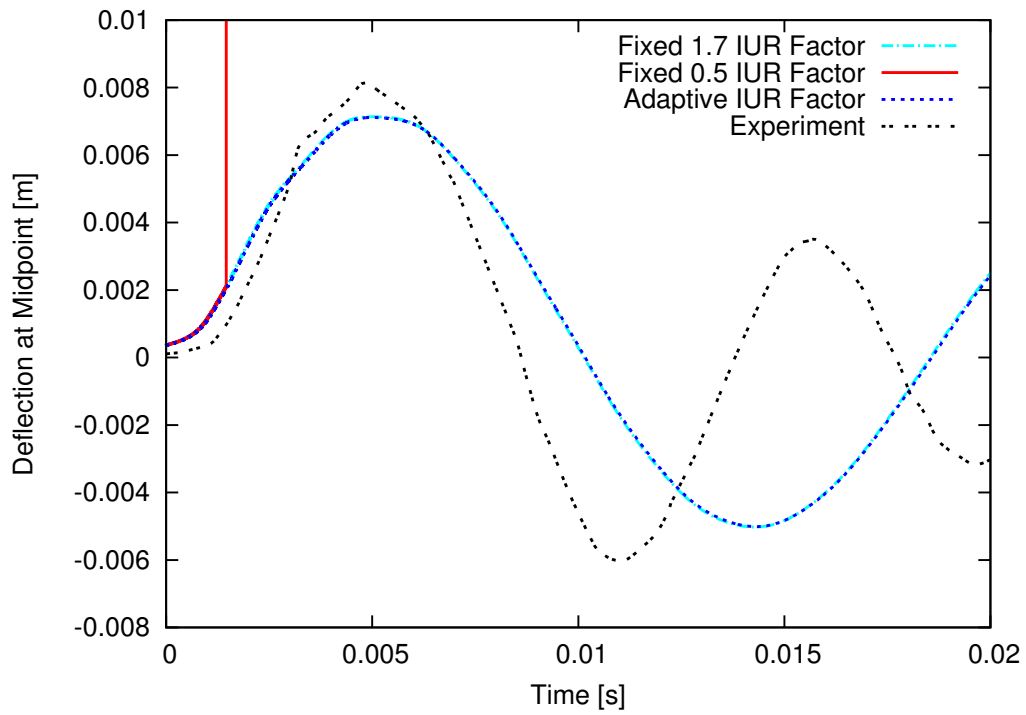
Figure 4.1: Deflection for runtime adaptive added mass simulation
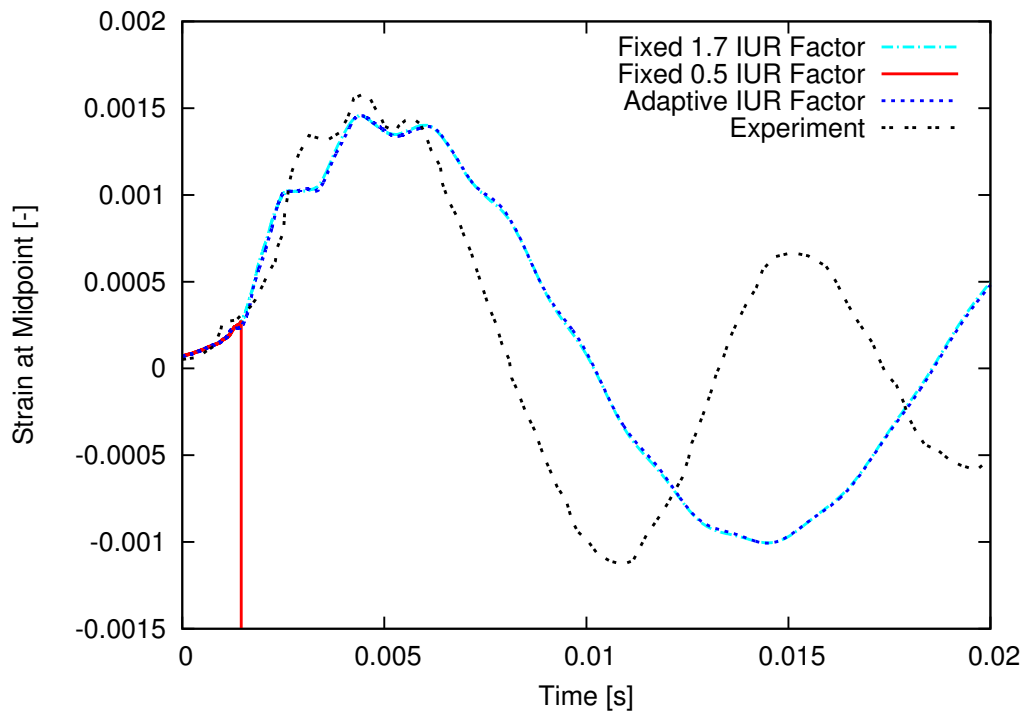
Figure 4.2: Strain for runtime adaptive added mass simulation
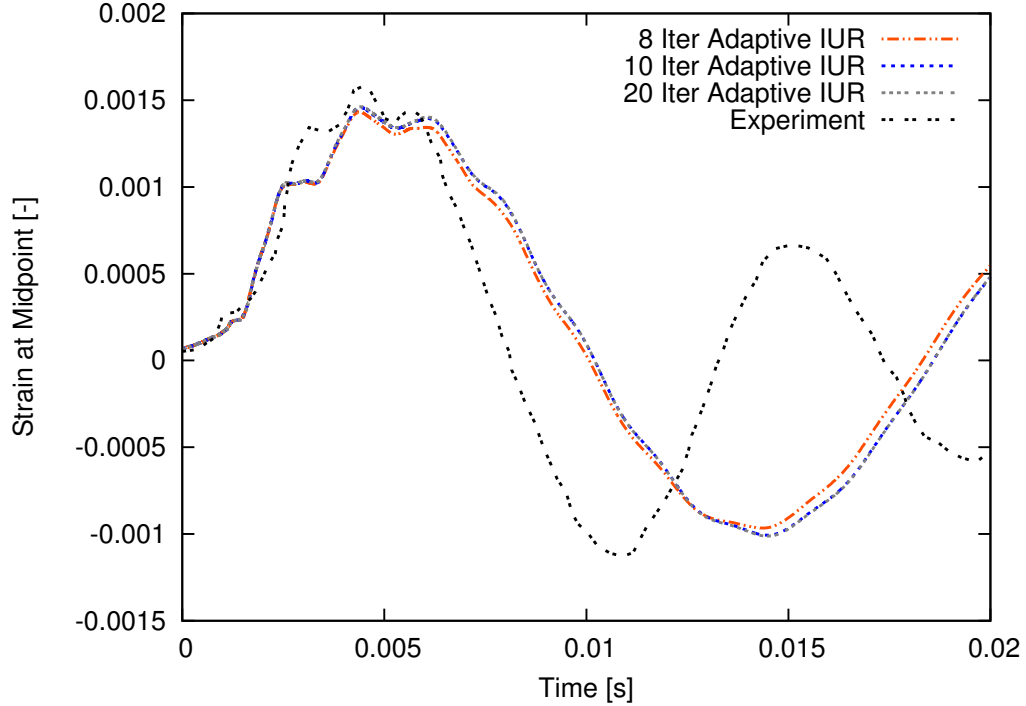
Figure 4.3: Strain convergence study for runtime adaptive added mass simulation

For the fixed 1.7 inertial under-relaxation factor a minimum of 6 iterations were needed for the convergence of strain, Section 3.1.3. The adaptive inertial under-relaxation scheme needs at least 10 iterations for the convergence of strain. The increase in iterations comes from the over estimation of the new inertial under-relaxation factor when there are small modal structure accelerations. Small modal accelerations cause overpredictions of the estimated modal added mass. Overpredictions can also come from the modal force assumption, where the forcing from added mass effects is assumed to dominate the modal forcing. The algorithm does show promise for simulations where calculating an estimate of the added mass before runtime is difficult. An increase in the iterations is a better alternative to the simulation failing due to stability issues. The computational cost from increasing the number of iterations can be much smaller than the computational cost from multiple failed simulations. The added mass estimation for mode one and two is plotted in Figure 4.4 for the adaptive algorithm and the fixed 1.7 inertial under-relaxation factor.
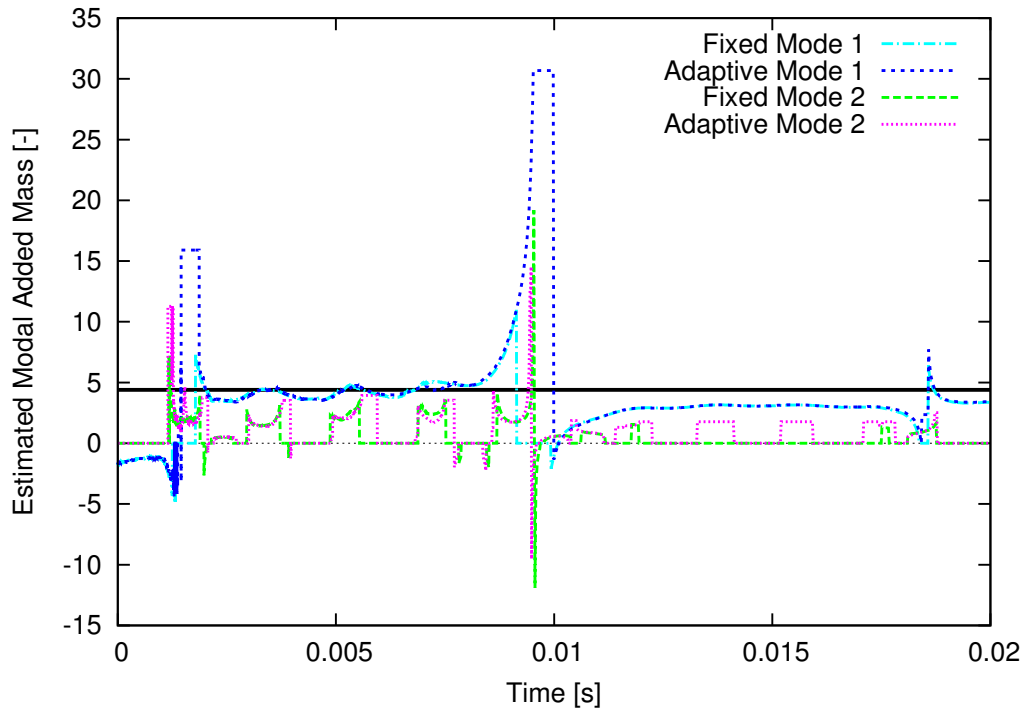
Figure 4.4: Modal added mass during runtime
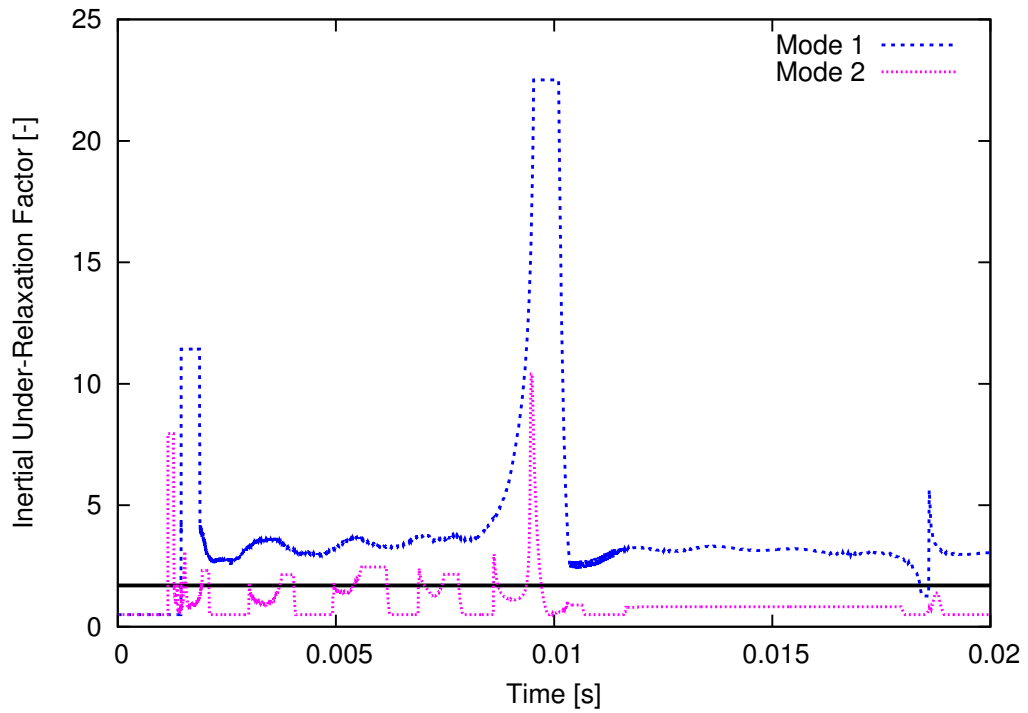
Figure 4.5: Inertial under-relaxation factor during runtime

The solid black horizontal line is the constant inertial under-relaxation equivalent value of 1.7 which corresponds to a 4.4 modal added mass by solving Equation 2.14 for γ_m. The estimation of the modal added mass for the adaptive conditions has several instances where the estimation is larger than the required stability criteria. This over estimation may come from the assumption made in Equation 4.2, where the added mass is assumed to dominate the modal forcing or from small modal accelerations. The adaptive estimate follows the trends of the fixed value, but has more noise present in the estimation. Small accelerations lead to large added mass estimates which increase the inertial under-relaxation factor, Figure 4.5. Larger overpredictions of the inertial under-relaxation factors require more iterations for convergence. The larger overestimate of the inertial under-relaxation factors cause the iterations needed for convergence to change from 6 to 10 iterations. The flat portions of the adaptive scheme which correspond to a maximum value are were accelerations are small enough that the modal added mass estimation from the previous time step is used. The flat portions of the adaptive scheme that correspond to zero for the estimated modal added mass are where the normalized force is small so the estimation of the modal added mass is set to zero. The flat portions of the inertial under-relaxation factor that match the 0.5 minimum inertial under-relaxation factor are were the estimation of the inertial under relaxation-factor is below the minimum value. An example of small acceleration that lead to larger modal added mass estimates is shown for the eight iterations over two time steps in Figures 4.6 and 4.7.

The vertical black line denotes the change between time steps and a new set of iterations. At the first iteration the fluid solution is solved first with the old structure state and the new structure state is solved with the new fluid update. The second iteration is when the fluid solution first sees the updated structure state solution and this is one of the places where issues with small accelerations can occur. In Figure 4.6, the absolute values of the modal accelerations are plotted on log scale. Iteration nine,
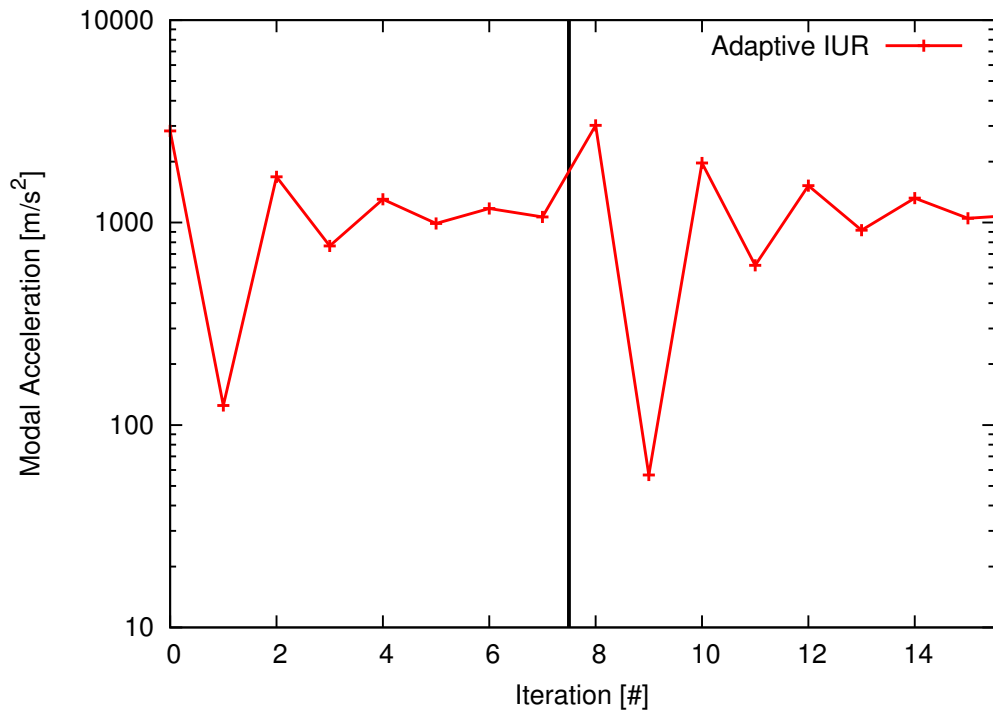
Figure 4.6: Structure modal accelerations during iterations
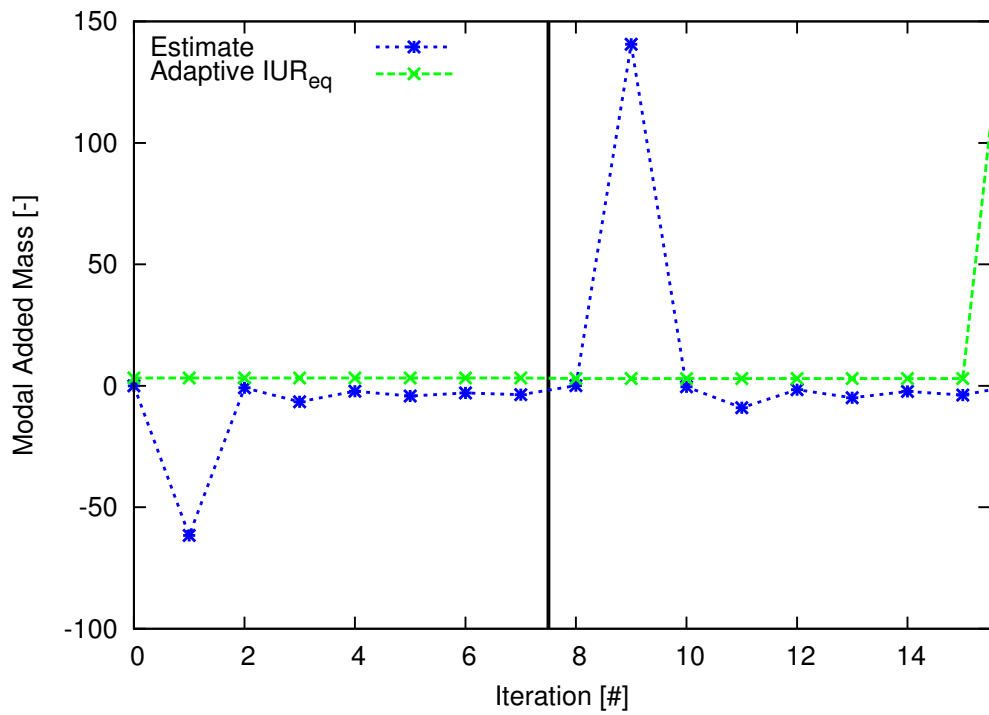
Figure 4.7: Structure modal added mass estimates during iterations

which corresponds to the second iteration in the new time step, decreases significantly from the converged modal accelerations after the fluid is solved with the first structure state update. This leads to a large estimation in the modal added mass for the current iteration as shown in Figure 4.7. This is the artificial added mass issues discussed in Young et al. (2012). After iteration 15, which is the last iteration in the new time step, the new inertial under-relaxation factor increases for the next time step. Stability issues were found if only the converged estimate of modal added mass is used. This means that the converged modal added mass estimation in the adaptive inertial under-relaxation algorithm does not always correspond to the stability criteria needed for the inertial under-relaxation factor.

The adaptive algorithm shows promise for simulations where added mass estimation before runtime is difficult or computationally expensive. Future work should explore issues such as the modal forcing assumption and how solving for the fluid solution first can cause stability issues with the adaptive inertial under-relaxation algorithm. Issues with handling small accelerations and convergence criteria are other areas of future exploration. Over estimating the modal added mass leads to better stability, but slower convergence. However, the adaptive inertial under-relaxation scheme is a better alternative to a failed solution due to stability issues with the inertial under-relaxation factor.

CHAPTER V

Wetdeck Slamming of a Catamaran

The primary goal of this research is to further understand the physics involved in wetdeck slamming events in order to provide analytical theories that model slamming with appropriate assumptions. This research provides the first look at a detailed hydroelastic analysis of a realistic catamaran geometry with a flat wetdeck. The high-fidelity FSI solver allows for the modeling of global and local loading on the catamaran and wetdeck to be explored. The influence of modeling different parts of the structure is discussed. Recommendations are provided for the important physics to model when using a simplified theory to predict response.

The FSI solver is applied to a realistic multihull geometry with a flat wetdeck. A segmented model is chosen to model global loads in addition to the local loads on the wetdeck structure. The geometry chosen is a test model for a Surface Effect Ship (SES) operating without the skirt which models a typical catamaran geometry with a flat wetdeck. Stationary simulations with head seas is simulated for Response Amplitude Operators (RAO) comparisons. Head seas with forward speed is simulated for measuring loads during wetdeck slamming events. The body plan of the SES is shown in Figure 5.1 and the backspline structure layout for the segmented SES model is shown in Figure 5.2.

The body plan for the SES shows a typical geometry for catamarans with flat
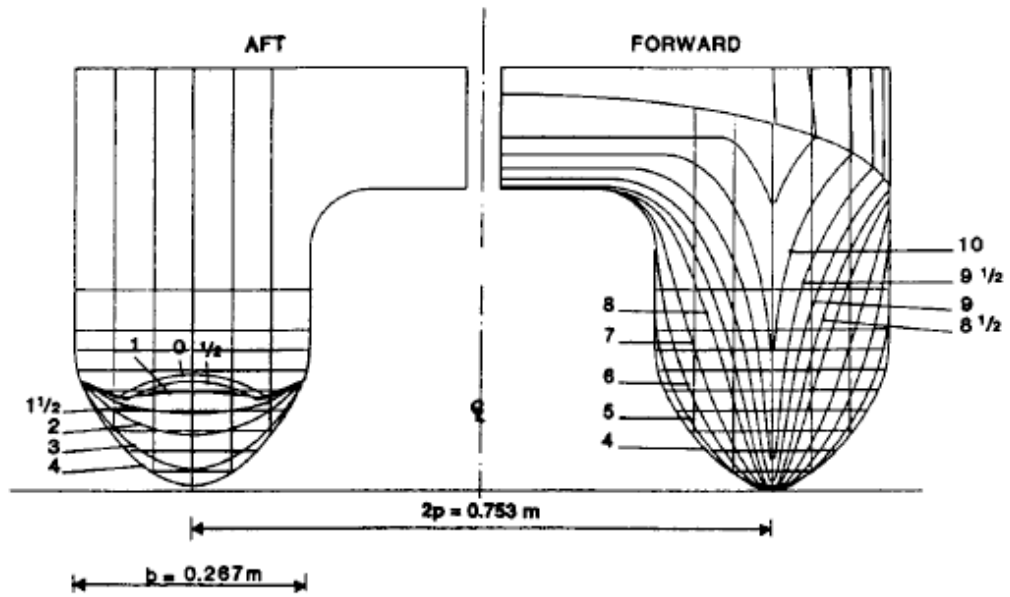
Figure 5.1: Body plan of the SES model without the skirt from Ge (2002)
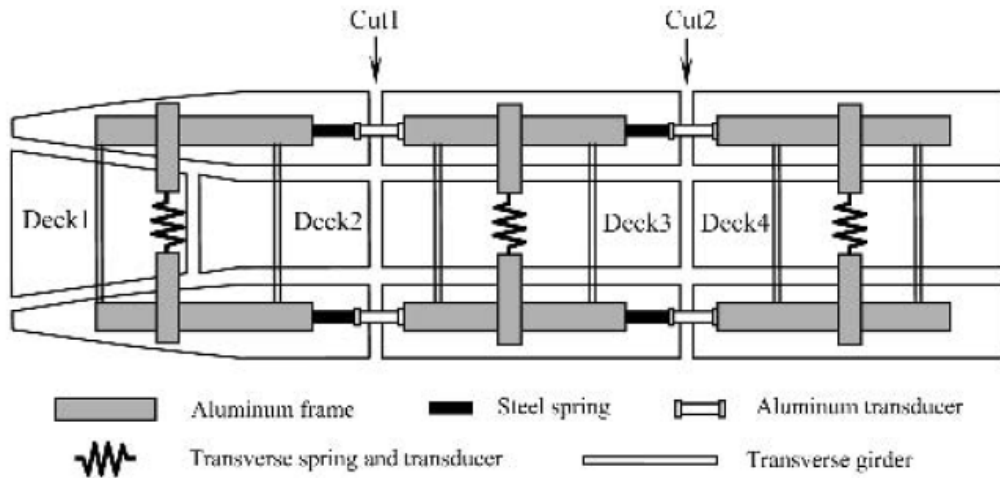
Figure 5.2: Global backspline structure layout for the segmented SES model from Ge (2002)

wetdecks. The backspline models the scaled structure elasticity of a typical full scale vessel. The model is cut into three segments longitudinally. There is another cut down the center line which separates the two hulls transversely. The wetdeck is cut into four separate plates and a pinned connection is used to connect the wetdeck plate to the backspline. Deck one and two connect to the two forward backspline segments, while decks three and four connect to the middle and aft backspline segments respectively. Deck one has constant slope relative to the baseline while the remaining decks are parallel to the baseline. The backspline structure connects all hull segments and wetdeck segments together.
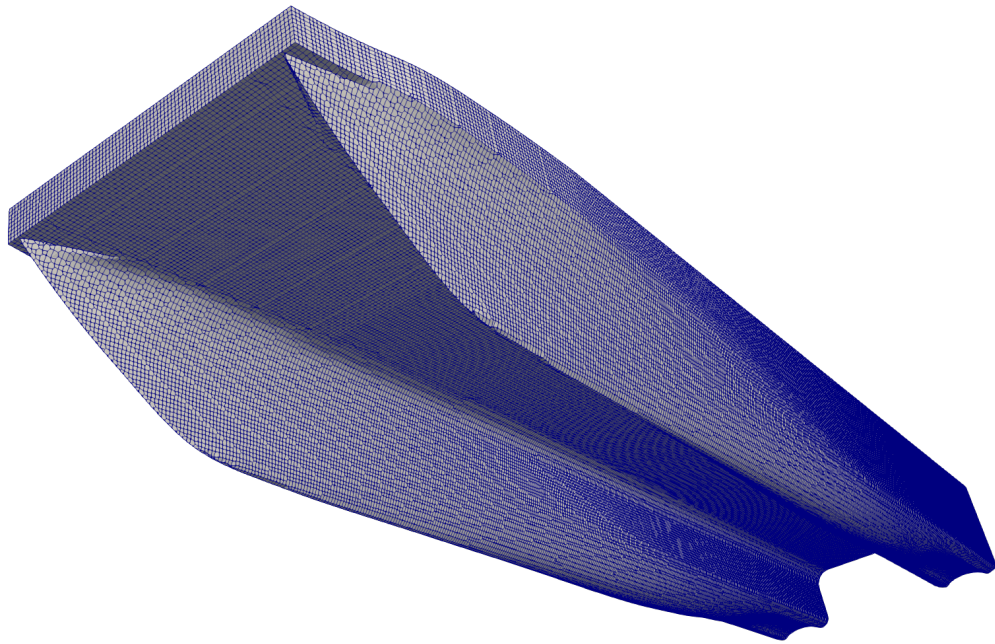
Figure 5.3: Fluid CFD grid patch of SES hull

The longitudinal elastic response is modeled by the steel springs and aluminum transducers located at cut one and two as indicated in Figure 5.2. Longitudinally, the segments are connected by the springs and transducers only. This allows for measurements of sectional forces and moments at cuts one and two. The transverse elastic response has contributions from the the wetdeck segments and the the springs and transducers connecting the segments transversely. Transverse bending will not

be analyzed for the head seas comparisons, as the structural loading is symmetric and transverse bending response is small compared with the longitudinal bending. There are two different mass distributions used in this chapter. Økland (2002) reported a total mass of 302 kg for the stationary tests and Ge (2002) reported a total mass of 246 kg for the slamming tests with forward speed. The RAO simulations use the 302 kg mass distribution and the elastic slamming simulations with forward speed use the 246 kg mass distribution. Both mass distributions are listed in Appendix A. Ge (2002) reported that the ballast weights used in the stationary tests were removed for the forward speed cases in waves.

The three-dimensional geometry is developed from a table of offsets, measurements, and the lines plans. The CFD grid is generated using the three-dimensional geometry and the snappyHexMesh mesh generation utility in OpenFOAM. The fluid face patches for the SES geometry is shown in Figure 5.3. Convergence studies and validation of the geometry are detailed in the following sections.

5.1   Rigid Simulations

An analysis of the fluid grid is conducted by performing rigid-body simulations. This insures that the three-dimensional SES geometry is correctly modeled and the fluid grid has enough resolution to capture the wave interactions with the SES model. Stationary simulations with head seas are used to compare the RAO with experimental results. A grid convergence study is conducted in heads seas with forward speed to analyze the convergence of the motion and the forcing on the wetdeck panels. The largest slamming event from the text of Ge (2002) is used for all forward speed simulations.

5.1.1 RAO Analysis

The SES model under went experimental testing at MARINTEK in Norway. Testing for the RAO of the vessel was conducted in the wave tank with zero forward speed. Experimental tests were conducted for wave periods between 0.7-2.5 seconds. To reduce the steepness of the waves and minimize non-linearity, wave heights between 0.02 and 0.03 m are used. Table 5.1 shows the wave properties for the four simulations used to compare to experimental results.

T [sec]	H [m]	U [m/s]	λ [m]	k [rad/m]
0.7	0.03	0.0	0.776	8.09
0.85	0.03	0.0	1.136	5.53
1.0	0.03	0.0	1.567	4.01
1.8	0.03	0.0	5.060	1.24

Table 5.1: Wave properties for RAO simulations

For the RAO simulations, the limiting factor for the grid resolution is the wave height. When simulating waves in the OpenFOAM CFD environment, 100 points per wave length and 5 points per wave height are preferred for resolving the wave profile. For this reason the largest wave height of 0.03 m is used. A resolution of 0.005 m gives 6 points per wave height and is used for all RAO simulation. The model is approximately 4.1 m long, 1.04 m wide, and 0.5 m tall. The grid extends from the hull two ship lengths in front, three ship lengths behind, 1.5 ship lengths to the side, 1.5 ship lengths below, and 0.75 ship lengths above. Stretching is used away from the hull to reduce the number of cells. The grid size is 13,845,714 cells and is split on 288 processors. A minimum time step size of 1000 time steps per wave period is enforced to minimize time discretization error. A list of the grid properties for the four simulations is shown in Table 5.2.

Økland (2002) presents the experimentally measured RAO for the SES in head seas with no forward speed. A Fourier analysis of the motion time history of the vessel is used to calculate the RAO transfer function. The magnitude of the first

T [sec]	p.p.w.l.	p.p.w.h.	Δt_{min} [sec]
0.7	155	6	0.0007
0.85	227	6	0.00085
1.0	313	6	0.001
1.8	1012	6	0.0018

Table 5.2: Grid properties for RAO simulations

harmonic from the transfer function is the RAO value. This value is a linearization of the vessel response at a certain wave frequency and amplitude. The heave RAO value is defined as,

$$\text{RAO}_{heave} = \frac{\eta_3}{\zeta_a} \tag{5.1}$$

where ζ_a is the wave amplitude and η_3 is the heave amplitude. The pitch RAO value is defined as,

$$\text{RAO}_{pitch} = \frac{\eta_5}{\zeta_a k} \tag{5.2}$$

where k is the wave number and η_5 is the pitch amplitude. The experimental values are measured from the optical sensor and Motion Reference Unit (MRU) and shown in Figures 5.4 and 5.5 with the simulation values. Stationary tests were also conducted for oblique, beam, and following seas. The most severe slams occurred in head seas, so only head seas are analyzed.

Økland (2002) expressed low confidence in the experimental measurements for heave at the lower frequencies due to the differences in the RAO between the optical sensor and MRU and the small wave amplitudes used in the measurements, which were 30 mm tall. The small wave amplitudes used in the RAO measurements also drove the CFD grid size, as at least five points is needed per wave height to capture the wave profile. The heave RAO shows reasonable agreement with the experimental results and only have large discrepancies for the second lowest frequency. The slamming
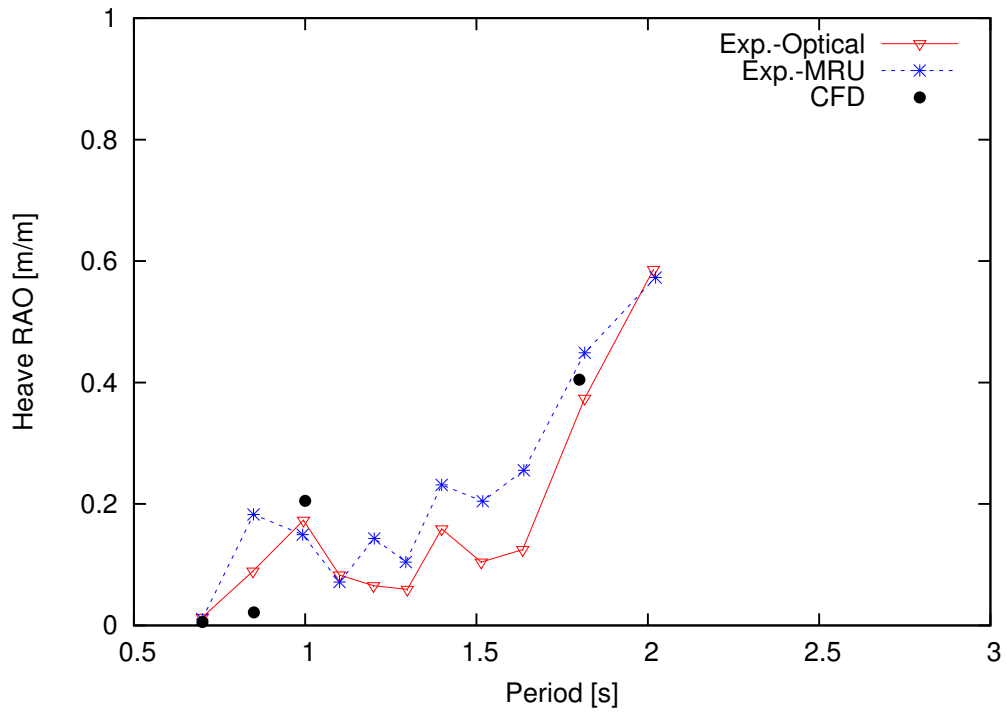
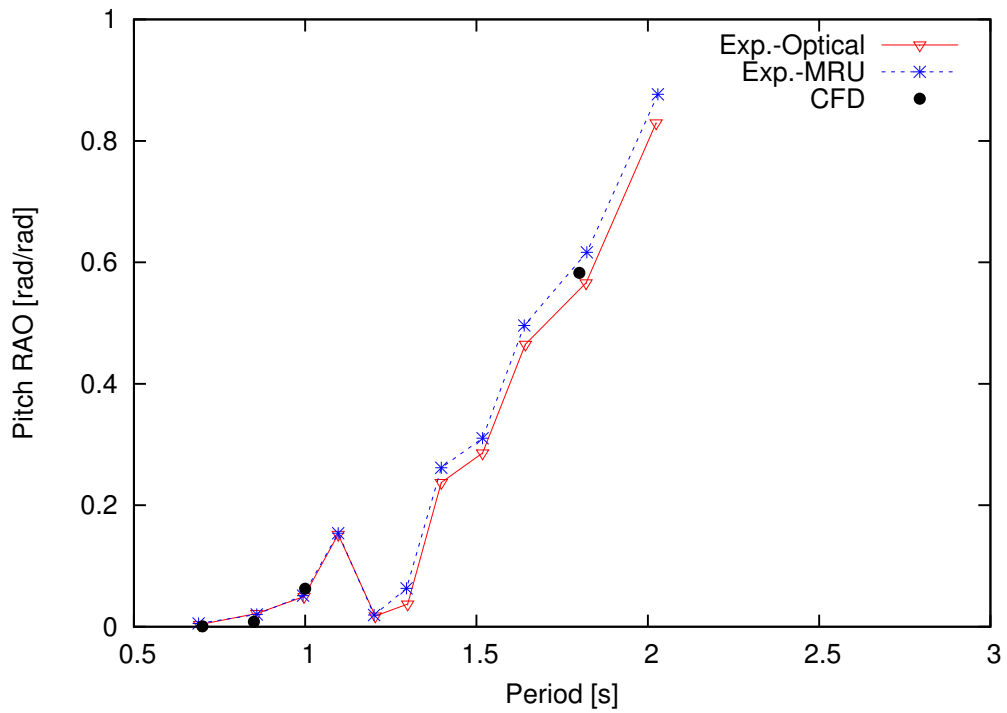Figure 5.4: Heave RAO for head seas with zero forward speed

Figure 5.5: Pitch RAO for head seas with zero forward speed

event that is chosen for validation has a wave period of 1.8 seconds. For this wave period, the rigid CFD model falls between the two experimental measurements from the MRU and optical sensor for the heave and pitch RAO. The pitch RAO also shows excellent agreement with the experimental measurements at lower frequencies. Capturing the pitch motion is important for local wetdeck slamming loads as large vertical velocities can be achieved at the bow or stern due to pitching motion. The agreement with the experimental RAO measurements gives confidence to the CFD grid modeling of the SES geometry.

5.1.2 Wetdeck Slamming and Forcing

Slam events are encountered in the experiments for a wave period of 1.8 seconds, a forward speed of 1.8 m/s, and wave a amplitude of 0.041 m. These conditions are used in the simulations and new grids are generated based off the RAO studies. The coarse grid has 2,384,130 cells and the hull face patch is shown in Figure 5.3. The medium grid has 3,533,572 cells and the fine grid has 8,562,860 cells. Figures 5.6 and 5.7 show the rigid heave and pitch motions during a slamming period for each grid. The slamming period is the wave encounter period of 1.097 seconds. The impact of the wetdeck starts at approximately 3.7 seconds in the following figures.

The pitch response between the two grids closely matches in frequency and amplitude. However, the heave motion has a small time delay for the coarser grids compared to the fine grid. This small difference may be attributed to the difference in resolution of the wave, since fewer cells are used to describe the height of the wave for the coarser grids. Modeling the elastic structure depends on the forcing from the fluid grid. Figure 5.8 shows the total vertical force on the hull and Figure 5.9 shows the total vertical force on the Deck 1 fluid patch for the coarse, medium, and fine grids. The time window for the experimental results, presented in Ge (2002), is from 19.5 to 23.5 seconds. The time window corresponds to a series of consistent slam
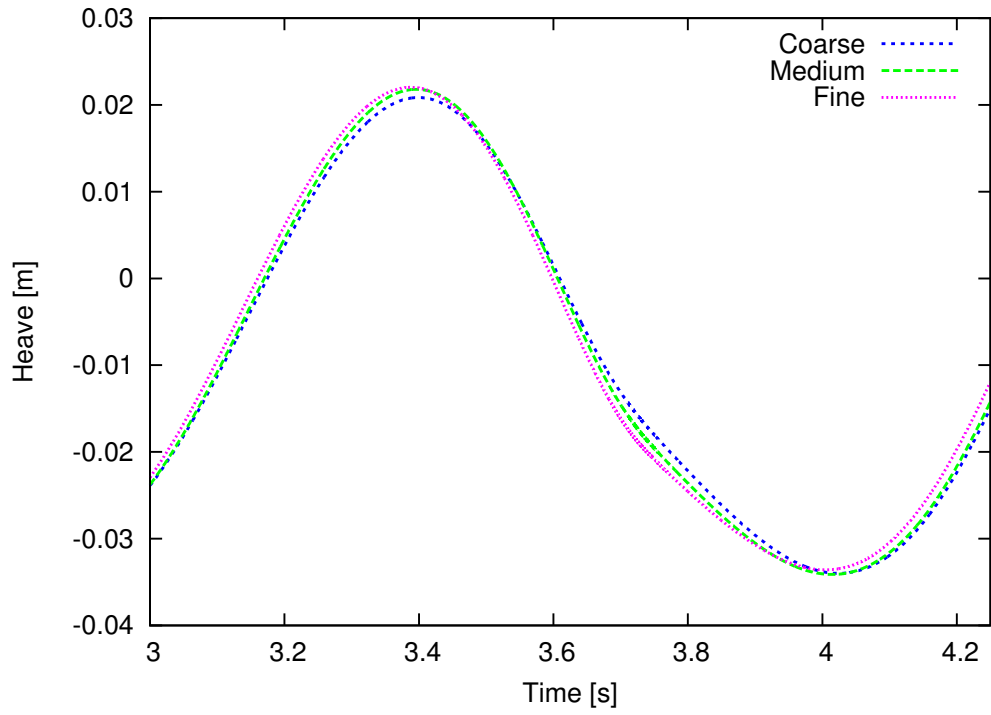
Figure 5.6: Heave response during slamming for grid refinement study
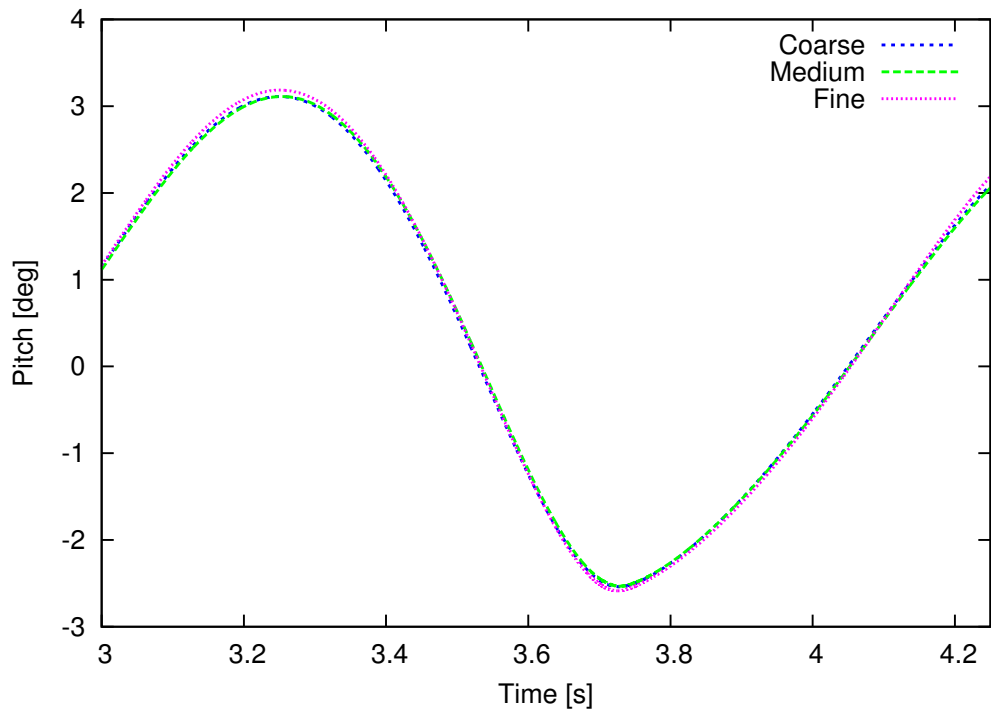
Figure 5.7: Pitch response during slamming for grid refinement study

events, and is shifted to match the simulation results.
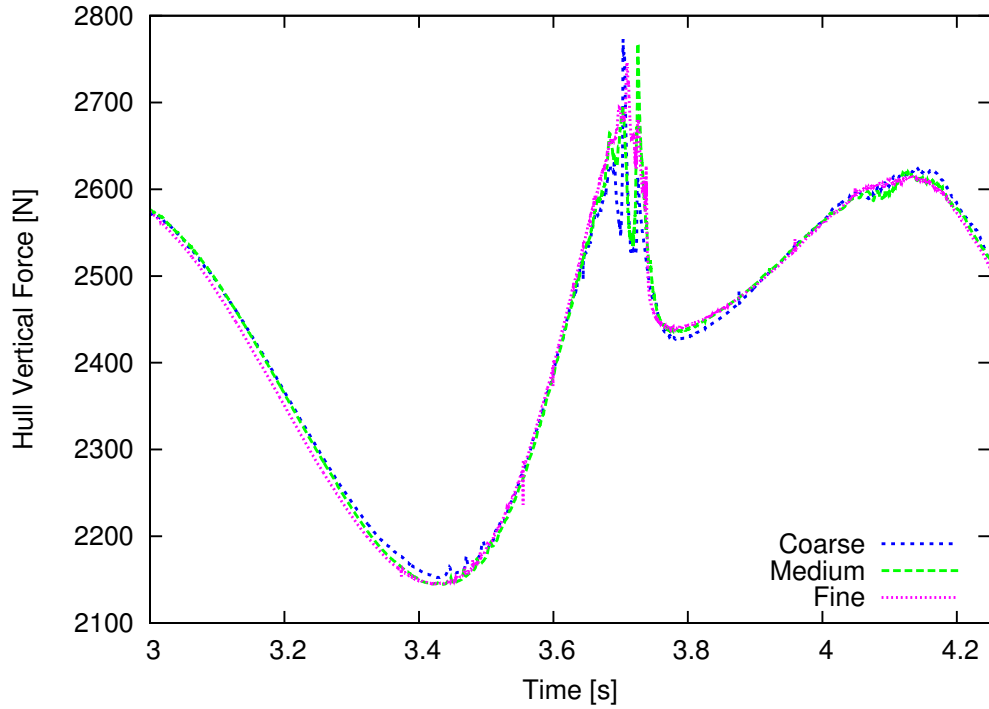
Figure 5.8: Total rigid vertical hull forces for grid refinement study

The forcing on Deck 1 from the experiments is measured at the pinned connections between the wetdeck and the global structure backspline. The oscillations in the experimental measured forces come from the inertial forces between the wetdeck and global structures. The forces measured by the rigid simulations are the pressure forces acting on the fluid patch and do not contain the elastic forcing oscillations. The peak slamming force is sensitive to the wave-hull interactions and the resolution of the grids. The peak force is overpredicted by the rigid grids as expected since there is no structure-to-fluid interactions. A larger negative force impulse loading on the patch after impact corresponding to the exit phase is seen in experiments and simulations. This negative force loading was also noted in the wedge entry and exit studies by Piro and Maki (2011). The structure response to larger force impulse loads which corresponds to the area under the forcing curve. The negative impulse load on the structure is significant, and will influence the structure response. Modeling the exit
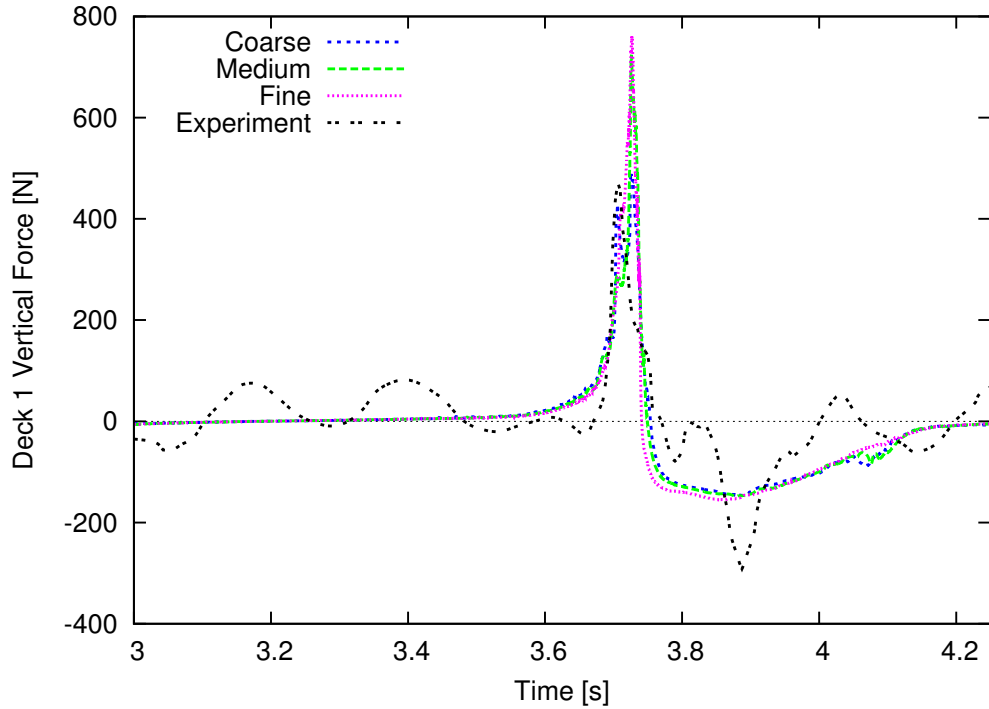
Figure 5.9: Rigid vertical forces on Deck 1 for grid refinement study

phase is just as important as modeling the entry. The FSI solver has the ability to solve the rigid body motions in all six degrees-of-freedom. The simulations for this study in head seas, fix the model at a constant forward speed and solve the pitch and heave motions while keeping all other degrees-of-freedom fixed. This allows for the entry and exit phase to be solved for the model. Korobkin et al. (2017) have worked with analytical exit stage models for three-dimensional bodies. Analytical models are complex and require separate modeling of entry and exit stages to accurately account for the forcing on the body.

The forcing between the coarse, medium, and fine grids show good agreement except during the impact. The coarse and medium grid have more noise in the forcing signal during impact for the total vertical forces on the hull and Deck 1. A small time delay in the coarse and medium grid compared to the fine grid is exhibited in the forcing signals. Impact forcing show differences in maximum loads, but the impulse load on the structure is similar between the coarse, medium, and fine grids.

The maximum pressure during the simulation for each patch on Deck 1 is plotted for both the coarse, medium, and fine grid in Figure 5.10 using the non-dimensional pressure coefficient,

$$C_p = \frac{p_{max} - p_a}{\frac{1}{2}\rho V_{ave}^2},\tag{5.3}$$

where p_{max} is the maximum pressure during the simulation on the face patch, p_a is the atmospheric pressure, ρ is the density of water, and V_{ave} is the average impact velocity. The average impact velocity is approximately 1.9 m/s and includes the forward and vertical velocity components of the wetdeck during impact. Majority of the velocity comes from the forward speed of the vessel. Note that the three patches in Figure 5.10 are not a single time instance, but the maximum recorded pressure on each cell face at any point in time during the simulation.

Figure 5.10: Maximum rigid slam pressures on the Deck 1 patch for the coarse (left), medium (middle), and fine (right) grids

The wave hull interactions during a wetdeck slamming event influence the peak

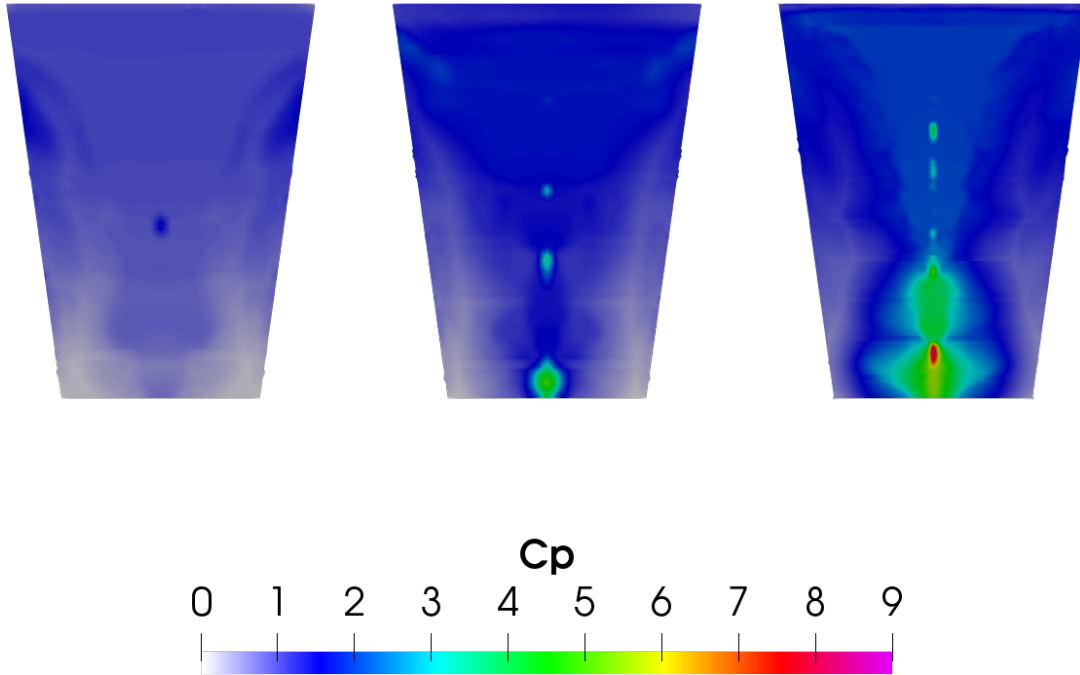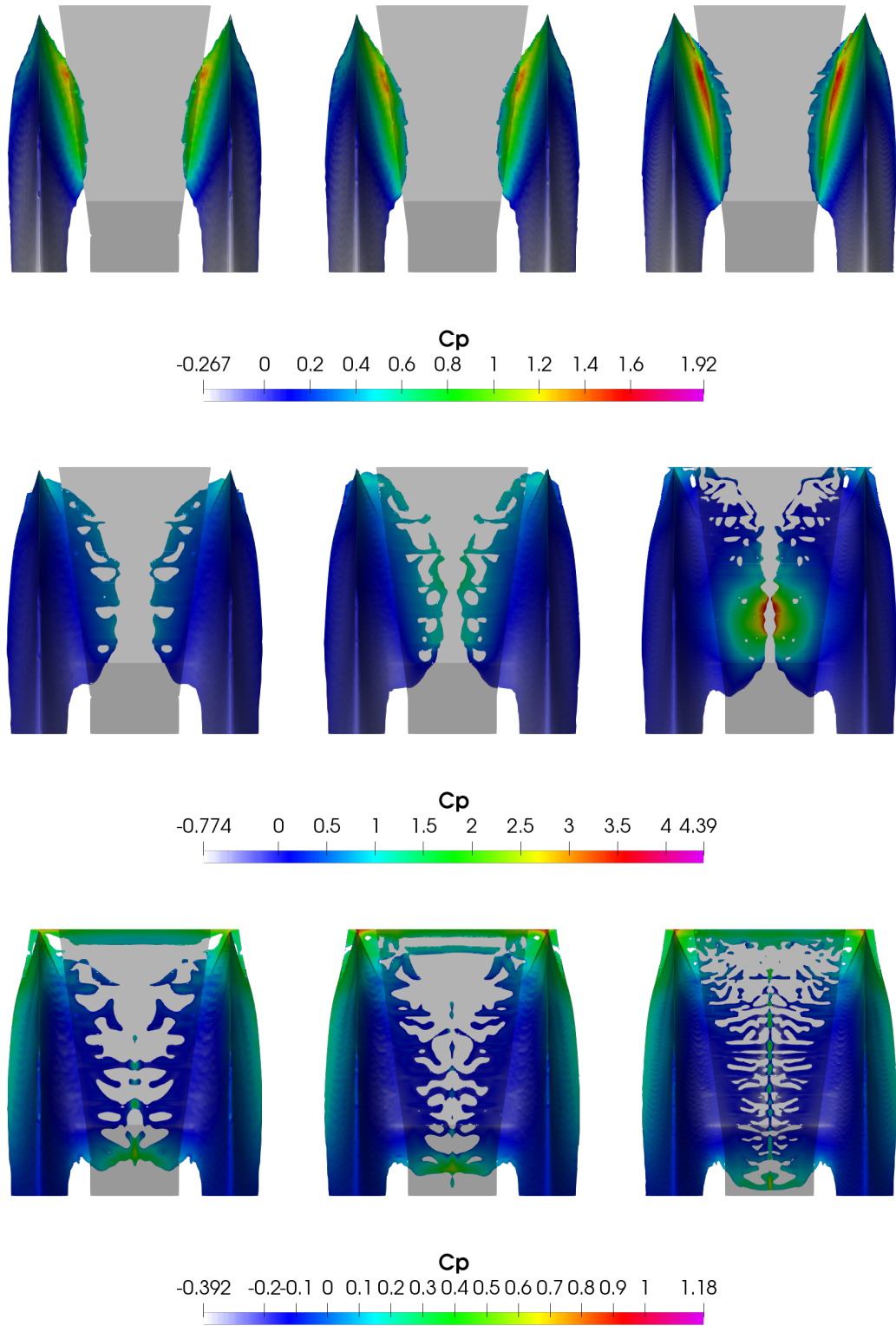Figure 5.11: Wetted rigid pressure for coarse (left), medium (middle), and fine (right) grids at times 3.69 s (top), 3.735 s (middle), and 3.78 s (bottom)

pressures along the Deck 1 patch. The peak pressures are sensitive to the wave profiles and modeling the correct wave-hull interactions. The largest peak pressures occur near the location that Deck 1 and 2 meet. The maximum pressure value increases with grid refinement similar to the flat plate impact simulations. A high resolution of grid cells is needed to accurately model maximum value of pressure. Even though the maximum pressure value is not captured with the coarse and medium grid, the forcing on the fluid patches is not sensitive to capturing the maximum value of pressure. Figure 5.11 shows the wetted rigid pressures at different stages of impact for the coarse, medium, and fine grids.

The wetted rigid pressures on Deck 1 and part of Deck 2 show that a jet root develops from the water pile-up as the bow sections enter the wave. As the two jet roots approach each other, the wetdeck impacts the wave crest and entraps air. The moment that the maximum pressure occurs is difficult to capture visually as data must be written out at the exact time step for post-processing. As the wetdeck continues to impact the wave crest, the entrapped air is mixed. The maximum pressure occurs close to initial impact and around the same time the two jet roots meet. Although the maximum pressure is not captured by the coarser grids, the elastic structure responds to the force impulse loading. It is important to capture the longer impulse loading accurately for the structural response. Both the coarse, medium, and fine grids exhibit similar long term force impulse loads, shown in Figures 5.8 and 5.9, on the fluid patches and are sufficient for modeling the structure response.

5.1.3 Sectional Forces

Sectional forces at the segmented cuts are measured in the experimental tests. Experimental measurements are taken from a five degree-of-freedom aluminum force transducer, see Figure 5.2, that makes up part of the elastic beam connection between segments. The mass and inertia information for each segmented is provided by Ge

(2002), and can be referenced in Appendix A. Using the mass data and integrating the pressure force over the hull fluid patch, the rigid vertical shear force and vertical bending moment is calculated at each segmented and compared with experimental data, Figure 5.12.

(a) Vertical shear force at Cut 1

(b) Vertical bending moment at Cut 1

(c) Vertical shear force at Cut 2

(d) Vertical bending moment at Cut 2
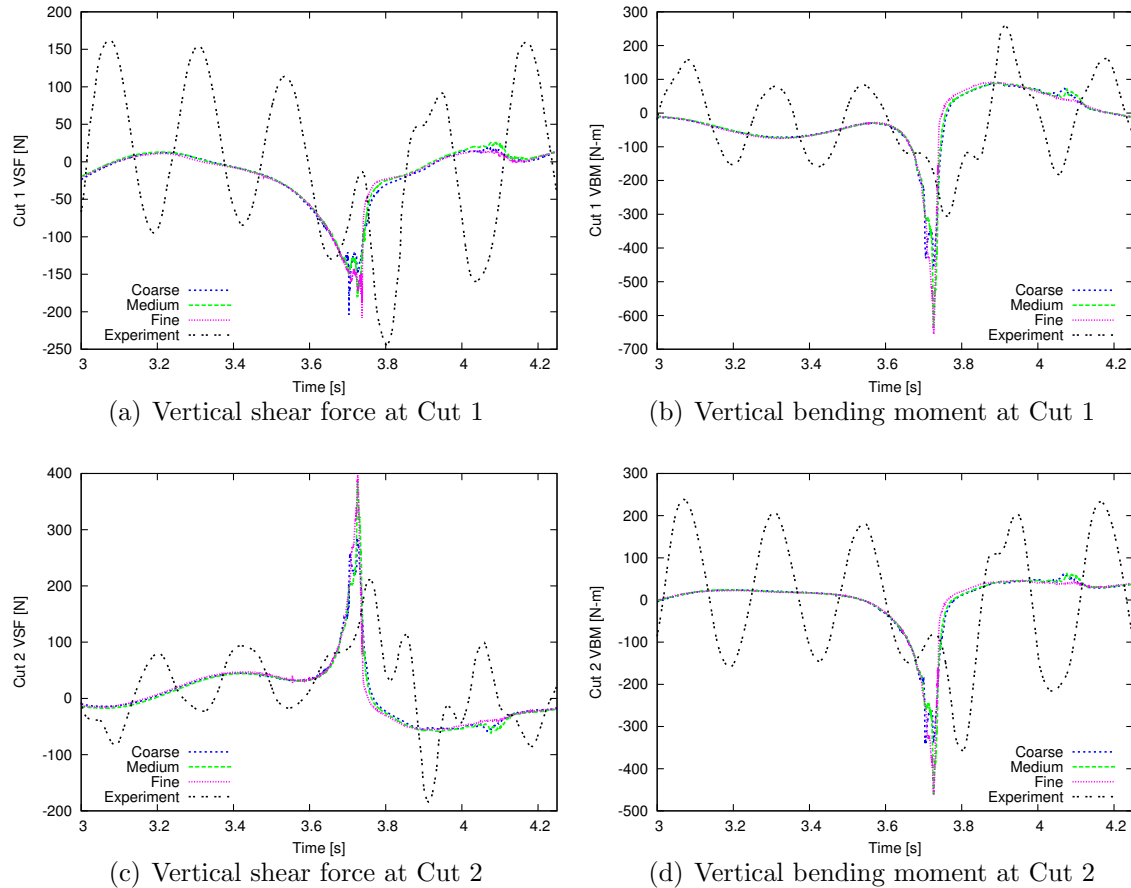
Figure 5.12: Rigid simulations of vertical shear force and bending moment at segment cuts

The sectional forces are the sum of the port and starboard longitudinal transducers at each cut. The sectional forces are zeroed at the static load case with zero forward speed. The rigid simulations do not contain the global structure ringing response that is seen in the experimental results. The rigid sectional forces do follow the average forcing that the experimental results are oscillating about. There is not a large variation in the shear force and bending moment between the coarse, medium,

82

and fine grids. Differences in the shear force and bending moment do occur at the initial impact of the wetdeck around 3.7 seconds. These differences are small and do not significantly affect the sectional forces after the impact. The structure responses to the force impulse load and the visual differences between the force impulse load between the three grids is small. This suggests that the coarse grid has enough resolution to solve the global structure response.

5.2 Elastic Simulations

The coarse grid is chosen for the elastic simulations based on the studies from the previous sections and due to the large computational cost savings when compared to the medium and fine grids. Elastic simulations are conducted using a one-way coupling between the rigid fluid grid and structural model and two-way tightly coupled hydroelastic simulations with the structure response influencing the fluid solution. The first 90 modes are used for the global simulations which include 24 modes from Deck 1 and 6 modes from Deck 2. The same number of modes for Deck 1 and Deck 2 are used in the local only simulations. The FEA of the structure is modeled in Abaqus and the modal decomposition information is provided to the FSI solver. Figures 5.13-5.15 show the local and global FEM generated in Abaqus and the mapping to the fluid grids of the first mode shapes.

To study local effects, the FEM models of Decks 1 and 2 are modeled separately and attached to a rigid global structure. Wetdeck slamming only occurs for this case on Decks 1 and 2, so the remaining decks are assumed rigid. A pinned connection to the rigid global structure is used for connecting the wetdecks to the hulls. The rigid body motions of the SES is transferred to the elastic wetdeck structures through the pinned connections. Pressure loads from Decks 1 and 2 are applied to the one-way coupled structures respectively.

Global loads are accounted for by modeling the entire SES structure. The global
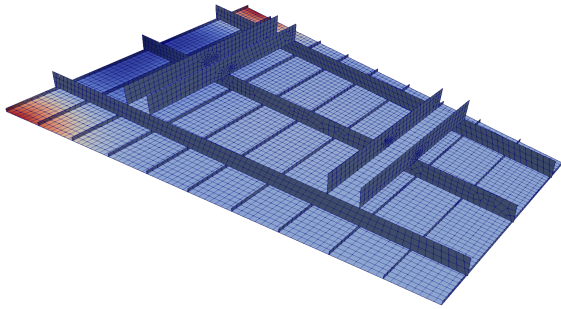
(a) Structure FEM grid
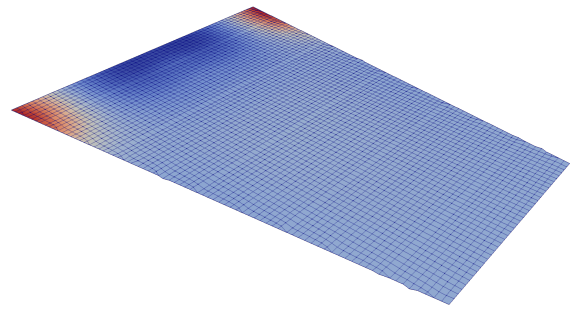
(b) Fluid CFD grid

Figure 5.13: Deck 1 structure to fluid mapping of the first mode shape
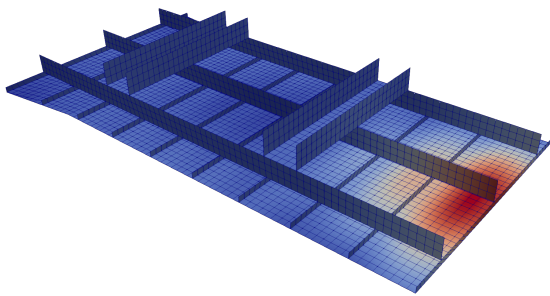
(a) Structure FEM grid
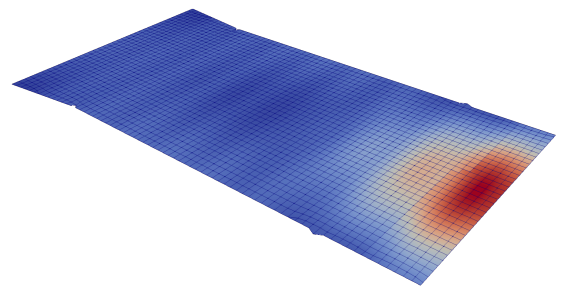
(b) Fluid CFD grid

Figure 5.14: Deck 2 structure to fluid mapping of the first mode shape
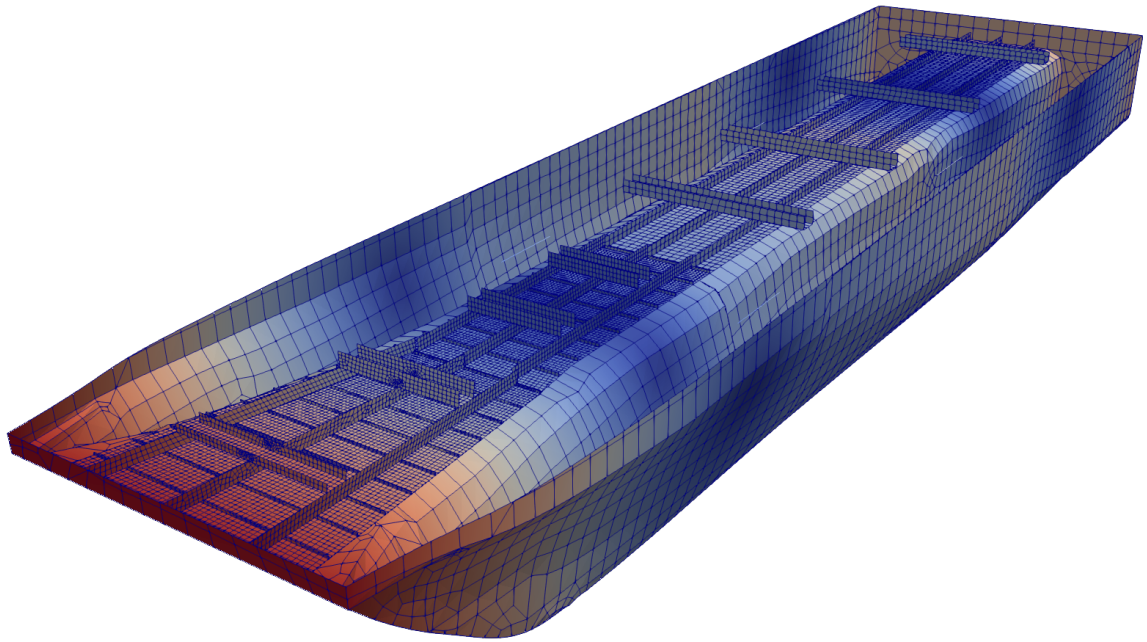
(a) Structure FEM grid
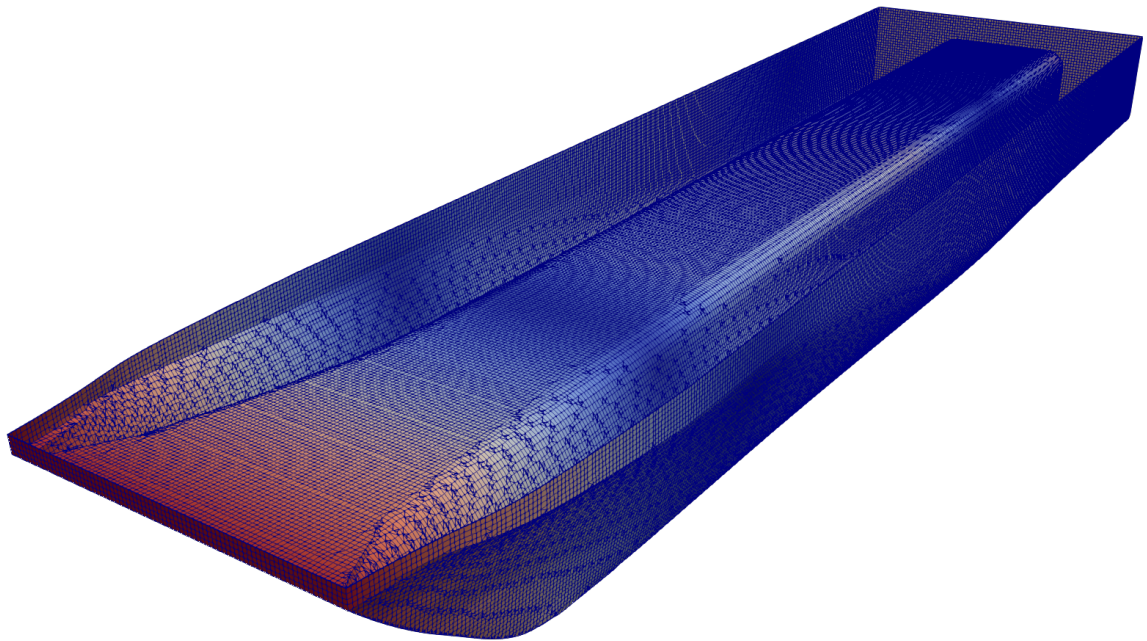
(b) Fluid CFD grid

Figure 5.15: Global and local structure to fluid mapping of the two node bending mode

structure connects all six segments using beam elements. The wetdecks connect to the segments through pinned connections. The entire fluid hull patch pressures are provided to the one-way and two-way coupled global structure. For the two-way simulations the entire fluid hull patch models the hydroelastic effects using the approximate FSI boundary condition. The layout of the beam elements connecting to the center-of-gravity of each segment is shown in Figure 5.16 where the bow is at the top and the stern is at the bottom of the page.

Each beam element, displayed in green, has pinned boundary conditions at the ends that connect to the red Cartesian coordinates that mark the center-of-gravity location of a segment. The rigid connections between the pinned beam and the center-of-gravity are the red line segments. The mass and inertia information for each segment that is not included in the modeled structure, such as motors, measurement equipment, etc., is included as a rigid body point mass at the center-of-gravity of each segment. The elastic spring and transducer that connect the segments are modeled as beam elements with an equivalent $EI_{eq} = 6,541\ Nm^2$ and equivalent length of 0.21 m as provided by Ge (2002). The global FEM also models the four wetdecks since they provide a significant contribution to the transverse bending stiffness. Rigid connections are also used between the rigid body point masses and the pinned boundary condition of each wetdeck. Decks 1 and 2 connect to the forward two segments and Decks 3 and 4 connect to the middle and aft segments respectively, see Figure 5.2. Rigid shell elements are used to model the hull geometry. The rigid shell elements for each segment are connected to the rigid body point mass and transfer the pressure forces and moments from the hull to the internal structure. The rigid shell elements are known as transfer shell elements in the FSI solver. The transfer shell elements map the fluid forcing to the structure for the one-way and two-way simulations. For the two-way simulations, the transfer shell elements provide the structure response to the fluid using the approximate FSI boundary condition. Table 5.3 shows the dry

86
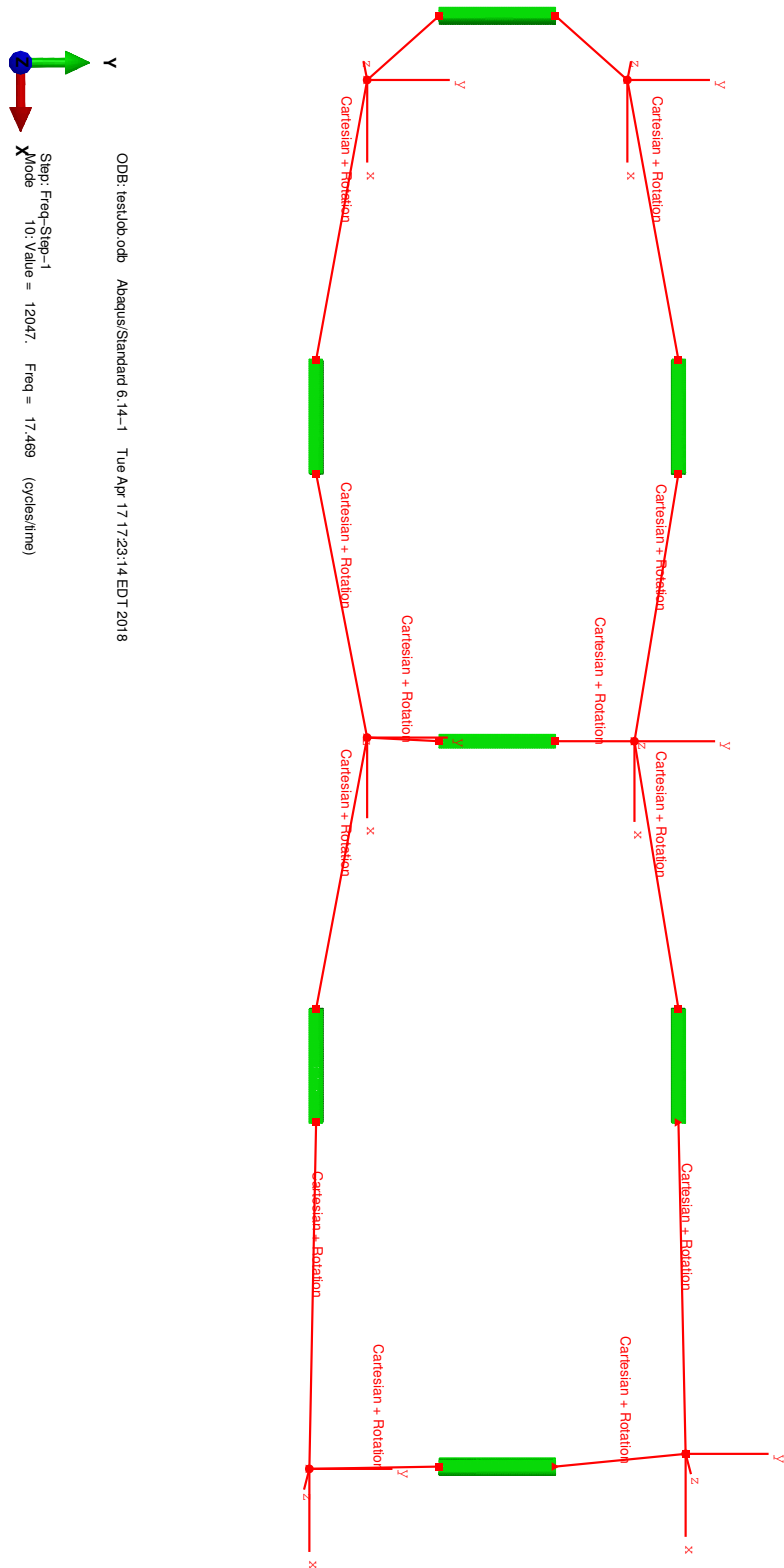
Figure 5.16: Global structure model using beam elements

oscillation period for the two node and three node bending. The dry frequencies were measured experimentally and reported by Økland (2002). The two mass distributions are modeled numerically using the FEM with Ge (2002) 246 kg and Økland (2002) 302 kg mass distributions.

Mode Type	Økland Exp. [sec]	FEM 246kg [sec]	Diff. [%]	FEM 302kg [sec]	Diff. [%]
2 Node Bending	0.17	0.14	-20.1	0.15	-9.4
3 Node Bending	0.07	0.06	-17.9	0.06	-12.4

Table 5.3: Dry oscillation period comparisons with experiments for the SES model

The two node bending mode is the first mode shape, and is shown in the mapping example in Figure 5.15 for Ge (2002) 246 kg mass distribution. The experimental measurement data is reported for Økland (2002) 302 kg mass distribution. The difference in oscillation period between the experiments and FEM for Økland (2002) 302 kg mass distribution can be due to the accuracy of the effect stiffness, effective length, mass distribution, structural elements, and the precision of the measured values. The oscillation periods of the FEM are modeled in a vacuum while the experimental results were measured in air. Although added mass effects in air are small, the oscillation periods would decrease if the experimental measurements were conducted in a vacuum. The difference between the FEM oscillation periods of Økland (2002) and Ge (2002) is from the differences in the mass of each model.

The complex fluid interactions with the catamaran geometry, rigid body motion solver, and the elastic structure increase the number of iterations needed for convergence. A convergences study on the number of iterations is conducted for the elastic two-way coupling simulations. The convergence simulations start at rest with the fluid grid at the starting draft and the structure at zero displacement. The structure begins to oscillate from the sectional forces and moments acting on the catamaran. The convergence of the heave and pitch motions are shown in Figures 5.17 and 5.18.

The rigid body motion solver uses a similar inertial under-relaxation technique
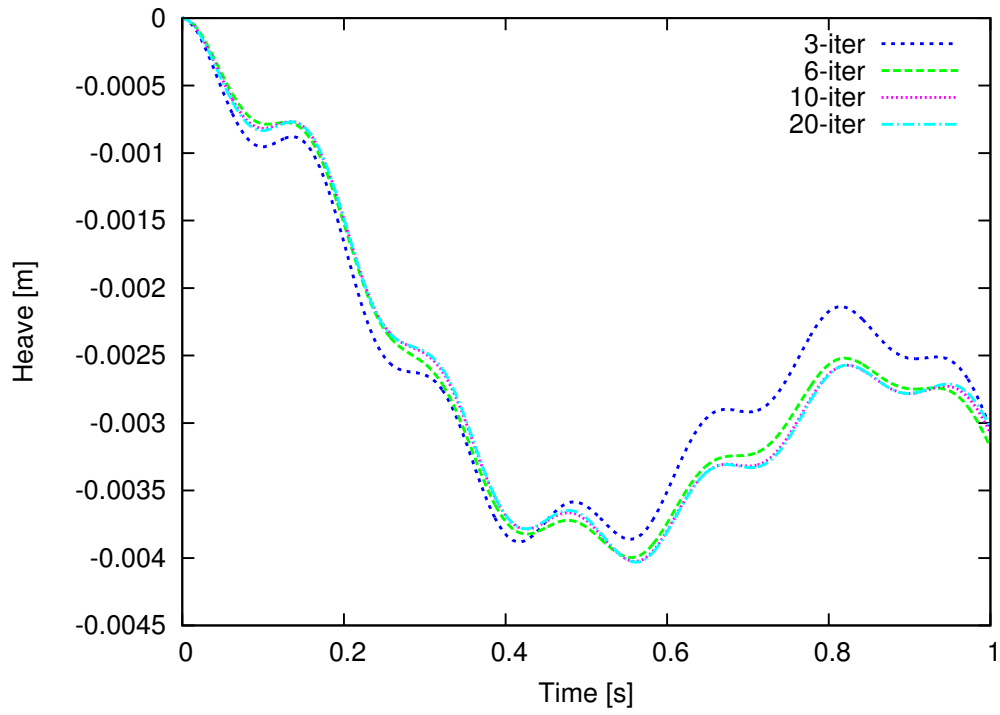
Figure 5.17: Two-way coupling iteration convergence of heave
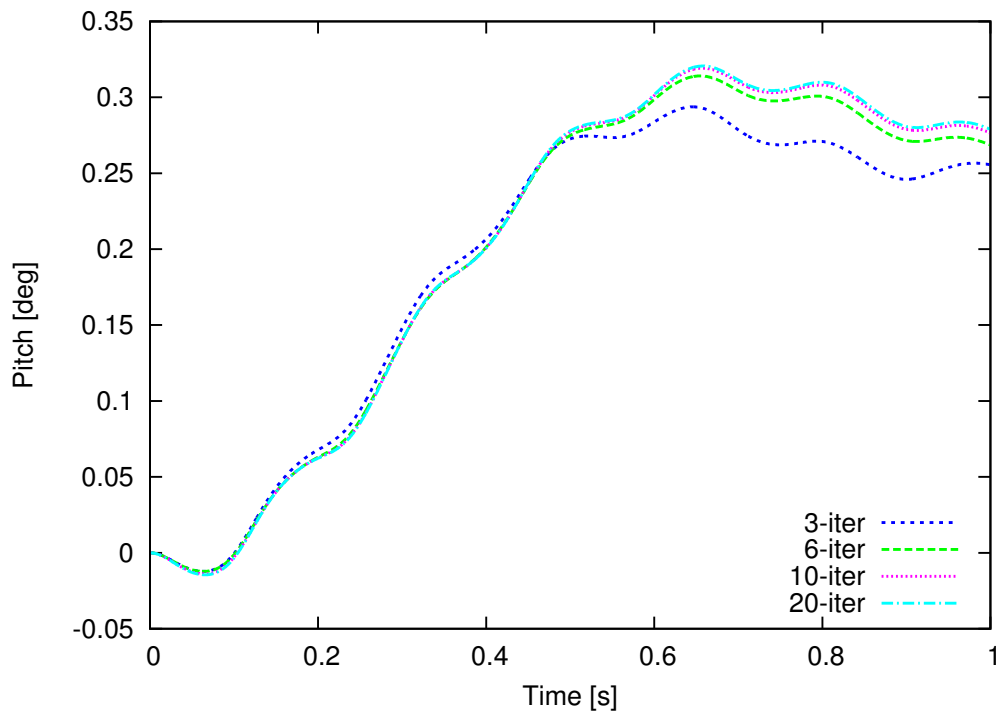
Figure 5.18: Two-way coupling iteration convergence of pitch

described in Section 2.4 to stabilize the motion solver due to added mass effects. The rigid body simulations used 5 iterations to insure convergence of the motion solver. The convergence study in Section 3.1.3 found that 6 iterations were necessary for convergence of the two-dimensional FSI simulations. The elastic two-way coupling simulations show that at least 10 iterations are needed to converge the heave and pitch motions. Figure 5.19, shows the convergence of the vertical sectional force at segment Cut 1.
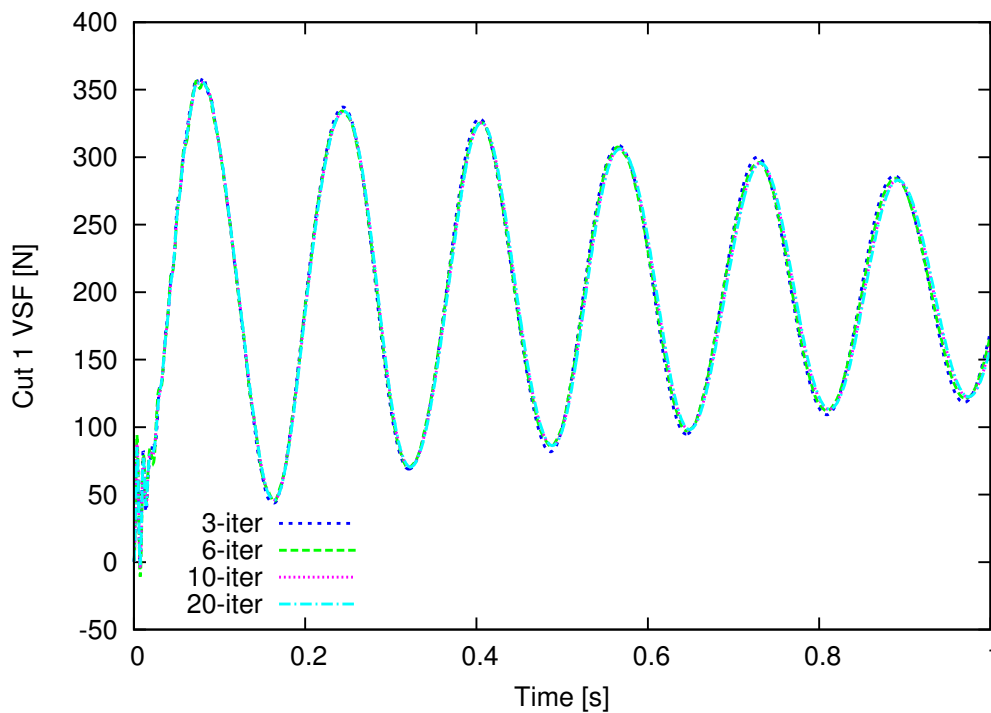
Figure 5.19: Two-way coupling iteration convergence of Cut 1 sectional forces

The simulations are only run for one second, but if the simulations were run for longer the oscillations would damp out and the structure would have a static displacement and vertical sectional force. At least 6 iterations are required for convergence of the sectional forces acting on the structure for a fixed inertial under-relaxation factor of one. After evaluating the convergence of the heave motions, pitch motions, and the vertical section force at segment Cut 1, a minimum of 10 iterations are needed for the elastic two-way coupling simulations. Using a fixed inertial under-relaxation factor of

5.0, the simulation would become unstable during the wetdeck impact. The adaptive inertial under-relaxation scheme was used with a minimum inertial under-relaxation factor of 5.0 to stabilize the FSI solver. The adaptive inertial under-relaxation scheme requires additional iterations for convergence and a total number of 15 iterations per time step is selected for the two-way coupling simulations which model the wetdeck slamming events.

5.2.1 Global Loads

Global structure shear force and bending moment is measured at the segment connection points. The elastic sectional forces at each segment cut are compared in Figure 5.20 using the one-way coupling technique and two-way coupling techniques.

The oscillation differences between the one-way simulation and experiment is from the added mass effects which cause the wetted structure to oscillate at a lower frequency. The one-way coupling technique oscillates at the dry frequency since only the fluid pressures are given to the structure and the fluid does not receive the structure velocities or displacements. The two-way coupling technique captures the added mass effects, but at a larger computational expense from the increase in iterations for convergence. The frequency-of-oscillation of the two-way coupled simulation is higher than the experiments. The higher frequency-of-oscillation may be due to the difference between the simulation and experimental mass distributions. The two-way simulations used the 246 kg mass distribution reported by Ge (2002). The 302 kg Økland (2002) mass distribution, listed in Appendix A, oscillates at a lower frequency due to the larger structure mass. If the 302 kg Økland (2002) mass distribution is used, the two-way oscillation frequencies should more closely match the experimental results.

The two-way coupled amplitudes are closer to the experiments than the one-way coupled amplitudes. However, the one-way coupling amplitudes are on the same
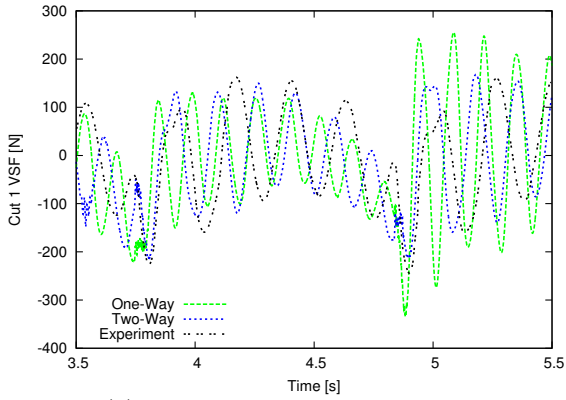
(a) Vertical shear force at Cut 1   (b) Vertical bending moment at Cut 1
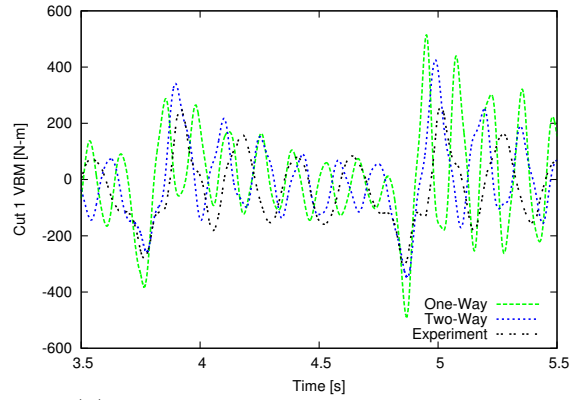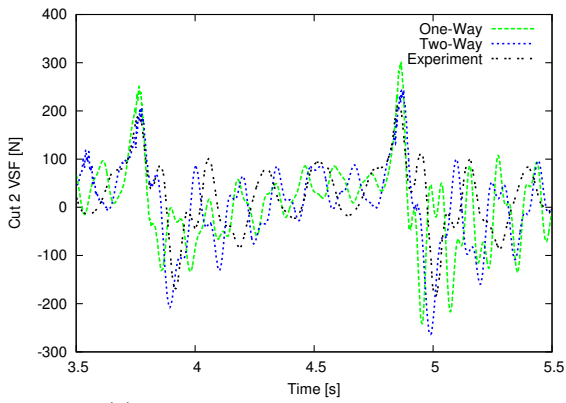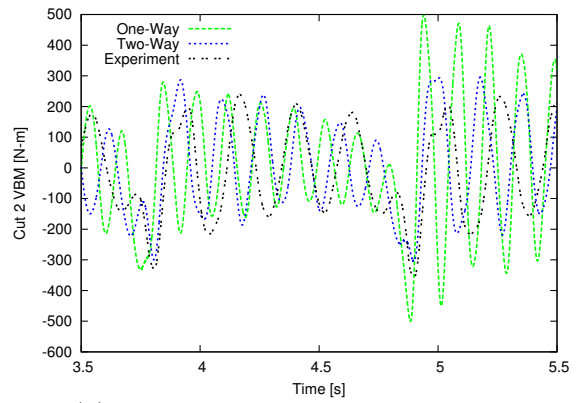
(c) Vertical shear force at Cut 2   (d) Vertical bending moment at Cut 2

Figure 5.20: Elastic simulation of vertical shear force and bending moment at segment cuts

order of magnitude as the two-way and experiments with less computational expense. Different amplitudes are noted between slamming periods that depend on speed and the geometry of the wave at impact. The experimental measurements were taken for a set of wave impacts that produced similar shear force and bending moment amplitudes between slams. The stiffness of the global structure leads to decent results in sectional force and bending moment amplitudes using the one-way coupling. When designing a structure, maximum values are of interest for fracture and fatigue.

5.2.2 Local Loads

The experimental wetdeck structures incorporate transverse and longitudinal stiffeners. The stiffeners are oversized to create an extremely stiff wetdeck structure so focus can be maintained on measuring global structure loads. The local wetdeck plate structures are simulated with the one-way coupling technique for computational efficiency. Stiff structures are usually modeled in a fluid solution as a rigid body and maximum amplitudes will be similar hydroelastic simulation. The plates will oscillate at the dry frequency, but the wetdeck is only wetted during the impact stage for a short duration. The deflections and strains for a chosen point on Decks 1 and 2 near the maximum pressure value are shown in Figures 5.21 and 5.22.

The sampling point on Deck 1 is located 3.780 m forward of the aft perpendicular and 0.101 m to starboard of the center line. The sampling point for Deck 2 is located 3.241 m forward of the aft perpendicular and 0.063 m to starboard of the center line. These correspond to points in between two transverse stiffeners. These points will be used for comparisons of maximum stress later in the chapter with the two-dimensional flat plate simulations in Chapter III.
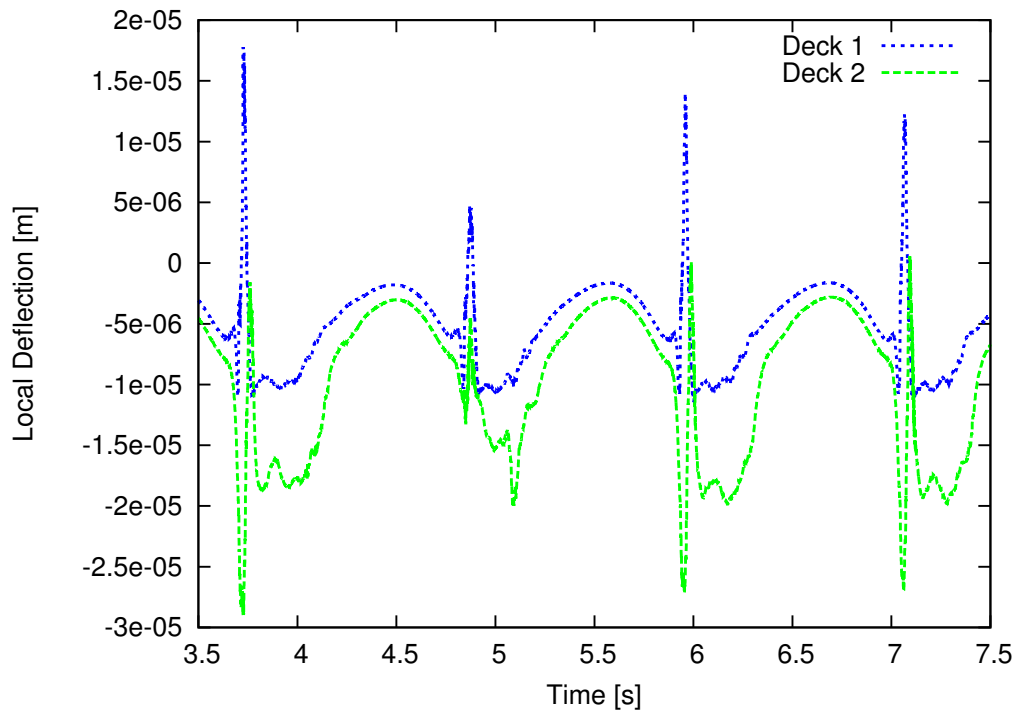
Figure 5.21: Local deflection on Decks 1 and 2
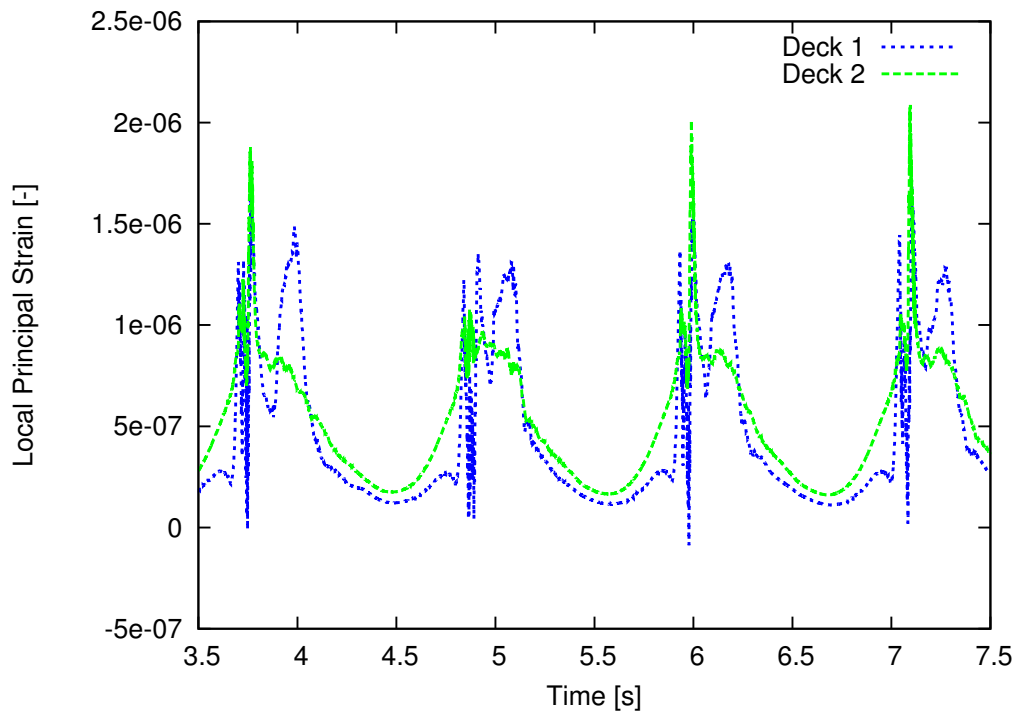
Figure 5.22: Local strain on Decks 1 and 2

5.3 Slamming Analysis

This section presents differences when modeling only local loads and including the global loads for a dynamic slamming simulation. Comparisons are also made with two-dimensional flat plate drop results and recommendations for analytical slamming models are provided. These recommendations and results are only valid for similar flat wetdeck slamming problems.

5.3.1 Global and Local Loads

To understand the effects of the global loads on the local structure, the sample points in the previous section on Decks 1 and 2 are compared with and without the global structure modeled. Figures 5.23 and 5.24 show the deflections and strains at the sample points.
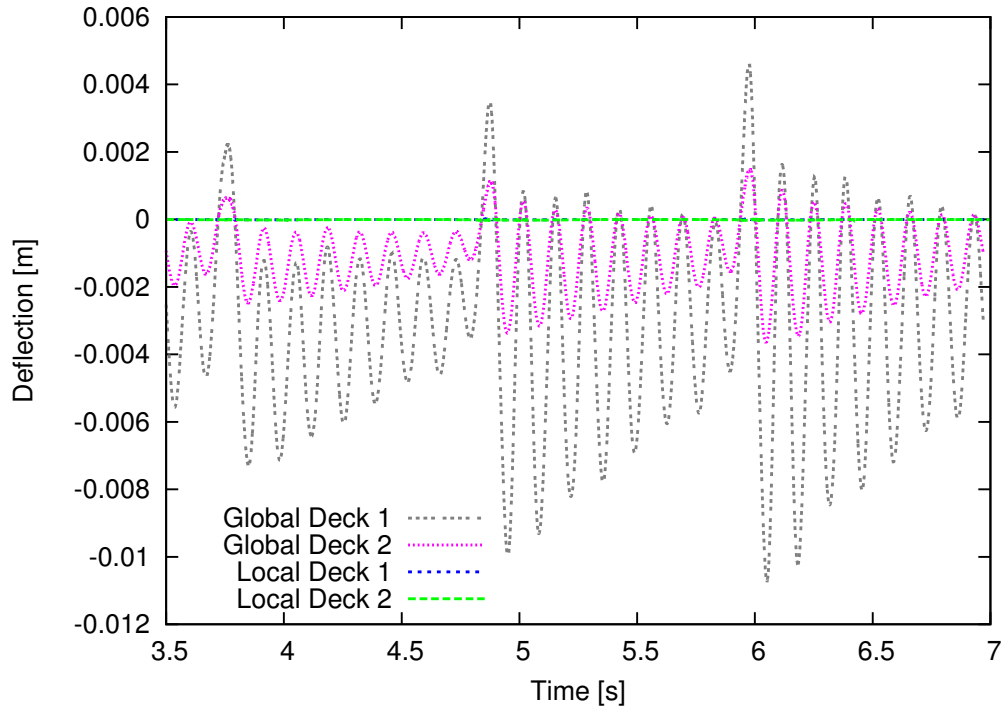
Figure 5.23: Global and local deflection on Decks 1 and 2

The global structure ringing oscillations are present in the deflections and strains that include the global structure model. The global deflections are several orders of
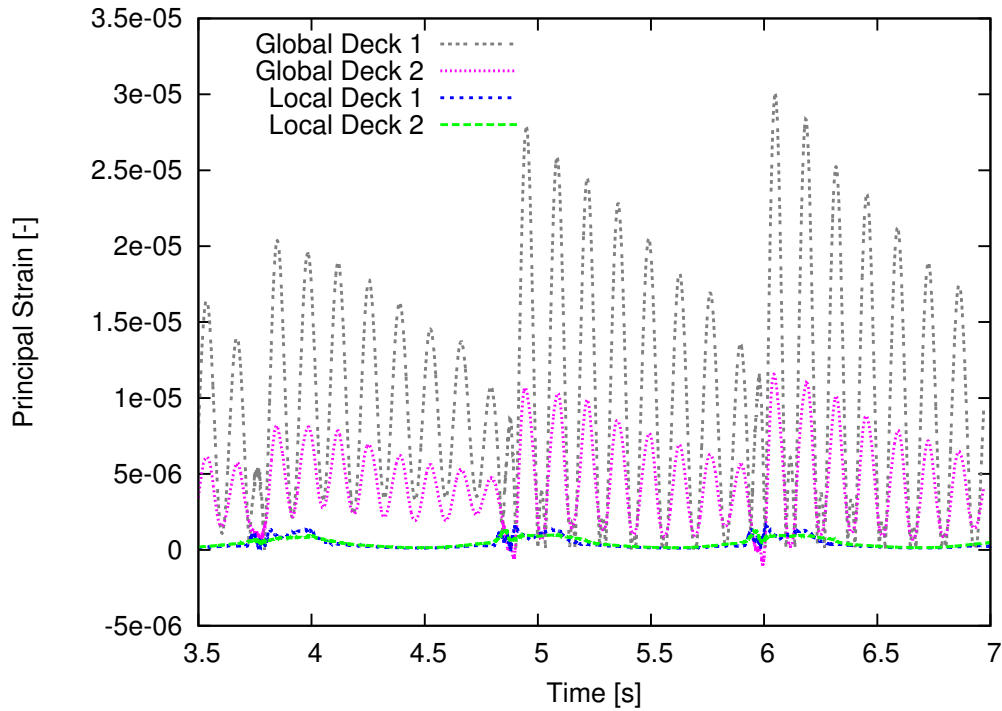
Figure 5.24: Global and local strain on Decks 1 and 2

magnitude larger than the local only deflections. This is largely due to the two node longitudinal bending at the segment cuts that yield larger structure deflections farther away from the segment cuts. The strains with the global structure also exhibit the global ringing oscillations. The local only structure is only influenced by the slamming event. The maximum strains from the global loads are an order of magnitude larger than the local strains from slamming. Figure 5.25 maps the stress from the Deck 1 plate structure during the impact when the local and global loads have similar orders of magnitude for maximum stress at the sample point at approximately 4.905 seconds.

The tertiary stresses on the wetdeck plate are influenced by the global structure response. The local only model shows the excitation of one of the higher plate modes during the impact. The wetdeck plate that includes the global loads exhibits some of the higher mode characteristics of the local model, but there are significant influences from the global loads that change the maximum stress locations. At the time in the simulation the stresses in the global model are at a minimum while the local model
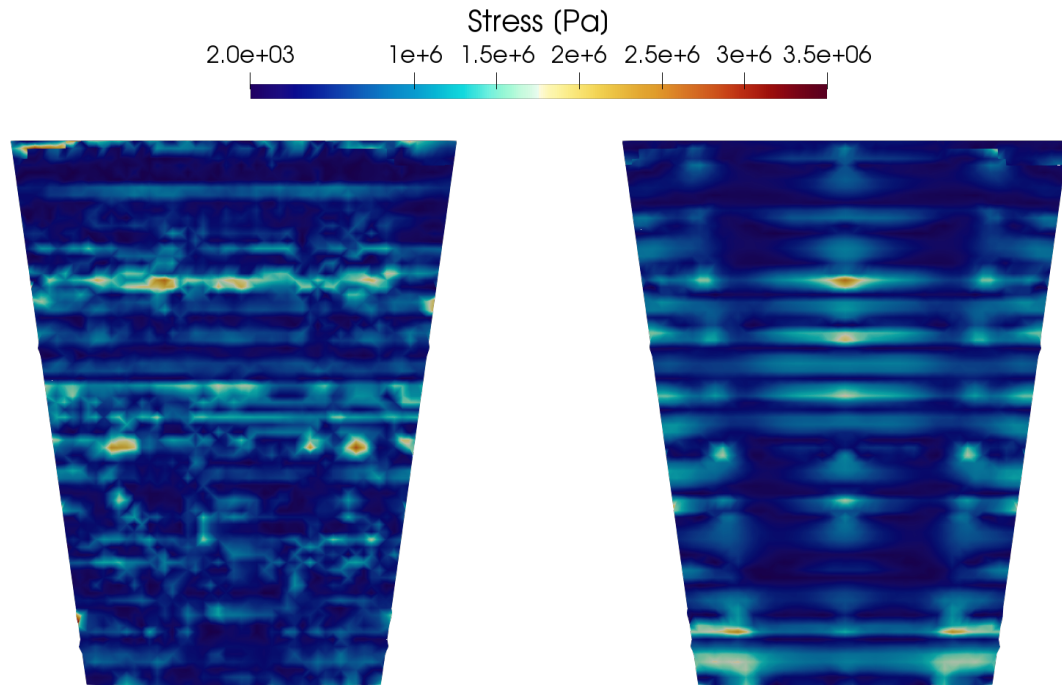
Figure 5.25: Stress mapping of Deck 1 plate for global (left) and local only (right) simulations at 4.905 seconds

is near a maximum. This analysis shows that modeling the global structure in this dynamic slamming simulation is important for capturing the maximum tertiary loads developed in the wetdeck plate.

5.3.2 Analytical Modeling

Comparisons are made between the three-dimensional wetdeck impact and the two-dimensional flat plate impact. The two-dimensional flat plat impact allows for analytical models to be used. Assumptions made by analytical models are addressed and recommendations for reduced order models are provided. Analytical models have the ability to integrate into the early stage design process and provide qualitative guidance. Correct assumptions and solutions to different impact problems need to be validated before analytical slamming models can become a reliable design tool. This study furthers the initial steps for validating and improving analytical slam modeling.

The three-dimensional slamming simulation is broken down into a two-dimensional slice to relate to the flat plate impact simulations and experiments. A slice of Deck 1 during impact is taken at the sample point 0.101 m to starboard of the center line, Figure 5.26. The grid resolution on the hull is 0.01 m.
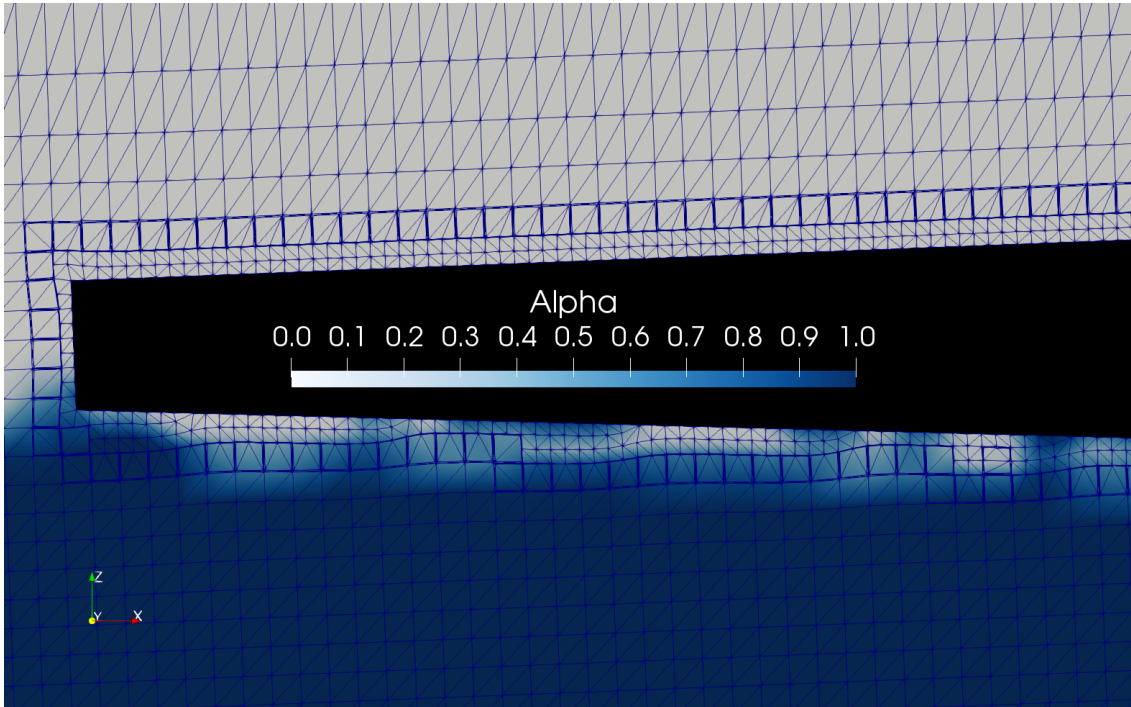
Figure 5.26: Longitudinal slice of Deck 1 at sample point during impact

The grid shows a captured air pocket with mixing similar to the two-dimensional flat plate impact in Figure 3.19. Due to the pitching motion of the catamaran, Deck 1 is close to horizontal at impact. The transverse stiffeners break up Deck 1 into 10 sections of length 0.076 m. Equation 3.2 for the non-dimensional maximum stress uses the length between transverse stiffeners to calculate the loads on the wetdeck plate. When considering the plate impact between stiffeners, the wave radius of curvature compared to the plate length is large and can be assumed to be practically flat. These assumptions were made by the various analytical slamming models and are good assumptions for this wetdeck geometry.

The non-dimensional maximum stress is calculated at the Deck 1 sample point

for the simulations with the global structure and with the local structure only. The non-dimensional maximum stress for the SES simulations are compared with two-dimensional simulations in Figure 5.27.
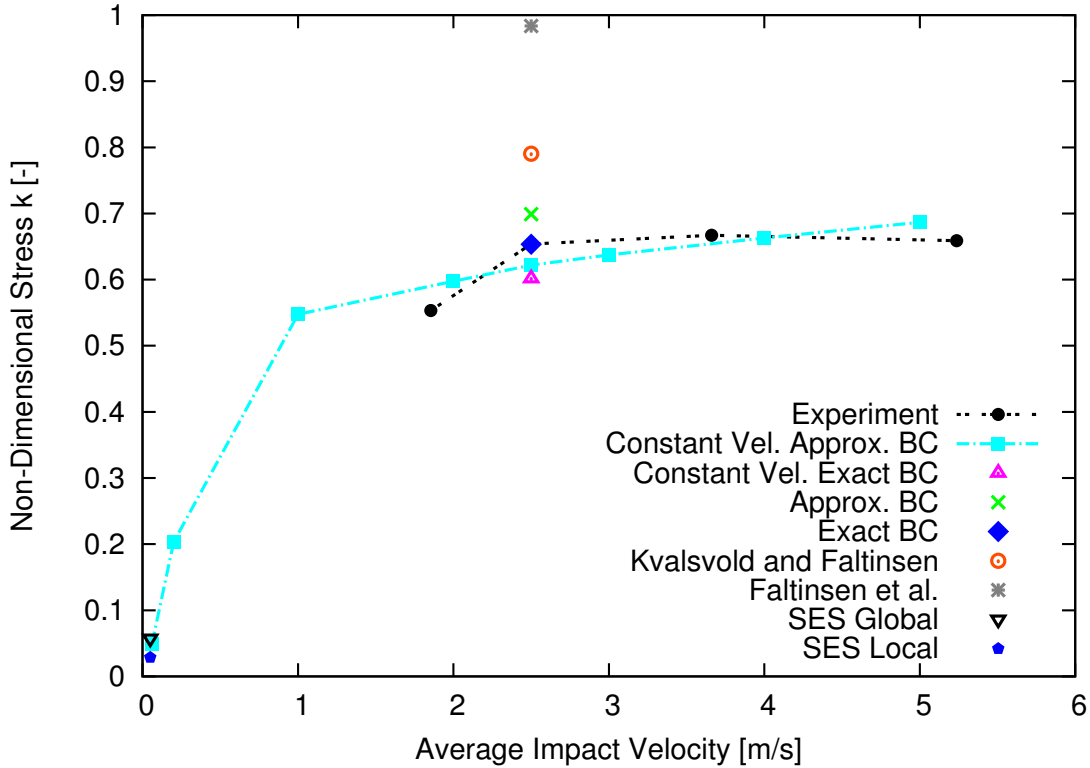
Figure 5.27: Non-dimensional stress located in the middle of two stiffeners

The constant velocity two-dimensional impact with the approximate FSI boundary condition is run for several different impact speeds. The constant velocity impact results agree with the trend from the limited experimental results. The impact velocity of Deck 1 at the sample point is approximated at an average 0.05 m/s. The non-dimensional maximum stress has good agreement with the two-dimensional drop for the structure with the global loads. The model with only the local structure underpredicts the the non-dimensional maximum stress by 50% of the global structure non-dimensional maximum stress. Modeling the global structure response may have significant impact on the local wetdeck structure loads. Influence from the global structure should be explored in future work to determine how much the global struc-

ture response can contribute to the local loads on the wetdeck structure.

Another noticeable trend that Faltinsen et al. (1997) first theorized, is the maximum stress is linearly proportional to the impact velocity in the range he examined. In the two-dimensional flat plate experiments, the velocity that most closely modeled the experimental impact and elastic structure deformation matched the experimental value best. Simplified theories should focus on capturing the correct relative impact velocity if the model intends to use the non-dimensional stress values k. The relative impact velocity is the velocity normal to the wetdeck location of impact. The relative impact velocity V_e is given by Faltinsen et al. (1997) as,

$$V_e = V + U\alpha + u_z \qquad (5.4)$$

where V is the structure velocity normal to the wetdeck impact location, U is the combined forward speed of the wave and wetdeck in head seas, α is the wetdeck angle relative to the forward speed, and u_z is velocity of the wave normal to the wetdeck impact location. The impact velocity V_e can be determined using linear motion functions and modeled for a long period to develop statistics for the relative impact velocity and relative vertical motions. Using these statistics, Faltinsen et al. (1997) presented a joint probability equation for bending stress that is larger than σ_{max} using the non-dimensional stress coefficient k,

$$P = \exp\left[-\left(\frac{\sigma_{max}^2 I}{2k^2 Z^2 \rho ELW\sigma_v^2} + \frac{d^2}{2\sigma_r^2}\right)\right] \qquad (5.5)$$

where σ_v^2 is the variance of the relative vertical velocity V_e, d is the height of the wetdeck above calm water, and σ_r^2 is the variance of the relative vertical motion between the wetdeck impact location and the waves. The statistics for the long term results do not model voluntary reductions in speed due to sea states and the full profile of the non-dimensional stress values should be explored before a reduced order

model can be developed and used.

The non-dimensional stress values are only analyzed in this study for the locations in the middle of two transverse stiffeners. The values for the non-dimensional stress vary along the distance between the stiffeners and were found by Faltinsen et al. (1997) to be between 0.6 and 1.2 for the analytical method. Further analysis of variation of non-dimensional stress at locations between transverse stiffeners should also be explored before implementing a simplified theory. The non-dimensional stress study has only focused on horizontal impact of flat plate geometries and does not apply to more complex geometries, such as catamarans with wedge shaped wetdecks. The FSI solver has proved to be a useful tool in modeling the complex hydroelastic interactions during flat wetdeck slamming events. The solver can be used to further explore the non-dimensional stress and even used as a late stage design tool to validate extreme slam responses for vessels of concern.

CHAPTER VI

Conclusions

6.1 Summary

This study is motivated by recent issues in ship design where underpredicting the dynamic loading and slamming loads have led to structural failure. Specifically, catamarans with flat wetdecks are susceptible to extreme slam events and structural failure from these events. Background information on the latest analytical, experimental, and numerical modeling techniques for slamming is presented. A high-fidelity FSI model is used to study a simple plate impact on a free-surface. Stability of the FSI solver pertaining to the artificial added mass effects from the coupling of segregated algorithms is analyzed. A new adaptive inertial under-relaxation scheme is developed to solve the issue of knowing the maximum modal added mass value before simulation runtime. The FSI solver is then used to study a realistic catamaran geometry with a flat wetdeck. The effects of modeling the global and local structure separately are shown. The realistic wetdeck slam events are related to the simple plate impact study and recommendations are provided for analytical modeling of the process. Assumptions made in the two-dimensional slam models are also confirmed with the FSI solver.

6.2   Contributions

The following are contributions to the research community from this dissertation. A new analysis of the FSI solver using a simple two-dimensional plate impact problem. The FSI solver analysis includes influences of the exact and approximate FSI boundary conditions for small displacements, a first look at the dynamic non-linear structure geometry and non-linear material plastic deformation influences, and the first CFD analysis validating the relationship of non-dimensional plate stress to the velocity of impact. A new adaptive inertial-under relaxation scheme is developed and analyzed to stabilize the large artificial added mass effects in the FSI solver. The first techniques for estimating the modal added mass during runtime and reduce over estimates due to small accelerations is provided. New details of the artificial added mass from the coupling of segregated fluid and structure solvers is presented. This dissertation provides the first comparison of the MARINTEK SES experiments with FSI results using CFD. The full field data is provided by the CFD and the FEA simulations. The first analysis of local and global slamming loads for flat wetdecks, shows that local tertiary loads can be significantly influenced by the global primary loads of the ship structure. Visualization of the local tertiary loads on the wetdeck plate using the full field data show the influence of the primary global structure. The first CFD simulations used to compute the non-dimensional stress on the wetdeck, show that the two-dimensional simple plate problem can relate to three-dimensional wetdeck slamming events. The relationship of the non-dimensional stress to the impact velocity is validated using three-dimensional slamming simulations.

6.3   Future Work

The FSI solver used in this study has proved the solvers potential for studying complex interactions between the fluid and structure. The most promising areas of

future research lie in the potential to provide appropriate recommendations to classification societies for dynamic loads on structures. Further suggestions for future work include exploring the non-dimensional stress coefficient at different impact velocities and developing mathematical relationships for the non-dimensional stress and velocity of impact. The effects of turbulence, compressiblity, and cavitation on the hydroelastic response during an impact can be investigated. Also the adaptive inertial under-relaxation scheme can be improved by incorporating a convergence criteria to study the stability and convergence of the adaptive scheme. Adding the full FEM to the solver library to incorporate non-linear geometries and materials would increase the usefulness of the solver and allow for non-linearities in the structure to be modeled. These are some of the immediate areas of future work and improvements.

APPENDIX

APPENDIX A

Mass Distributions for the SES

Component	Mass	LCG	TCG	VCG	r_{11}	r_{22}	r_{33}
	kg	m	m	m	m	m	m
Hull SB fore	20	0.95	0.33	0.25	0.1	0.45	0.55
Hull SB mid	17	2.08	0.33	0.25	0.1	0.35	0.45
Hull SB aft	25	3.3	0.33	0.25	0.1	0.4	0.5
Hull PS fore	20	0.95	-0.33	0.25	0.1	0.45	0.55
Hull PS mid	17	2.08	-0.33	0.25	0.1	0.35	0.45
Hull PS aft	25	3.3	-0.33	0.25	0.1	0.4	0.5
TR+SPR, SB aft	3.2	2.68	0.335	0.31	0	0	0.1
TR+SPR, SB fore	3.2	1.48	0.335	0.31	0	0	0.1
TR+SPR, PS aft	3.2	2.68	-0.335	0.31	0	0	0.1
TR+SPR, PS fore	3.2	1.48	-0.335	0.31	0	0	0.1
TR+SPR, deck fore	2.3	0.77	0	0.44	0	0	0
TR+SPR, deck mid	2.3	2.08	0	0.44	0	0	0
TR+SPR, deck aft	2.3	3.39	0	0.44	0	0	0
Deck 1	9.1	0.34	0	0.35	0.1	0.23	0.2
Deck 2	3.2	1.12	0	0.35	0.1	0.27	0.2
Deck 3	4.8	2.08	0	0.35	0.1	0.3	0.3
Deck 4	5.4	3.39	0	0.35	0.1	0.4	0.4
Suspension mid	3	2.08	0	0.42	0.2	0.4	0.4
Suspension aft	3	3.39	0	0.42	0.2	0.4	0.4
Motor SB	18	3.03	0.45	0.65	0.1	0	0
Motor PS	18	3.03	-0.45	0.65	0.1	0	0
PR+shaft SB	2	3.9	0.35	0	0	0	0
PR+shaft PS	2	3.9	-0.35	0	0	0	0
RudderContr. SB	1.2	3.8	0.35	0.4	0	0	0
RudderContr. PS	1.2	3.8	-0.35	0.4	0	0	0
RudderMachine SB	2.2	4	0.35	0.4	0	0	0
RudderMachine PS	2.2	4	-0.35	0.4	0	0	0
MRU	3.8	2.02	-0.21	0.31	0	0	0
Rudder/plastic SB	0.1	2.1	0.35	0.4	0	1.2	1.2
Rudder/plastic PS	0.1	2.1	-0.35	0.4	0	1.2	1.2
Pulsetrigger	3	3.4	0.35	0.4	0	0	0
Cables etc.	2	2.1	-0.15	0.4	0.3	1	1
Ballast SB	9	3.98	0.37	0.25	0	0	0
Ballast PS	9	3.98	-0.37	0.25	0	0	0
	246	2.468	0	0.335	0.372	1.128	1.179

Table A.1: Mass Distribution from Ge (2002)

Component	Mass	LCG	TCG	VCG	r_{11}	r_{22}	r_{33}
	kg	m	m	m	m	m	m
Hull SB fore	20	0.95	0.33	0.25	0.1	0.45	0.55
Hull SB mid	17	2.08	0.33	0.25	0.1	0.35	0.45
Hull SB aft	25	3.3	0.33	0.25	0.1	0.4	0.5
Hull PS fore	20	0.95	-0.33	0.25	0.1	0.45	0.55
Hull PS mid	17	2.08	-0.33	0.25	0.1	0.35	0.45
Hull PS aft	25	3.3	-0.33	0.25	0.1	0.4	0.5
TR+SPR, SB aft	3.2	2.68	0.335	0.31	0	0	0.1
TR+SPR, SB fore	3.2	1.48	0.335	0.31	0	0	0.1
TR+SPR, PS aft	3.2	2.68	-0.335	0.31	0	0	0.1
TR+SPR, PS fore	3.2	1.48	-0.335	0.31	0	0	0.1
TR+SPR, deck fore	2.3	0.77	0	0.44	0	0	0
TR+SPR, deck mid	2.3	2.08	0	0.44	0	0	0
TR+SPR, deck aft	2.3	3.39	0	0.44	0	0	0
Deck 1	9.1	0.34	0	0.35	0.1	0.23	0.2
Deck 2	3.2	1.12	0	0.35	0.1	0.27	0.2
Deck 3	4.8	2.08	0	0.35	0.1	0.3	0.3
Deck 4	5.4	3.39	0	0.35	0.1	0.4	0.4
Suspension mid	3	2.08	0	0.42	0.2	0.4	0.4
Suspension aft	3	3.39	0	0.42	0.2	0.4	0.4
Motor SB	18	3.03	0.45	0.65	0.1	0	0
Motor PS	18	3.03	-0.45	0.65	0.1	0	0
PR+shaft SB	2	3.9	0.35	0	0	0	0
PR+shaft PS	2	3.9	-0.35	0	0	0	0
RudderContr. SB	1.2	3.8	0.35	0.4	0	0	0
RudderContr. PS	1.2	3.8	-0.35	0.4	0	0	0
RudderMachine SB	2.2	4	0.35	0.4	0	0	0
RudderMachine PS	2.2	4	-0.35	0.4	0	0	0
MRU	3.8	2.02	-0.21	0.31	0	0	0
Rudder/plastic SB	0.1	2.1	0.35	0.4	0	1.2	1.2
Rudder/plastic PS	0.1	2.1	-0.35	0.4	0	1.2	1.2
Pulsetrigger	3	3.4	0.35	0.4	0	0	0
Cables etc.	2	2.1	-0.15	0.4	0.3	1	1
Ballast SB	9	3.98	0.37	0.25	0	0	0
Ballast PS	9	3.98	-0.37	0.25	0	0	0
Ballast SB 1	5	3	0.35	0.095	0	0	0
Ballast PS 1	5	3	-0.35	0.095	0	0	0
Ballast SB 2	10	1.34	0.42	-0.105	0	0	0
Ballast PS 2	10	1.34	-0.42	-0.105	0	0	0
Ballast SB 3	6	1.34	0.42	-0.155	0	0	0
Ballast PS 3	6	1.34	-0.42	-0.155	0	0	0
Ballast SB 4	7	0.18	0.35	0.135	0	0	0
Ballast PS 4	7	0.18	-0.35	0.135	0	0	0
	302	1.55	0	0.316	0.3815	1.0721	1.13

Table A.2: Mass Distribution from Økland (2002)

BIBLIOGRAPHY

BIBLIOGRAPHY

Amicarelli, A., Albano, R., Mirauda, D., Agate, G., Sole, A., and Guandalini, R. (2015). A Smoothed Particle Hydrodynamics model for 3D solid body transport in free surface flows. *Computers and Fluids*, 116:205–228.

Aquelet, N., Souli, M., and Olovsson, L. (2006). Euler-Lagrange coupling with damping effects: Application to slamming problems. *Computer Methods in Applied Mechanics and Engineering*, 195(1-3):110–132.

Bishop, R. E. D. and Price, W. G. (1979). Hydroelasticity of ships. page 420 p. : ill. ; 29 cm.

Bishop, R. E. D., Price, W. G., and Wu, Y. (1986). A general linear hydroelasticity theory of floating structures moving in a seaway. *Philosophical Transactions of the Royal Society of London. Series A, Mathematical and Physical Sciences*, 316(1538):375 LP – 426.

Camilleri, J., Temarel, P., and Taunton, D. (2015). Two-dimensional numerical modelling of slamming impact loads on high-speed craft. In *7th International Conference on Hydroelasticity in Marine Technology*, pages 43–54, Split, Croatia.

Das, K. and Batra, R. C. (2011). Local water slamming impact on sandwich composite hulls. *Journal of Fluids and Structures*, 27(4):523–551.

De Rosis, A., Falcucci, G., Porfiri, M., Ubertini, F., and Ubertini, S. (2014). Hydroelastic analysis of hull slamming coupling lattice Boltzmann and finite element methods. *Computers and Structures*, 138:24–35.

Dessi, D., Faiella, E., Geiser, J., Alley, E., Dukes, J., and Marine, C. (2016). Design , assessment and testing of a fast catamaran for FSI investigation. In *31st Symposium on Naval Hydrodynamics*, number September, pages 11–16, Monterey, California.

el Moctar, O., Ley, J., Oberhagemann, J., and Schellin, T. (2017). Nonlinear computational methods for hydroelastic effects of ships in extreme seas. *Ocean Engineering*, 130(February 2016):659–673.

El Moctar, O., Oberhagemann, J., and Schellin, T. E. (2011). Free-surface RANS method for hull girder springing and whipping. *In Proc. SNAME*, (V):286–300.

Faltinsen, O. M. (1997). The effect of hydroelasticity on ship slamming. *Philosophical Transactions of the Royal Society A: Mathematical, Physical and Engineering Sciences*, 355(1724):575–591.

Faltinsen, O. M. (2001). Hydroelastic slamming. *Journal of Marine Science and Technology*, 5(2):49–65.

Faltinsen, O. M., Kvålsvold, J., and Aarsnes, J. V. (1997). Wave impact on a horizontal elastic plate. *Journal of Marine Science and Technology*, 2(2):87–100.

Ge, C. (2002). *Global Hydroelastic Response of Catamarans Due to Wetdeck Slamming.* PhD thesis, Norwegian University of Science and Technology, Trondheim, Norway.

Ge, C., Faltinsen, O. M., and Moan, T. (2005). Global Hydroelastic Response of Catamarans Due to Wetdeck Slamming. *Journal of Ship Research*, 49(1):24–42.

Gong, K., Shao, S., Liu, H., Wang, B., and Tan, S. K. (2016). Two-phase SPH simulation of fluid-structure interactions. *Journal of Fluids and Structures*, 65:155–179.

Greenhow, M. and Lin, W.-m. (1983). Nonlinear Free Surface Effects: Experiments and Theory. page 103.

Jacobi, G., Thomas, G., Davis, M. R., and Davidson, G. (2014). An insight into the slamming behaviour of large high-speed catamarans through full-scale measurements. *Journal of Marine Science and Technology (Japan)*, 19(1):15–32.

Khabakhpasheva, T. and Korobkin, a. (2003). Approximate models of elastic wedge impact. *18th IWWFB (April 2003)*, 0(1):2–6.

Kim, J. H., Kim, Y., Yuck, R. H., and Lee, D. Y. (2015). Comparison of slamming and whipping loads by fully coupled hydroelastic analysis and experimental measurement. *Journal of Fluids and Structures*, 52:145–165.

Kim, Y. Y. Y. Y., Kim, K. H., Kim, J. H., Kim, T., Seo, M. G., and Kim, Y. Y. Y. Y. (2011). Time-domain analysis of nonlinear motion responses and structural loads on ships and offshore structures: Development of WISH programs. *International Journal of Naval Architecture and Ocean Engineering*, 3(1):37–52.

Korobkin, A., Guéret, R., and Malenica, Š. (2006). Hydroelastic coupling of beam finite element model with Wagner theory of water impact. *Journal of Fluids and Structures*, 22(4):493–504.

Korobkin, A. A., Khabakhpasheva, T. I., and Maki, K. J. (2017). Hydrodynamic forces in water exit problems. *Journal of Fluids and Structures*, 69(October 2015):16–33.

Kvalsvold, J. and Faltinsen, O. M. (1995). Hydroelastic modeling of wet deck slamming on multihull vessels. *Journal of ship research*, 39(3):225–239.

Lavroff, J., Davis, M. R., Holloway, D. S., and Thomas, G. (2013). Wave slamming loads on wave-piercer catamarans operating at high-speed determined by hydroelastic segmented model experiments. *Marine Structures*, 33:120–142.

Lind, S. J., Stansby, P. K., Rogers, B. D., and Lloyd, P. M. (2015). Numerical predictions of water-air wave slam using incompressible-compressible smoothed particle hydrodynamics. *Applied Ocean Research*, 49:57–71.

Maki, K. J., Lee, D., Troesch, A. W., and Vlahopoulos, N. (2011). Hydroelastic impact of a wedge-shaped body. *Ocean Engineering*, 38(4):621–629.

McVicar, J., Lavroff, J., and Davis, M. (2015). Effect of Slam Force Duration on the Vibratory Response of a Lightweight High-Speed Wave-Piercing Catamaran. *Journal of Ship Research*, 59(2):69–84.

McVicar, J., Lavroff, J., Davis, M. R., and Thomas, G. (2018). Fluidstructure interaction simulation of slam-induced bending in large high-speed wave-piercing catamarans. *Journal of Fluids and Structures*, 82:35–58.

Mesa, J. D. and Maki, K. J. (2017). Numerical hydroelastic analysis of slamming for high speed vessels. In *14th International Conference on Fast Sea Transportation, FAST*, pages 1–8, Nantes, France.

MOL COMFORT, M. (2015). Final Report of Committee on Large Container Ship Safety (MOL COMFORT). Technical Report March, Committee on Large Container Ship Safety, Japan.

MSC Napoli, M. (2008). Report on the investigation of the structural failure of MSC Napoli English Channel on 18 January 2007. Technical Report 9, Marine Accident Investigation Branch, Southampton, UK.

Oberhagemann, J. (2016). *On Prediction of Wave-Induced Loads and Vibration of Ship Structures with Finite Volume Fluid Dynamic Methods*. PhD thesis, University of Duisburg-Essen.

Økland, O. D. (2002). *Theoretical and experimental analysis of wetdeck slamming*. PhD thesis, Norwegian University of Science and Technology, Trondheim, Norway.

Økland, O. D., Zhao, R., and Moan, T. (2003). Numerical assessment of segmented test model approach for measurement of whipping responses. In *7th International Conference on Fast Sea Transportation, FAST'2003*.

Piro, D. J. (2013). *A Hydroelastic method for the analysis of global response due to slamming events*. PhD thesis, University of Michigan.

Piro, D. J. and Maki, K. J. (2011). Hydroelastic Wedge Entry and Exit. *FAST 2011 11th International Conference on Fast Sea Transportation*, (September).

Piro, D. J. and Maki, K. J. (2013). Hydroelastic analysis of bodies that enter and exit water. *Journal of Fluids and Structures*, 37:134–150.

Seng, S. (2012). *Slamming and Whipping Analysis of Ships*. PhD thesis, Technical University of Denmark.

Seng, S., Jensen, J. J., and Malenica, Š. (2014). Global hydroelastic model for springing and whipping based on a free-surface CFD code (OpenFOAM). *International Journal of Naval Architecture and Ocean Engineering*, 6(4):1024–1040.

Southall, N., Lee, Y., Johnson, M. C., Lin, F., and White, N. (2016). Coupling CFD with a Time-domain Ship Motions Method for Prediction of Slamming. *26th International Ocean and Polar Engineering Conference*, (July):376–383.

Stenius, I., Rosén, A., and Kuttenkeuler, J. (2007). Explicit FE-modelling of hydroelasticity in panel-water impacts. *International Shipbuilding Progress*, 54(2-3):111–127.

Stenius, I., Rosén, A., and Kuttenkeuler, J. (2011). Hydroelastic interaction in panel-water impacts of high-speed craft. *Ocean Engineering*, 38(2-3):371–381.

Swidan, A., Thomas, G., Penesis, I., Ranmuthugala, D., Amin, W., Allen, T., Battley, M., Penesis, I., Allen, T., and Battley, M. (2017). Wetdeck slamming loads on a developed catamaran hullform experimental investigation. *Ships and Offshore Structures*, 12(5):653–661.

Thomas, G., Winkler, S., Davis, M., Holloway, D., Matsubara, S., Lavroff, J., and French, B. (2011). Slam events of high-speed catamarans in irregular waves. *Journal of Marine Science and Technology*, 16(1):8–21.

Veldman, A. E. P., Seubers, H., van der Plas, P., Zahraei, M. H., Wellens, P. R., and Huijsmans, R. H. (2018). Preventing the Added-Mass Instability in Fluid-Solid Interaction for Offshore Applications. *Proceedings of the ASME 2018 37th International Conference on Ocean, Offshore and Arctic Engineering*, pages 1–10.

Volpi, S., Diez, M., Sadat-Hosseini, H., Kim, D. H., Stern, F., Thodal, R. S., and Grenestedt, J. L. (2017). Composite bottom panel slamming of a fast planing hull via tightly coupled fluid-structure interaction simulations and sea trials. *Ocean Engineering*, 143(February):240–258.

Von Karman, T. (1929). The impact on seaplane floats during landing. *National Advisory Committee For Aeronautics*.

Wagner, H. (1932). {Ü}ber Sto{ß}-und Gleitvorg{ä}nge an der Oberfl{ä}che von Fl{ü}ssigkeiten. *ZAMM-Journal of Applied Mathematics and Mechanics/Zeitschrift f{ü}r Angewandte Mathematik und Mechanik*, 12(4):193–215.

113

Wang, S. and Guedes Soares, C. (2017). Hydroelastic effects on slamming loads and dynamic response of flexible panels. *Progress in the Analysis and Design of Marine Structures - Proceedings of the 6th International Conference on Marine Structures, MARSTRUCT 2017*, (2016):59–68.

Whelan, J. R. (2004). *Wetdeck slamming of high-speed catamarans with a centre bow.* PhD thesis, University of Tasmania.

Young, Y. L., Chae, E. J., and Akcabay, D. T. (2012). Hybrid algorithm for modeling of fluid-structure interaction in incompressible, viscous flows. *Acta Mechanica Sinica*, 28(4):1030–1041.

Yvin, C., Leroyer, A., and Visonneau, M. (2014). Added mass evaluation with a finite volume solver for applications in fluid structure interaction problems solved with co-simulation. *Journal of Fluids and Structures*, 81:528–546.

Zhao, R. and Faltinsen, O. M. (1992). Slamming loads on high-speed vessels. *19. Symp. Naval Hydrodyn., Seoul*.